# NMR STUDIES OF MULTI-COMPONENT
MACROMOLECULAR SOLUTIONS

SULIMAN BARHOUM
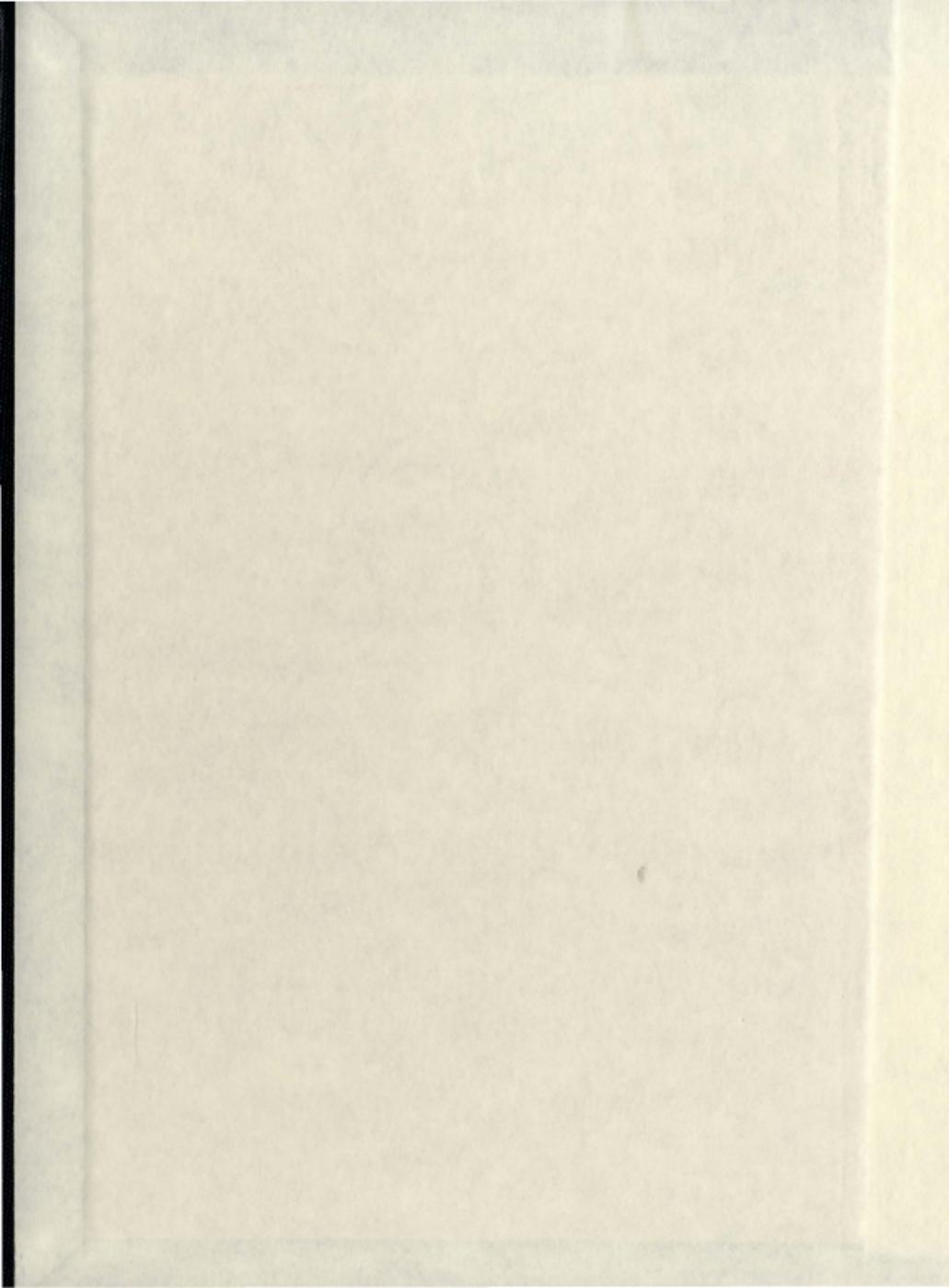
NMR Studies of Multi-component Macromolecular Solutions

by

© Suliman Barhoum
M.Sc.

A thesis submitted to the
School of Graduate Studies
in partial fulfillment of the
requirements for the degree of
Doctor of Philosophy.

Department of Physics and Physical Oceanography
Memorial University of Newfoundland

July 10, 2012

Abstract

My doctoral studies deals with model systems in soft matter. In these model systems, we address questions that are on the interface between physics and biology. The primary focus of the studies is to explore the dynamics and structural changes of aggregations of biologically relevant multi-component polymer, protein, peptide, and micellar systems using nuclear magnetic resonance (NMR) based techniques. Diffusometry, relaxometry, and deuterium NMR techniques were chosen since they complement one another in understanding the dynamics and structure in the process of macromolecular self-assembly. Moreover, identifying the size of nanoparticle clusters in these model systems is a challenging problem and there is no technique that gives complete answers. Therefore, my doctoral work is a systematic attempt to use NMR as a tool to make quantitative statements about the nature of macromolecular clustering.

During my PhD, we used a model polymer-surfactant solution in order to identify surfactant concentration regimes relevant to understanding the behavior of biomolecules in a ˝crowded environment˝ consisting of multiple species of macromolecules. Such crowded environments are a characteristic of intracellular plasma. We studied a system composed of nonionic polymer poly(ethylene glycol) (PEO) and an anionic sodium dodecyl sulfate (SDS) at different SDS concentrations. Using NMR diffusometry, we measured the self-diffusion coefficients of the polymer (PEO) and surfactant (SDS) components simultaneously as a function of SDS concentration. Also, we obtained NMR relaxation rates for PEO and the chemical shifts as a function of SDS concentration. Using a simple model to interpret our experimental results, we developed a precise

ii

method to identify the onset of aggregation of SDS on PEO chains (critical aggregation concentration CAC=3.5 mM) and a crossover concentration (C_2 = 60 mM) which is associated with a sharp change in the relaxation behavior, as well as an increase in free surfactant concentration. Moreover, in the context of a simple model, we identified the SDS concentration (C_m = 145 mM) beyond which the diffusion of the aggregates was strongly hindered by the presence of other structures such as free micelles.

Another source of hindered diffusion, apart from macromolecular crowding, is diffusion in the presence of geometrical constraints. In the case of cylindrical or wormlike micelles, the constraint is to diffuse within the cylinder. Aggregates in a multi-component wormlike micelle are difficult to study via scattering techniques because they would require contrast matching. Therefore, We studied a system composed of a zwitterionic surfactant N-tetradecyl-N, N-dimethyl-3-ammonio-1-propanesulfonate (TDPS) and an anionic surfactant SDS in brine. NMR diffusometry indicates that the self-diffusion coefficients of surfactant is consistent with restricted diffusion within a reptating micelle. Using a simple model to interpret our diffusometry results, we estimated the average end-to-end micellar distance to be ≈ 1 μm. Using NMR relaxometry, we obtained the wormlike micelle overlap concentration (a characteristic concentration $C^{threshold}$ = 4.5 mM). Deuterium NMR spectra indicate that the internal structure of the wormlike micellar system includes domains with different orientation orders with slow exchange between domains. Our experimental results (NMR diffusometry and rheometry) revealed that the wormlike micelles exhibit remarkable polymer-like scalings with a crossover from Zimm-like (diffusion) to Rouse-like (rheology) regimes.

During the latter part of my PhD, we explored protein solutions. We were motivated by the fact that scattering techniques in concentrated lysozyme protein solutions show conflicting reports over the existence of an equilibrium cluster phase. It is recognized that protein aggregation is essential in understanding the biophysics of proteins. Also, it must be noted that protein aggregations and misfoldings, which are implicated as a root cause of some diseases that are thus sometimes called ``conformational diseases´´ are technically challenging to quantify. To address this problem,

we worked on diffusion of lysozyme proteins in concentrated lysozyme solutions. Lysozyme is a common mammalian protein, which is found in human amylases. Using NMR diffusometry, we obtained the self-diffusion coefficients of lysozyme in concentrated lysozyme solutions. Diffusometry and relaxometry showed that both the observed diffusion coefficient and relaxation rates are a weighted average of monomer and aggregate fractions. Therefore, our studies gave a strong evidence for both lysozyme monomers and thermodynamically stable lysozyme clusters in the protein solution with a rapid exchange between monomer and aggregate on the NMR time scale.

Finally, we addressed a practical problem of relevance to biochemists and biophysicists. Studying the dynamics of macromolecules and aggregates in multicomponent systems composed of peptide or protein and surfactants is challenging. Many peptides and proteins are synthesized in tiny quantities. We used NMR diffusometry and relaxometry to explore systems composed of peptides that are very long compared to the surfactant, dissolved with an anionic surfactant in an aqueous solution. We compared the results to those for shorter dipeptides whose size is comparable to the surfactant. Diffusometry shows that the longer peptide behaves as if there is no free fraction of peptide molecules in the solution. Based on that, we extracted reliable physical quantities such as the true hydrodynamic radius of long peptide-surfactant aggregate as a function of surfactant concentration. On the other hand, the smaller dipeptides are partitioned between the bound and free state such that the fraction of the bound peptide varies with surfactant concentration.

Acknowledgements

Foremost, I would like to express my deep appreciation to my parents, Mr. Abdallah Barhoum and Mrs. Khaldeyeh Durgam who sacrifice in order to support me spiritually and financially. Also, I would like to thank my sister Sawsan and my brothers Samer and Ayman for their constant encouragement. I would like to express my thanks to my friends Ahmad Almudallal, Anas Malkawi, Awab Hamodat, and Ahmad Zien for their continuous support.

I would also like to acknowledge all my fellow members, Edward Hayden, Hughie Newman, Dr. Marek Bromberek, Michael Ducey, Payam Bagheri, and Andrew Bartlett, in my research group for their encouragement, help, and advice.

I would like to express my sincere gratitude to one of the best supervisors ever Dr. Anand Yethiraj for his support, guidance, patience, enthusiasm, and immense knowledge that helped me a lot during my PhD program. Also, I would like to acknowledge my supervisory committee: Dr. Ivan Saika-Voivod and Dr. Todd Andrews for their encouragement and insightful comments during the supervisory committee meetings. I am grateful to Dr. Valerie Booth for her collaboration, constructive contribution in performing one of the projects during my PhD, and for giving me an opportunity to use items and to prepare samples in her laboratory. In addition, I would like to acknowledge Dr. Rolando Castillo for his collaboration and constructive contribution in performing one of the projects during my PhD.

I would like to thank Dr. Celine Schneider who has not spared any effort training me in using the nuclear magnetic resonance machine and guiding me in running my samples. Also, I would

v

Contents

List of Tables

List of Figures

List of Abbreviations

D_2O	Deuterium oxide
SDS	Sodium dodecyl sulfate
Ala-Gly	Alanine-Glycine
CHAPS	3-[(3-Cholamidopropyl)dimethylammonio]-1-propanesulfonate
CPMG	Carr-Purcell-Meiboom-Gill
DPC	dodecylphosphocholine
ITC	Isothermal titration calorimetry
NMR	Nuclear magnetic resonance
PDI	Polydispersity index
PEO	Poly(ethylene) oxide
PFG	Pulsed field gradient
PFG-STE	Pulsed field gradient stimulated echo
RF	Radio frequency
Rheo-SANS	Rheology and small angle neutron scattering

SAXS	Small angle X-ray scattering
TDPS	N-tetradecyl-N,N-dimethyl-3-ammonio-1-propanesulfonate
TMS	Tetramethylsilane
Tyr-Leu	Tyrosine-Leucine
UV	Ultraviolet-visible

Chapter 1

Introduction

Macromolecules, such as proteins, and amphiphilic molecules, such as lipids, represent the main components of biological membranes in the living cell. The biological membrane separates the internal components of a biological cell from the outside environment and it acts as a selectively permeable barrier that controls the traffic of the molecules in and out of the biological cell.[1] Biological molecules such as proteins also represent important components in the ¨crowded environment¨of the biological cell where their concentration can reach 300-400 g/l.[2,3]

Macromolecules such as proteins and amphiphilic molecules show a tendency to form aggregates, with an average size based on the interactions among different species of the macromolecules. As an example, systems of charged surfactants or amphiphilics form spherical,[4,5] cylindrical,[4,5] and wormlike micellar aggregates,[6–12] a behavior that is attributed to the balance between the hydrophobic interaction and electrostatic repulsion.[4] These micellar systems find applications not only in biology, but also in technological applications such as heat-transfer fluids, oil-field drilling and drain openers.[13] Moreover, systems composed of polymer-surfactant molecules that form molecular aggregates and complexes have implementations in cosmetic and pharmaceutical applications.[14–16] On the other hand, many studies have been accomplished in the field of protein cluster formation (e.g. lysozyme cluster formation).[17–25] Protein aggregates are thought to play a

significant role in so called "conformational diseases".[26–28] These protein clusters are technically hard to quantify. It has been shown that the balance between a short-range attraction and long-range repulsion is responsible for the formation of mesoscopic clusters[17, 18, 20, 22, 24, 25] with finite size. However, conflicting reports over the existence of an equilibrium protein aggregate phase have emerged.[17–19]

The goal of this thesis is to investigate biologically relevant soft matter systems such as polymer-surfactant,[29] micellar, and protein systems[30] at different conditions of the system environment (i.e. dilute, semidilute, and concentrated molecular environment that partially mimics the intracellular environment) using nuclear magnetic resonance (NMR), where we provide quantitative answers for some important open questions: When do crowding effects become significantly important? What is the partitioning of different molecular species (i.e. monomers, aggregates, or micelles) in multi-component aggregates? What is the average size of the molecular aggregates? We address these questions by creating systems that partially mimic the intracellular "crowded environment" at which the dynamics and structure of macromolecular components are influenced. The Stokes-Einstein-Sutherland equation,[31, 32] $D = \frac{K_B T}{6\pi\eta R_H}$ relates a measured diffusion coefficient D with the solvent viscosity η and a physical quantity knows as the hydrodynamic radius R_H where K_B is the Boltzmann constant and T is the absolute temperature. This relation is strictly only valid at infinite dilution. For realistic, dense systems, one needs to work hard to obtain meaningful physical parameters from measured diffusion coefficients.

Scattering techniques such as dynamic light scattering[21, 33, 34] and neutron spin echo[20] can be used to analyze molecular motions and to extract molecular diffusion coefficients. However, there are unique aspects to NMR that can be both a complication and be used to one's advantage, such as combinations of chemical shift measurements, relaxation measurements (relaxometry), and diffusion measurements (diffusometry). As an example, chemical shift measurements (the one-dimensional spectrum) provide information about the chemical and electronic environment of detected nuclei (section 2.1.1). Relaxometry can be used to determine the relaxation mechanism

responsible for the relaxation process of the sample magnetization (section 2.1.2). Diffusometry is used to study the dynamics of molecules with spectral resolution in the chemical shift dimension (section 2.1.5.3).

Chapter 2 explains the basic concepts in NMR spectrometry. We present the density matrix formalism (density operator formalism) which is mainly used to describe the evolution of the magnetization during the pulse sequence. We discuss the two main relaxation processes (longitudinal and transverse relaxation processes) and the mechanism behind these relaxation processes. We then present the two-step relaxation mechanism, which is responsible for the relaxation process in micellar systems. Discussed next are two techniques (inversion recovery and spin echo technique) which are used to measure the longitudinal and transverse relaxation times of the molecules. We outline the main pulse sequences (pulsed-field gradient (PFG) spin echo and pulsed field gradient stimulated echo (PFG-STE)) which are used to measure the molecular self-diffusion coefficient. Finally, we discuss basic concepts in rheology including flow curves, oscillatory shear, and stress relaxation as well as a description of rheometer experimental details.

Chapter 3 includes an overview of the building blocks of self-assembly in polymers, surfactants, micelles, and proteins. We begin with general definitions for polymers, surfactants, and proteins. We then present the physical parameters which are used to characterize the average size of each of these building blocks (i.e. radius of gyration and hydrodynamic radius). In addition, we explain the self assembly of amphiphilic molecules to the micellar phase (i.e. spherical or cylindrical micelles).

In chapter 4, we elucidate the nature of polymer-surfactant aggregates in a model system composed of anionic surfactant sodium dodecyl sulfate (SDS) and nonionic polymer polyethylene oxide (PEO) in aqueous solution. We present the diffusion measurements, the relaxation measurements, and the chemical shift measurements of the PEO-SDS system in an aqueous solution over a wide range of SDS concentration. We introduce a self-consistent model that takes into account the fact that the surfactants are found in monomeric, aggregate, and micellar form. We use the

3

experimental data and the model to obtain the variation of the free monomer concentration and the free micellar concentration over the entire range of SDS concentration.

In chapter 5, we explore the dynamics and the structure of a micellar system composed of a zwitterionic surfactant N-tetradecyl-N,N-dimethyl-3-ammonio-1-propanesulfonate (TDPS) and anionic surfactant SDS in brine solution. We present complementary measurements diffusometry, relaxometry, deuterium NMR, and rheometry to explore the microstructure of this system. Also, we merge our experimental data with a restricted diffusion model and polymer theoretical models to obtain the average size of micelles and to show that these systems have properties very dependent on the length scale.

In chapter 6, we investigate evidence for the presence of an equilibrium phase composed of lysozyme monomers and aggregates in concentrated protein solutions. Therefore, we introduce previous work done on the lysozyme system in an aqueous solution, which includes formation of lysozyme aggregates, crystallization, and formation of equilibrium clusters. In addition, we present our diffusion and relaxation measurements for the lysozyme system. In all the work done, we obtain weight-averaged diffusion coefficients which must then be coupled with a reasonable model (for example monomer and aggregate states).

In chapter 7, we study the nature of peptide-micelle complexes in a 19-residue antimicrobial peptide (Gad2)-anionic surfactant (SDS), smaller dipeptides (Ala-Gly and Tyr-leu)-anionic surfactant (SDS) system, and anionic surfactant (SDS) system in an aqueous solution. We present the diffusion measurements and the relaxation measurements for the above mentioned systems over a range of SDS concentration. Using NMR-diffusometry we identify the onset of surfactant crowding on a peptide molecule beyond which hydrodynamic corrections to the diffusion coefficient are extremely important. Based on that, we extract the true hydrodynamic radius of Gad2-SDS aggregate over a range of SDS concentration below the SDS concentration at which crowding effects become important. For smaller dipeptides (Ala-Gly and Tyr-Leu)-SDS systems, diffusometry shows that dipeptides (Ala-Gly and Tyr-leu) do not affect significantly the aggregate nature of SDS

4

micelles. In addition, we compare the dynamics of a buffered SDS system with an unbuffered SDS/D_2O system. Diffusometry shows that the presence of a buffer in such an anionic surfactant system promotes the formation of SDS micelles.

5

Bibliography

[1] Neil A. Campbell, Jane B. Reece, Lisa A. Urry, Michael L. Cain, Steven A. Wasserman, Peter V. Minorsky, and Robert B. Jackson. *Biology*. Pearson Education Inc, San Francisco, USA, 8th edition, 2009.

[2] Julie E. Bryant. In-cell protein dynamics. *Molecular BioSystems*, 407:406–410, 2006.

[3] Reginald John Ellis. Macromolecular crowding: obvious but underappreciated. *Trends in Biochemical Sciences*, 26:597–604, 2001.

[4] Richard. A. L. Jones. *Soft Condensed Matter*. Oxford University Press Inc, New York, 1st edition, 2002.

[5] Jacob Israelachvili. *Intermolecular and Surface Forces*. Academic Press Limited, London, 2nd edition, 1991.

[6] Cecile A. Dreiss. Wormlike micelles: where do we stand? Recent developments, linear rheology and scattering techniques. *Soft Matter*, 3:956–970, 2007.

[7] Mike E. Cates and Sauveur-Jean Candau. Statics and dynamics of worm-like surfactant micelles. *Journal of Physics: Condensed Matter*, 2:6869–6892, 1990.

[8] Toshiyuki Shikata and Hirotaka Hirata. Micelle formation of detergent molecules in aqueous media: Viscoelastic properties of aqueous cetyltrimethylammonium bromide solutions. *Langmuir*, 3:1081–1086, 1987.

[9] R. Messager, A. Ott, D. Chatenay, W. Urbach, and D. Langevin. Are giant micelles living polymers? *Physical Review Letters*, 60:1410–1413, 1988.

[10] Sauveur-Jean Candau and R. Oda. Linear viscoelasticity of salt-free wormlike micellar solutions. *Colloids and Surfaces A: Physicochemical and Engineering Aspects*, 183-185:5–14, 2001.

[11] Richard D. Koehler, Srinivasa R. Raghavan, and Eric W. Kaler. Microstructure and dynamics of wormlike micellar solutions formed by mixing cationic and anionic surfactants. *The Journal of Physical Chemistry B*, 104:11035–11044, 2000.

[12] David Lopez-Diaz and Rolando Castillo. The wormlike micellar solution made of a zwitterionic surfactant (TDPS), an anionic surfactant (SDS), and brine in the semidilute regime. *The Journal of Physical Chemistry B*, 114:8917–8925, 2010.

[13] Jiang Yang. Viscoelastic wormlike micelles and their applications. *Current Opinion in Colloid & Interface Science*, 7:276–281, 2002.

[14] E. Desmond Goddard and James V. Gruber. *Principles of Polymer Science and Technology in Cosmetics and Personal Care*. Marcel Dekker Inc, Dekker, New York London, 1st edition, 1999.

[15] Francoise M. Winnik and Sudarshi T.A. Regismond. Fluorescence methods in the study of the interactions of surfactants with polymers. *Colloids and Surfaces A: Physicochemical and Engineering Aspects*, 118:1–39, 1996.

7

[16] E. Desmond Goddard. Polymer-surfactant interaction part 1. uncharged water-soluble polymers and charged surfactants. *Colloids and Surfaces*, 19:255–300, 1986.

[17] Anna Stradner, Helen Sedgwick, Frederic Cardinaux, Wilson C. K. Poon, Stefan U. Egelhaaf, and Peter Schurtenberger. Equilibrium cluster formation in concentrated protein solutions and colloids. *Nature*, 432:492–495, 2004.

[18] Anna Stradner, Frederic Cardinaux, and Peter Schurtenberger. A small-angle scattering study on equilibrium clusters in lysozyme solutions. *The Journal of Physical Chemistry B*, 110:21222–21231, 2006.

[19] Anuj Shukla, Efstratios Mylonas, Emanuela Di Cola, Stephanie Finet, Peter Timmins, Theyencheri Narayanan, and Dmitri I. Svergun. Absence of equilibrium cluster phase in concentrated lysozyme solutions. *Proceedings of the National Academy of Sciences*, 105:5075–5080, 2008.

[20] Lionel Porcar, Peter Falus, Wei-Ren Chen, Antonio Faraone, Emiliano Fratini, Kunlun Hong, Piero Baglioni, and Yun Liu. Formation of the dynamic clusters in concentrated lysozyme protein solutions. *The Journal of Physical Chemistry Letters*, 1:126129, 2009.

[21] Jaroslaw Poznanski, Jedrzej Szymanski, Teresa Basinska, Stanislaw Slomkowski, and Wojciech Zielenkiewicz. Aggregation of aqueous lysozyme solutions followed by dynamic light scattering and ^{1}H NMR spectroscopy. *Journal of Molecular Liquids*, 121:21–26, 2005.

[22] Yun Liu, Emiliano Fratini, Piero Baglioni, Wei-Ren Chen, and Sow-Hsin Chen. Effective long-range attraction between protein molecules in solutions studied by small angle neutron scattering. *Physical Review Letters*, 95(118102):1–4, 2005.

[23] N. Niimura, Y. Minezaki, M. Ataka, and T. Katsura. Aggregation in supersaturated lysozyme solution studied by time-resolved small angle neutron scattering. *Journal of Crystal Growth*, 154:136–144, 1995.

[24] Sean R. McGuffee, , and Adrian H. Elcock. Atomically detailed simulations of concentrated protein solutions: The effects of salt, pH, point mutations, and protein concentration in simulations of 1000-molecule systems. *Journal of the American Chemical Society*, 128:12098–12110, 2006.

[25] Fredrik Carlsson, Martin Malmsten, and Per Linse. Monte carlo simulations of lysozyme self-association in aqueous solution. *The Journal of Physical Chemistry B*, 105:12189–12195, 2001.

[26] Jim Schnabel. Protein folding: The dark side of proteins. *Nature*, 464:828–829, 2010.

[27] Ron R. Kopito and David Ron. Conformational disease. *Nature Cell Biology*, 2:E207–E209, 2000.

[28] Adriano Aguzzi and Tracy O'Connor. Protein aggregation diseases: pathogenicity and therapeutic perspectives. *Nature Reviews Drug Discovery*, 9:237–248, 2010.

[29] Suliman Barhoum and Anand Yethiraj. An NMR study of macromolecular aggregation in a model polymer-surfactant solution. *The Journal of Chemical Physics*, 132:19, 2010.

[30] Suliman Barhoum and Anand Yethiraj. NMR detection of an equilibrium phase consisting of monomers and clusters in concentrated lysozyme solutions. *The Journal of Physical Chemistry B*, 114:17062–17067, 2010.

[31] Albert Einstein. Zur theorie der brownschen bewegung. *Annalen der Physik*, 17:549–550, 1906.

[32] William Sutherland. A dynamical theory of diffusion for non-electrolytes and the molecular mass of albumin. *Philosophical Magazine and Journal of Science*, 54:781–785, 1905.

[33] Yannis Georgalis, Patrick Umbach, Jannis Raptis, and Wolfram Saenger. Lysozyme aggregation studied by light scattering. I. influence of concentration and nature of electrolytes. *Acta Crystallographica Section D*, D53:691–702, 1997.

[34] Shirish Chodankara, Vinod K. Aswala, Joachim Kohlbrecher, Puthusserickal A. Hassanc, and Apoorva G. Wagh. Time evolution of crystallization phase of lysozyme protein in aqueous salt solution as studied by scattering techniques. *Physica B: Condensed Matter*, 398:164–171, 2007.

Chapter 2

Experimental Techniques

Nuclear magnetic resonance (NMR) based techniques are used to study the dynamics and the structure of the macromolecules in multi-component polymer-surfactant (chapter 4), micellar (chapter 5), protein (chapter 6), and peptide-surfactant (chapter 7) solutions. Complementary techniques, including chemical shift measurement, NMR relaxometry, and NMR diffusometry are utilized to extract quantitative information about the chemical environment of the detected nuclei, and the dynamics and structure of macromolecular self-assemblies in the above mentioned systems. In one of the studies (chapter 5), we have used rheology as well as NMR-based techniques in order to construct a comprehensive picture of the microscopic structure in a mixed-surfactant wormlike micellar system.

2.1 Nuclear magnetic Resonance (NMR)

Nuclear Magnetic Resonance (NMR) is the study of the magnetic interaction between an oscillating magnetic field with atomic nuclei inside a sample that is exposed to a strong external uniform magnetic field. All atomic nuclei contain protons and neutrons which possess spin angular momentum (I) with $2I+1$ degenerate sublevels. In a magnetic field $\vec{B_o}$, degeneracy is broken such that

each energy state of 2I+1 sublevels will possess slightly different energy $E = -\vec{\mu} \cdot \vec{B_o} = -\gamma \hbar m_\ell B_o$ where γ is the nuclear gyromagnetic ratio, $\vec{\mu} = \hbar \gamma \vec{I}$ is the magnetic dipole moment, and m_ℓ is the magnetic dipole moment quantum number of the energy state in each sublevel. Atomic nuclei with an even number of protons and an even number of neutrons are classified as non-detectable nuclei because the ground state nuclear spin I=0 (examples are ^{12}C and ^{16}O). Detectable nuclei can be further classified into nuclei with even mass number but an odd number of protons and an odd number of neutrons (where the ground state nuclear spin I is an integer) such as ^2H and nuclei with an odd mass number (where the ground state nuclear spin I is a half integer) such as ^1H, ^{15}N, ^{13}C.[1,2]

The experiments in the thesis focus on "proton NMR", i.e. with samples containing ^1H nuclei (with spin 1/2) as the primary detected nuclei. Many of our experiments are also conducted with deuterated solvent (i.e. containing ^2H nuclei with spin 1), and some experiments are carried out with samples containing ^2H labeled nuclei.

A typical NMR sample containing water has on the order of 10^{23} spin-1/2 nuclei, and the nuclear spin orientation (magnetic dipole moment) is either parallel ("spin up" state) or anti-parallel ("spin down" state) with respect to the direction of applied magnetic field. This magnetic field is by convention chosen to be along the z-axis ($\vec{B_o} = B_o \hat{k}$). However, the alignment of the nuclear spins with respect to the direction of the magnetic field is perturbed by the thermal motion of the molecules which are responsible for the random orientations of the nuclear spins inside the sample. Thus, in the presence of an external applied magnetic field, the magnetic dipole moment of a nuclear spin might align in such a way as to possess three different components: a longitudinal component along the z-axis and two transverse components in the xy-plane. The transverse components for all nuclear spins over the entire sample cancel out whereas there is a slight net orientation of longitudinal components parallel to the applied magnetic field. This is responsible for a small net bulk magnetization. Under these circumstances, the population ratio of

nuclear spins in the spin up and the spin down states is given by the Boltzmann distribution:[1]

$$\frac{n_{\beta,eq}}{n_{\alpha,eq}} = \exp\left(\frac{-\Delta E}{K_B T}\right) \qquad (2.1)$$

where $n_{\alpha,eq}$ and $n_{\beta,eq}$ are the equilibrium populations in the spin up state (α) and spin down state (β) respectively, ΔE is the energy difference between both states, K_B is the Boltzmann constant, and T is the absolute temperature. In addition, the z-component of the sample magnetization is proportional to the difference in populations between the spin up and spin down state:[1]

$$M_z \propto (n_{\alpha} - n_{\beta}). \qquad (2.2)$$

At equilibrium, the net magnetization of the sample is along the direction of $\vec{B}_o$ (the z-axis). However, if the magnetization is flipped away from the z-axis, the sample magnetization will experience a torque from the magnetic field $\vec{B}_o$ which drives the magnetization vector to precess about the direction of the magnetic field at the Larmor frequency, $\omega_0 = -\gamma B_o$. Our NMR experiments have been carried out using a NMR spectrometer that operates with a magnetic field $B_o = 14$ T. Therefore, the Larmor frequency of ^1H nucleus is ≈ 600 MHz while the Larmor frequency of the ^2H nucleus is $\approx 91 \times 10^6$ Hz. The frequency of the radio waves is in the range ≈ 0.3 MHz to ≈ 300 GHz; thus magnetic resonance experiments such as electron spin resonance and NMR are possible with electromagnetic fields oscillating at radio frequency.

2.1.1 One Dimensional NMR Spectroscopy

One of the simplest magnetic resonance experiments is one in which the sample magnetization experiences a short radio-frequency (RF) pulse in the transverse direction of the sample magnetization with a frequency close to the Larmor frequency. This RF pulse tilts the magnetization away from the z-axis. After turning off the RF-pulse, the precessional motion of the sample magnetization about $\vec{B}_o$ creates an oscillatory electric current in a radio-frequency tuned receiver coil. This

13

current is digitized and recorded as a "free induction decay" (FID) signal in the time domain. This signal has two (x and y) components. One can alternatively and equivalently write the signal as a complex time domain signal. Using the Fourier transform, the FID is transformed to a frequency domain signal that has a real and an imaginary component. The real component of the frequency domain signal represents the one dimensional 1D NMR spectrum. It includes peaks of one type of nucleus at different frequency positions based on the chemical and electronic environment of the detected nucleus.[1,2]

2.1.1.1 Chemical Shift and 1D Spectrum

The external magnetic field $\vec{B_0}$ in an NMR spectrometer interacts indirectly with detectable sample nuclei through the electron clouds around the nuclei. The magnetic field $\vec{B_0}$ induces electronic currents in the chemical environment around the nuclei. These electronic currents create an induced magnetic field that is called secondary magnetic field at the nuclear spin sites, which affects slightly the value of the nuclear Larmor frequency ω_0. Thus, nuclei of the same isotope in different chemical environments can have slightly different values of Larmor frequency. Nuclei which are bonded or close to electronegative chemical groups or electronegative elements are more exposed to the NMR external magnetic field B_o. Thus, these are referred to as deshielded nuclei. Nuclei which are not bonded to any electronegative chemical groups or electronegative elements are less exposed to the NMR external magnetic field. Thus, these are referred to as shielded nuclei.[1,2]

Since the value of a nuclear Larmor frequency ω_0 depends on the value of the operating magnetic field strength B_o of the NMR spectrometer, then for different NMR spectrometers which operate at different field strengths, the same nuclei at the same chemical environment have different values of Larmor frequency and so different peak positions on the frequency scale. In order to compare the peak positions in the 1D spectra between NMR spectrometers which operate at different fields, a chemical shift scale is defined as a magnetic field independent scale. On this scale, the peak position is reported by measuring the peak's frequency ν_i relative to a reference peak

14

frequency ν_{ref} of a known compound. Tetramethylsilane (TMS), with chemical formula $(CH_3)_4Si$, is the most common standard reference compound for proton NMR. TMS is typically chosen as a reference in organic solvents because it is chemically inert and has a single peak NMR spectrum. Thus, the peak position in the chemical shift scale is defined by the following equation[1,2]

$$\delta(ppm) = \frac{\nu_i - \nu_{ref}}{\nu_{spectrometer}} \times 10^6 \qquad (2.3)$$

where $\nu_{spectrometer}$ is the NMR spectrometer frequency and the position of the standard reference compound is defined to be at 0 ppm on the chemical shift scale.

In an NMR 1D spectrum, the more shielded nuclei have lower chemical shift values than the less shielded nuclei. Thus, on the chemical shift scale when the chemical shift value of a peak increases (more leftwards by convention), this indicates that the chemical environment of the detected nucleus is changing such that the nucleus is being less shielded.

Figure 2.1 shows the 1D NMR spectrum of protons in a polymer-surfactant solution that is discussed and presented in chapter 4. The spectrum includes six peak regions which have different chemical shift values. The one with the lowest chemical shift value represents the peak of protons in the CH_3 chemical group (SDS4) which are the most shielded protons. The peak with the highest chemical shift value represents protons on the OH chemical group which are less shielded since they are bonded to an electronegative element O. All the peaks in the spectrum are broad peaks that consist several peaks.

2.1.1.2 The Radio-Frequency Pulse and the Rotating Frame

The equilibrium sample magnetization is perturbed by applying a radio-frequency (RF) pulse that generates an oscillating magnetic field. Assuming that the oscillating magnetic field $\overrightarrow{B_{RF}}(t)$ is along the x-axis,[2] we may write (following Levitt[2])

$$\overrightarrow{B_{RF}}(t) = B_{RF}\cos(\omega_{ref}t + \phi_p)\hat{i} \qquad (2.4)$$

15
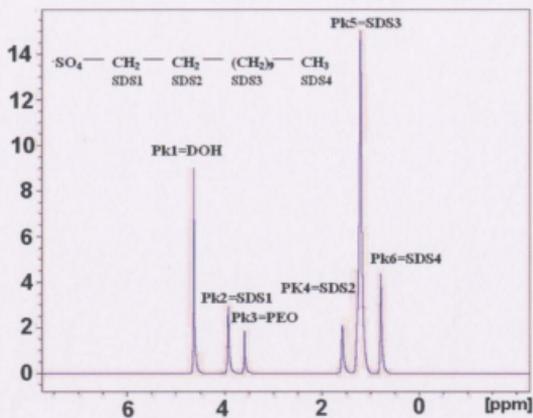
Figure 2.1: One-dimensional ^{1}H – NMR spectrum for a solution containing a polymer (polyethylene oxide) and a surfactant (sodium dodecyl sulfate) in D_2O solvent at a sample temperature 298 K. Inset: the chemical formula of the SDS molecule. A 1 ppm chemical shift corresponds to a 600 Hz frequency shift.

where B_{RF} has a maximum radio frequency amplitude, ω_{ref} is the frequency of the RF pulse, and ϕ_p is the phase shift of the radio frequency pulse. As stated in section 2.1, as soon as the RF pulse is turned off, the sample magnetization will experience a precessional motion about the direction of the magnetic field B_o with a Larmor frequency $\omega_o = -\gamma B_o$. We therefore write $\overrightarrow{B_{RF}}(t)$ as a linear combination of two counter-rotating (clockwise and counterclockwise) magnetic fields components. One of the components is rotating in the same sense as the nuclear spin does and is known as the resonant component $\overrightarrow{B_{res}^{RF}}(t)$ of the oscillating magnetic field $\overrightarrow{B_{RF}}(t)$ while the other component is rotating in the opposite direction of the spin precession and is termed as non-resonant component $\overrightarrow{B_{non-res}^{RF}}(t)$ of the oscillating magnetic field $\overrightarrow{B_{RF}}(t)$. We write[2]

$$
\begin{aligned}
\overrightarrow{B_{RF}}(t) &= \frac{B_{RF}}{2}\left[\cos(\omega_{ref}t + \phi_p)\hat{i} + \sin(\omega_{ref}t + \phi_p)\hat{j}\right] \\
&+ \frac{B_{RF}}{2}\left[\cos(\omega_{ref}t + \phi_p)\hat{i} - \sin(\omega_{ref}t + \phi_p)\hat{j}\right] = \overrightarrow{B_{res}^{RF}}(t) + \overrightarrow{B_{non-res}^{RF}}(t)
\end{aligned}
\tag{2.5}
$$

where $\overrightarrow{B_{res}^{RF}}(t) = \frac{B_{RF}}{2}\cos(\omega_{ref}t + \phi_p)\hat{i} + \frac{B_{RF}}{2}\sin(\omega_{ref}t + \phi_p)\hat{j}$ and $\overrightarrow{B_{non-res}^{RF}}(t) = \frac{B_{RF}}{2}\cos(\omega_{ref}t + \phi_p)\hat{i} - \frac{B_{RF}}{2}\sin(\omega_{ref}t + \phi_p)\hat{j}$.

In the presence of a strong external static magnetic field B_o, the resonant component $\overrightarrow{B_{res}^{RF}}(t)$ has the dominant direct effect on the orientation of the nuclear spin, while the effect of the non-resonant component is negligible.[2]

In the presence of both B_o and $\overrightarrow{B_{RF}}(t) \approx \overrightarrow{B_{res}^{RF}}(t)$, the spin Hamiltonian in the laboratory frame is written as

$$
\hat{H}(t) = -\overrightarrow{\mu_i}.\left[\overrightarrow{B_o} + \overrightarrow{B_{res}^{RF}}(t)\right] = \omega_0\hat{I}_z - \frac{1}{2}\gamma B_{RF}\left(\cos(\omega_{ref}t + \phi_p)\hat{I}_x + \sin(\omega_{ref}t + \phi_p)\hat{I}_y\right)
\tag{2.6}
$$

where $\hbar$ is considered to be one and γ is the gyromagnetic ratio of the nuclear spin i. $\hat{I}_z$, $\hat{I}_x$, and $\hat{I}_y$ are quantum mechanical operators which represent z, x, and y components of the nuclear angular momentum. In the matrix representation, and including the unit matrix, they are[2]

17

$$\hat{I}_z = \frac{1}{2}\begin{pmatrix} 1 & 0 \\ 0 & -1 \end{pmatrix} \qquad (2.7a)$$

$$\hat{I}_x = \frac{1}{2}\begin{pmatrix} 0 & 1 \\ 1 & 0 \end{pmatrix} \qquad (2.7b)$$

$$\hat{I}_y = \frac{1}{2}\begin{pmatrix} 0 & -i \\ i & 0 \end{pmatrix} \qquad (2.7c)$$

$$\hat{I} = \begin{pmatrix} 1 & 0 \\ 0 & 1 \end{pmatrix} \qquad (2.7d)$$

We can see clearly from equation 2.6 that the spin Hamiltonian is a time dependent Hamiltonian. In order to simplify the spin Hamiltonian expression, a mathematical trick is considered by assuming that the xy-plane is rotating in the same sense as the resonant component B_{res}^{RF} of the RF pulse (i.e. the same sense as the nuclear spin precession). In this reference frame, the resonant component B_{res}^{RF} of the RF pulse appears to be static and aligned along x-axis. This is the ``rotating frame'' in NMR. In the rotating frame, the wave function of the spin $|\widetilde{\psi}>$ is related to the wave function $|\psi>$ of the spin in the laboratory frame by a rotation operator,[2]

$$|\widetilde{\psi}> = \exp(i\Phi\hat{I}_z|\psi>) = \begin{pmatrix} \exp(i\Phi/2) & 0 \\ 0 & \exp(-i\Phi/2) \end{pmatrix}|\psi> = \hat{R}_z(-\Phi)|\psi>. \qquad (2.8)$$

where $\Phi = \omega_{ref}t + \phi_{ref}$ and ω_{ref} is the frequency of the resonant component B_{res}^{RF} of the RF pulse. Using the time-dependent Schroedinger equation in the rotating frame[2]

$$\frac{d}{dt}[|\widetilde{\psi}>] = \frac{d}{dt}[\hat{R}_z(-\Phi)|\psi>] = -i\widetilde{\hat{H}}|\widetilde{\psi}> \qquad (2.9)$$

it can be shown that the relation between the spin Hamiltonian in the rotating frame $\widetilde{H}$ and the laboratory frame $\hat{H}$ is given as[2]

$$\overline{H} = \hat{R}_z(-\Phi)\hat{H}\hat{R}_z(\Phi) - \omega_{ref}\hat{I}_z. \tag{2.10}$$

Combining both equation 2.6 and equation 2.10, we obtain the spin Hamiltonian in the rotation frame as a time independent Hamiltonian[2]

$$\overline{H} = \Omega_0\hat{I}_z - \frac{\gamma B_{RF}}{2}(\hat{I}_x\cos(\phi_p - \phi_{ref}) + \hat{I}_y\sin(\phi_p - \phi_{ref})) \tag{2.11}$$

where $\Omega_0 = \omega_0 - \omega_{ref}$ is called the relative Larmor frequency or the offset frequency and $\omega_{nut} = |\frac{1}{2}\gamma B_{RF}|$ $= |\frac{1}{2}B_{RF}\omega_0/B_0|$ is called the nutation frequency. ϕ_{ref} is the phase of the rotating frame, which is defined to simplify mathematical calculations. For nuclear spins with $\gamma > 0$, both the Larmor frequency ω_0 and ω_{ref} (i.e; the frequency of reference frame) are negative, while for nuclear spins with $\gamma < 0$, both the Larmor frequency ω_0 and ω_{ref} are positive. Therefore, ϕ_{ref} is considered by convention to be either π for $\gamma > 0$ or 0 for $\gamma < 0$. Based on that, equation 2.11 is written as[2]

$$\overline{H} = \Omega_0\hat{I}_z + \omega_{nut}(\hat{I}_x\cos(\phi_p) + \hat{I}_y\sin(\phi_p)). \tag{2.12}$$

2.1.1.3 The Density Operator and Phase Coherence

Any sample includes a large number of nuclear spins which contribute to create both the longitudinal magnetization M_z and transverse magnetization M_x and M_y. The wavefunction $|\psi>$ of a single spin-1/2 nucleus is given by a linear combination of the spin-up and spin-down eigenstates, i.e. $|\psi> = C_\alpha|\alpha> + C_\beta|\beta>$, where $|\alpha>$ and $|\beta>$ are the spin up $(|+1/2>)$ and the spin down $(|-1/2>)$ state.[1]

For a sample with spin-1/2 nuclei, the longitudinal z-component of the bulk magnetization and the transverse xy magnetizations M_x and M_y are proportional to the sum of an average contribution of each spin in the longitudinal magnetization M_z and transverse magnetization components M_x and M_y[1]

$$M_z = \sum_{i=1}^{N} \gamma < I_z >_i = N\gamma\overline{< I_z >} = \frac{1}{2}\gamma N\left(|C_\alpha|^2 - |C_\beta|^2\right) \tag{2.13a}$$

19

$$M_x = \sum_{i=1}^{N} \gamma < I_x >_i = N\gamma \overline{< I_x >} = \frac{1}{2}\gamma N \left(C_\alpha^* C_\beta + C_\beta^* C_\alpha \right) \qquad (2.13b)$$

$$M_y = \sum_{i=1}^{N} \gamma < I_y >_i = N\gamma \overline{< I_y >} = \frac{1}{2} i \gamma N \left(C_\alpha C_\beta^* - C_\beta C_\alpha^* \right) \qquad (2.13c)$$

where $< I_z > = <\psi|I_z|\psi>$. Also, $|C_\alpha|^2$ and $|C_\beta|^2$ are the probabilities of finding a spin in the spin up state $|\alpha >$ (i.e. $|+1/2>$ state) and spin down state $|\beta >$ (i.e. $|-1/2>$ state) respectively. The population of the α or β state is proportional to the sum of probabilities $|C_\alpha|^2$ or $|C_\beta|^2$ of each spin respectively.

Since we are dealing with a huge number of nuclear spins, the density matrix formalism is used to simplify the prediction process of the sample magnetization components during the NMR pulse sequence. An operator called the density operator $\hat{\rho}$ is introduced and can be represented in matrix form[1]

$$\hat{\rho} = \overline{|\psi> <\psi|} = \begin{pmatrix} \rho_{\alpha\alpha} & \rho_{\alpha\beta} \\ \rho_{\beta\alpha} & \rho_{\beta\beta} \end{pmatrix} = \begin{pmatrix} \overline{|C_\alpha|^2} & \overline{C_\alpha C_\beta^*} \\ \overline{C_\beta C_\alpha^*} & \overline{|C_\beta|^2} \end{pmatrix} \qquad (2.14)$$

Based on equation 2.14, we are able to write the sample magnetization components (e.g equations 2.13a, 2.13b and 2.13c) in terms of the density matrix elements[1]

$$M_z = \frac{1}{2}\gamma N \left(\rho_{\alpha\alpha} - \rho_{\beta\beta} \right) \qquad (2.15a)$$

$$M_x = \frac{1}{2}\gamma N \left(\rho_{\beta\alpha} + \rho_{\alpha\beta} \right) \qquad (2.15b)$$

$$M_y = \frac{1}{2} i \gamma N \left(\rho_{\alpha\beta} - \rho_{\beta\alpha} \right) \qquad (2.15c)$$

Also, the population of the nuclear spins in the spin up and spin down states are given in term of the density matrix elements: $n_\alpha = N \rho_{\alpha\alpha}$ and $n_\beta = N \rho_{\beta\beta}$. However, we mentioned in

section 2.1 that at the equilibrium, n_α and n_β are given in terms of the Boltzmann distribution: $n_{\alpha,eq} = (1/2)N \exp\left(-E_\alpha/K_BT\right)$ and $n_{\beta,eq} = (1/2)N \exp\left(-E_\beta/K_BT\right)$.[1]

We conclude from the mathematical representation of M_z, M_x, and M_y (i.e. equation 2.15a to equation 2.15c) that a combination of the density operator diagonal elements is proportional to the sample longitudinal magnetization. On the other hand, combinations of the density operator off-diagonal elements are proportional to the sample transverse magnetization. More specifically, the diagonal elements $\rho_{\alpha\alpha}$ and $\rho_{\beta\beta}$ represent the "population" of the $|\alpha>$ state and the $|\beta>$ state respectively, while the off-diagonal elements $\rho_{\beta\alpha}$ and $\rho_{\alpha\beta}$ are called "coherences".[1,2]

Each element in the density matrix connects one state ($|\alpha>$ or $|\beta>$) with another. As noted in section 2.1.3, where coherence order is defined, the coherence order of both $\rho_{\alpha\alpha}$ and $\rho_{\beta\beta}$ are zero, while the coherence orders of $\rho_{\beta\alpha}$ and $\rho_{\alpha\beta}$ are -1 and +1 respectively. At equilibrium, the net magnetization of the sample is along the z-axis ($M^{eq} = M_z^{eq}$), while there are no transverse components M_x^{eq} and M_y^{eq}. Thus, at equilibrium, the amplitude of +1 and -1 coherence order elements $\rho_{\beta\alpha}$ and $\rho_{\alpha\beta}$ are zero,[1,2]

$$\hat{\rho}^{eq} = \begin{pmatrix} \rho_{\alpha\alpha}^{eq} & 0 \\ 0 & \rho_{\beta\beta}^{eq} \end{pmatrix} \tag{2.16}$$

where $\rho_{\alpha\alpha}^{eq}$ and $\rho_{\beta\beta}^{eq}$ represents the population of $|\alpha>$ and $|\beta>$ states at equilibrium. They are given as follows[2]

$$\rho_{\alpha\alpha}^{eq} = \frac{\exp\left(-E_\alpha/K_BT\right)}{\exp\left(-E_\alpha/K_BT\right) + \exp\left(-E_\beta/K_BT\right)} \approx \frac{1}{2}\left(1 - E_\alpha/K_BT\right) \tag{2.17}$$

$$\rho_{\beta\beta}^{eq} = \frac{\exp\left(-E_\beta/K_BT\right)}{\exp\left(-E_\alpha/K_BT\right) + \exp\left(-E_\beta/K_BT\right)} \approx \frac{1}{2}\left(1 - E_\beta/K_BT\right) \tag{2.18}$$

where $E_\alpha = -\frac{\gamma B_o}{2}$ and $E_\beta = \frac{\gamma B_o}{2}$, so equation 2.16 can be modified

$$\hat{\rho}^{eq} = \begin{pmatrix} \frac{1}{2}\left(1 - E_\alpha/K_BT\right) & 0 \\ 0 & \frac{1}{2}\left(1 - E_\beta/K_BT\right) \end{pmatrix} = \frac{1}{2}\hat{I} + \frac{\gamma B_o}{2K_BT}\hat{I}_z \tag{2.19}$$

According to equations 2.13a, 2.13b, and 2.13c:

$$M_z^{eq} = \frac{(\gamma)^2 N B_o}{4 K_B T}$$

$$M_x^{eq} = M_y^{eq} = 0 \qquad (2.20)$$

Equation 2.14 can be rewritten in order to use it in the rotating frame.[1,2] As we mentioned, in the rotating frame the xy-plane rotates in the same sense as the resonant component of the RF-pulse B_{res}^{RF} and in the same sense as the nuclear spin precession. According to this approach, B_{res}^{RF} appears to be oriented along x-axis while the relation between the spin wave function $|\widetilde{\psi}>$ in rotating frame and the spin wave function $|\psi>$ in laboratory frame is given by equation 2.9. Based on equation 2.9, we can write a general evolution expression of the density operator $\widetilde{\rho}$ in the rotating frame[1,2]

$$\widetilde{\rho}_2 = \exp\left(-i\widetilde{H}t\right) \overline{|\widetilde{\psi}><\widetilde{\psi}|}_1 \exp\left(i\widetilde{H}t\right) = \exp\left(-i\widetilde{H}t\right) \hat{\rho}_1 \exp\left(i\widetilde{H}t\right) \qquad (2.21)$$

Equation 2.21 is used to detect the evolution of the sample magnetization components at any time period during the NMR pulse sequence.

As an example, one can easily identify the evolution of the sample magnetization during the pulse sequence for the basic pulse-acquire experiment. The sample magnetization at equilibrium is represented by the density operator $\hat{I}_z$ which experiences a $(\pi/2)_x$ pulse. Equation 2.21 then gives $\widetilde{\rho}_2 = \exp\left(-i(\pi/2)\,\hat{I}_x\right)\hat{I}_z \exp\left(i(\pi/2)\,\hat{I}_x\right) = \cos(\pi/2)\,\hat{I}_z - \sin(\pi/2)\,\hat{I}_y = -\hat{I}_y$.

2.1.2   NMR Relaxation

Relaxation is the process by which the density operator (equation 2.14) returns to its equilibrium value (equation 2.16) and the sample magnetization (given by equation 2.13a, 2.13b, 2.13c) recovers its equilibrium value along the direction of the applied magnetic field in the absence of an RF perturbation. In general, relaxation processes in NMR are classified into two types: longitudinal relaxation and transverse relaxation processes.[1,2]

2.1.2.1 Longitudinal T_1 Relaxation

Longitudinal relaxation is the process during which the longitudinal component of the sample magnetization re-establishes its maximum value along the direction of the applied magnetic field.[1] A nuclear spin inside the sample experiences both an external uniform magnetic field B_o and internal oscillating local fields B_{loc}. One of the origins of these local fields is the magnetic fields which are created and associated with magnetic dipole moments of nearby nuclear spins inside the sample. Because of resonance, local fields that happen to be oscillating at close to the Larmor frequency have a disproportionately large effect in rotating a magnetic moment to new directions just like an applied resonance pulse.[1] In addition, the direction and the magnitude of these local fields at nuclear sites change continuously due to the thermal motion of molecules. According to the Boltzmann distribution in equation 2.1, the population of nuclear spins in the lower energy state is higher than in the higher energy state. The local fields will either rotate a given spin towards or away from the z-axis. However, the Boltzmann distribution (equation 2.1) ensures that the rotation towards the z-axis are more frequent than the rotation away from the z-axis.[1] Thus, the magnetization is driven to equilibrium by thermal motions.

The above termed mechanism is often refer as ``non-secular''contribution (i.e. arising from local fields oscillating at frequencies close to the Larmor frequency) to transverse relaxation; when the longitudinal magnetization relaxes back to equilibrium, so does the transverse magnetization.

2.1.2.2 Transverse Magnetization and T_2 Relaxation

In equilibrium, there is a net longitudinal magnetization, which is practically undetectable in comparison with the diamagnetic effect. NMR therefore typically involves $(\frac{\pi}{2})_x$ or $(\frac{\pi}{2})_y$ pulses which rotate the nuclear spins into the xy-plane. In the presence of uniform external magnetic field B_o, these spins precess in synchronization with the Larmor frequency and thus the macroscopic transverse magnetization also undergoes precessional motion.[1,2]

Transverse relaxation is the process during which the transverse (x and y) components of the sample magnetization (M_x and M_y in equation 2.13b and equation 2.13c) decay to zero.[1] In the presence of nearby nuclear spins, a nuclear spin will precess about the direction of the uniform magnetic field with a frequency which is proportional to the sum of both B_o and the net z-component of the local field $B_{z,loc}$[1]

$$\omega = -\gamma(B_o + B_{z,loc}) \tag{2.22}$$

where $B_o \gg B_{z,loc}$ but the amplitude of the local field and the z-component of the local field $B_{z,loc}$ vary at different nuclear spin locations in the sample. The nuclear spins will precess at slightly different values of Larmor frequency. This causes a loss in synchronization, and results in an irreversible decay in the macroscopic transverse magnetization. This mechanism is often called "secular" contribution to transverse relaxation that arises from the z-component of local fields varying from one spin to spin. In NMR, the peak width is directly proportional to transverse relaxation rate. Therefore, losing synchronization due to secular contribution caused a peak broadening that is called homogeneous broadening. However, another broadening in a NMR peak might be caused due to the existence of an inhomogeneous magnetic field. This peak broadening is called inhomogeneous broadening.[1]

Both the longitudinal T_1 relaxation time and the transverse T_2 relaxation time are related to a fundamental molecular rotational correlation time τ_c. In all cases $T_1(ms - s) \geqslant T_2(ms - s) \ggg \tau_c(ps - ns)$. We discuss the relationship of the relaxation times (or rates) to the molecular mechanism in section 2.1.2.3.

2.1.2.3 Relaxation Mechanisms, the Correlation Function, and Spectral Density

There are three dominant relaxation mechanisms in spin-1/2 nuclei. They are:[1,2]

• Dipole-dipole relaxation. This is attributed to the creation of local fields at nuclear spin sites

24

due to the direct dipole-dipole interaction between the nuclear spins.

- Chemical shift anisotropy relaxation. This is attributed to the creation of local fields at the nuclear spin sites due to the presence of a non-spherical distribution of electron clouds around the nuclear spins. Thus, in the presence of the external static NMR magnetic field B_o, an induced electrical current (in the electronic clouds) is created which itself creates local fields at the nuclear spin sites (transverse and longitudinal local field components).

- Relaxation due to paramagnetic impurities. This is attributed to the creation of local fields at the nuclear spin sites from the unpaired electrons in a dissolved impurity such as O_2.

In all cases, the mechanism generates local fields which then fluctuate due to molecular motions. The rotational diffusional motions of molecules are in the frequency range between 10^7 and 10^{10} Hz, which spans the range of the typical Larmor frequency.[1] This is an indication that molecular rotational diffusion is the most effective molecular motion in the relaxation process. In order to identify and characterize the random molecular rotational diffusion quantitatively, a mathematical function called the correlation function $G(\tau)$ is used to identify how rapidly the oscillating local magnetic field is fluctuating with time:

$$G(\tau) = \frac{1}{N} \sum B_{loc,i}(t) B_{loc,i}(t + \tau) = \overline{B_{loc}(t) B_{loc}(t + \tau)} \qquad (2.23)$$

Equation 2.23 represents the ensemble average over all nuclear spins in the sample volume. For rotational diffusion in a simple viscous solvent this correlation function exhibits a simple exponential decay $G(\tau) = \overline{B_{loc}^2(t)} \exp(-|\tau|/\tau_c)$. τ_c is the correlation time of the molecular motion and can be related to the solvent viscosity η_s: $\tau_c = 4\pi\eta(R_H)^3/(3K_B T)$.[3] The molecular rotational diffusion is attributed to the collisions of a molecule with other nearby molecules in the solution such that with the passage of time and after few collisions, the molecule shows a non-steady rotational motion associated with a change in the orientation of the molecule.

25

In order to be able to quantify the frequency of molecular rotational diffusion which dominates the relaxation process, another function called the spectral density $j(\omega)$ is defined as the Fourier transform of the correlation function $G(\tau)$ (equation 2.23)

$$j(\omega) = 2 \int_0^\infty G(\tau) \exp(-i\omega\tau) = \overline{B_{loc}^2(t)} \frac{2\tau_c}{1 + (\omega\tau_c)^2}. \tag{2.24}$$

Based on equation 2.24, we define the normalized spectral density function at the Larmor frequency,: $J(\omega_0) = \tau_c/(1 + (\omega_o\tau_c)^2)$. $J(\omega_o)$ is maximum at $\tau_c = 1/\omega_o$. Local fields are most effective at causing relaxation if they are oscillating at frequency close to the Larmor frequency. A maximum in the value of $J(\omega_0)$ thus results in a maximum in the relaxation rate as well.

2.1.2.4 Direct Dipole-Dipole Coupling

For spin-1/2 nuclei, the dominant relaxation mechanism is dipole-dipole coupling.[2] The nuclear spin has a magnetic dipole moment which creates a local magnetic field that directly affects another nearby nuclear spin. The dipole-dipole interaction U^{DD} mainly depends on the distance r between the two nuclear spins and the angle θ between the vector joining the two nuclear spins and the external uniform magnetic field B_o.[2]

$$U^{DD} \propto \frac{(3\cos^2\theta - 1)}{r^3} \tag{2.25}$$

According to this relaxation mechanism the characteristic time T_1 (or the associated relaxation rate $1/T_1$) associated with the relaxation process of the longitudinal magnetization is given by[2]

$$\frac{1}{T_1} = \frac{3}{10}b^2(J(\omega_o) + 4J(2\omega_o)) \tag{2.26}$$

while the characteristic time T_2 (or the associated relaxation rate $1/T_2$) associated with the relaxation process of the transverse magnetization is given by:[2]

$$\frac{1}{T_2} = \frac{3}{20}b^2(3J(0) + 5J(\omega_o) + 2J(2\omega_o)) \tag{2.27}$$

In equations 2.26 and 2.27, $J(\omega_o)$ is the normalized spectral density defined in equation 2.24, and $b = (-\mu_o \hbar \gamma^2)/(4\pi r^3)$. For proton NMR with r=5 Å and $\gamma = 2.674 \times 10^8$ rad/s.T, the typical value of $b^2 \approx 2 \times 10^4$ s^{-2}. One can get an estimate of correlation time that is independent of b^2 by calculating the ratio of T_1/T_2, which is independent of b^2.

In our study, the relaxation measurements for T_1 and T_2 were performed for the polymer species in a polymer (polyethylene oxide)-surfactant (sodium dodecyl sulfate) system (chapter 4), the surfactant species in a wormlike micellar system (chapter 5, lysozyme in lysozyme-buffer system (chapter 6), and the peptide and surfactant species in an antimicrobial peptide-surfactant (sodium dodecyl sulfate) system (chapter 7).

2.1.2.5 Two-Step Relaxation

We have mentioned in previous sections that the fluctuations in the local magnetic fields at the nuclear spin sites, which are created from direct dipole-dipole interactions, give rise to the dominant relaxation mechanism in spin-1/2 nuclei systems.

In a solution which includes surfactant aggregates or polymer/surfactant complexes, the mechanism of relaxation is explained according to the two-step relaxation model.[4-6] According to this model, the fluctuations in the local magnetic fields at nuclear spin sites arise from vibrational motions in a rapid motion regime on the 10^{-12} s time scale, of hydrocarbon chains and torsional motion of molecules in the hydrophobic core of a micelle or aggregate, and a slow motion regime in the 10^{-9}s time scale arising from the tumbling motion of a micelle or aggregate.[7] Based on this model, the dependence of the spin-lattice relaxation rate $1/T_1$ on the normalized spectral density $J(\omega)$ which is shown in equation 2.26, is modified to include the contribution of the normalized spectral densities from both the fast motion regime $J_{fast}(\omega)$ and the slow motion regime $J_{slow}(\omega)$,

$$J(\omega) = aJ_{slow}(\omega) + (1-a)J_{fast}(\omega) \qquad (2.28)$$

where a and (1-a) are the fractions that quantify the relative contribution of slow and fast mo-

27

tions respectively. In such circumstances, extracting a single rotational correlation time from the relaxation measurements is not usually feasible.

2.1.3 Coherence Order and Phase Cycling

The coherence order is a number that identifies the new phase shift of an operator S that experiences an evolution (rotation) by an angle Φ around the z-axis. Therefore, the coherence order is a mathematical tool that is used to describe what happens to an operator (particular state) that undergoes a z-rotation through an angle Φ.[1] Mathematically, the coherence order is defined by the symbol p, while the z-rotation through angle Φ of an operator $\hat{S}$ is given as: $\hat{S}^p \xrightarrow{\Phi \hat{I}_z} \exp(-i\, p\, \Phi)\, \hat{S}^p$.

As an example, the raising operator is a combination of two operators $\hat{I}_x$ and $\hat{I}_y$, so $\hat{I}_+ = \hat{I}_x + i\, \hat{I}_y$. If the raising operator goes through a z-rotation by angle Φ, then as a result: $\hat{I}_+ \xrightarrow{\Phi \hat{I}_z} \exp(-i\, \Phi)\, \hat{I}_+$. This indicates that the operator acquires a phase of $-\Phi$ and has +1 coherence order. Similarly, $\hat{I}_-$ has -1 coherence order, while $\hat{I}_z$ has zero coherence order. Also, this formalism is used in section 2.1.5.2 to determine the evolution (equation 2.30) of the sample magnetization during the spin echo pulse sequence (figure 2.8).[1]

Consider a particular state, an operator that experiences a change in the coherence order from p_1 to p_2 due to the application of an RF-pulse that has $\Delta\Phi$ phase shift. The phase shift acquired by the coherence due to this process is $-\Delta\Phi \times \Delta p$ where $\Delta p = p_2 - p_1$ is called the coherence pathway (CPW). Therefore, in order to select a particular pathway in an NMR experiment, the phase shift of the receiver coil must be tuned to match the phase shift acquired by the coherence pathway.[1]

As an example of this, if we assume that the phase shift of an RF-pulse changes in four steps as $0 \rightarrow (\pi/2) \rightarrow 2\,(\pi/2) \rightarrow 3\,(\pi/2)$ (in more geometric notation, this is written as $x \rightarrow y \rightarrow -x \rightarrow -y$). Then the evolution in the phase shift acquired by a coherence pathway Δp due to an application of the RF-pulse is given as: $0 \rightarrow -(\pi/2) \times \Delta p \rightarrow -2\,(\pi/2)\,\Delta p \rightarrow -3\,(\pi/2)\,\Delta p$. Therefore, in order to select this pathway, the phase shift of the receiver coil Φ_r must be tuned

28

to match the acquired phase shift values of the coherence during the evolution process. If the evolution of the phase shift matches the receiver phase in each step, then the signals in each step will co-add. In order to reject a particular pathway, one must have cancellation, for example, between pairs of steps. This process is called phase cycling. The phase cycles are presented in the captions for the different NMR techniques in section 2.1.5.
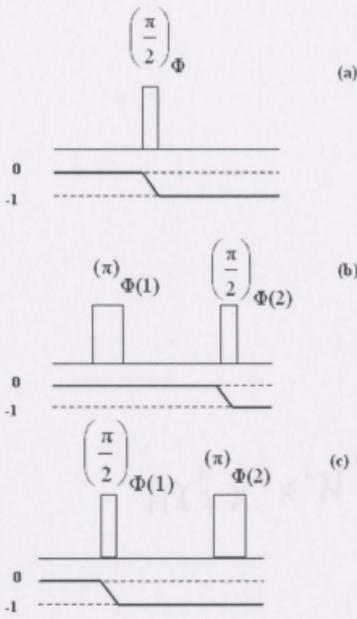
Figure 2.2: Coherence pathway of a) a one dimensional NMR b) an inversion recovery and c) a spin echo pulse sequence.

Figure 2.2 shows the coherence pathway of a one dimensional NMR (often called the zg or "zero go"), an inversion recovery, and a spin echo pulse sequence respectively. The phase cycle (table 2.1) of a one dimensional pulse sequence of the coherence pathway Δp=-1 is Φ=x,-x,-x,x,y,-

y,-y,y, Φ(receiver)=x,-x,-x,x,y,-y,-y,y. This phase cycle rejects other coherence pathways such as $\Delta p = +2, -2$, and 0.

Consider table 2.1 for an example of phase cycling that selects the $\Delta p = -1$ coherence transfer pathway. Comparison of column 4 (for $\Delta p = -1$ pathway) with column 7 shows that each step co-adds, while comparison of column 6 (for $\Delta p = -2$ pathway) with column 7 shows that alternate steps (e.g., 1 and 2) will have exactly opposite sign and give zero signal when added. The first 4 steps of the 8-step phase cycle in table 2.1 are identical to the last 4 steps. The 8-step (instead of 4-step) phase cycle is used to average over possible in-plane (x-y) asymmetries in the receiver hardware.

Table 2.1: Phase cycling that selects for the coherence pathway with $\Delta p = -1$.

1	2	3	4	5	6	7
step	$\Delta\Phi$	$-\Delta\Phi \times \Delta p$	equiv($-\Delta\Phi \times \Delta p$)	$-\Delta\Phi \times \Delta p$	equiv($-\Delta\Phi \times \Delta p$)	$\Phi_{receiver}$
		$\Delta p = -1$	$\Delta p = -1$	$\Delta p = -2$	$\Delta p = -2$	
1	0	0	0	0	0	$0 \equiv x$
2	$2\pi/2$	$2\pi/2$	$2\pi/2$	$4\pi/2$	0	$2\pi/2 \equiv -x$
3	$2\pi/2$	$2\pi/2$	$2\pi/2$	$4\pi/2$	0	$2\pi/2 \equiv -x$
4	0	0	0	0	0	$0 \equiv x$
5	$\pi/2$	$\pi/2$	$\pi/2$	$2\pi/2$	$2\pi/2$	$\pi/2 \equiv y$
6	$3\pi/2$	$3\pi/2$	$3\pi/2$	$6\pi/2$	$2\pi/2$	$3\pi/2 \equiv -y$
7	$3\pi/2$	$3\pi/2$	$3\pi/2$	$6\pi/2$	$2\pi/2$	$3\pi/2 \equiv -y$
8	$\pi/2$	$\pi/2$	$\pi/2$	$2\pi/2$	$2\pi/2$	$\pi/2 \equiv y$

2.1.4 NMR Instrumentation

In this section, a brief outline of NMR instrumentation is provided. The NMR spectrometer consists of several elements.[1,2,8] A few important elements are discussed below.

1. A primary component in NMR is the superconducting magnet. The superconducting magnet consists of a solenoid of wire (i.e. coil) made of a material that is superconducting (e.g a niobium and tin alloy) at liquid helium temperature so that a current flows without any resistance. This cable of wire is shielded by a cylindrical tank of liquid helium at a temperature 4 K which itself is shielded by another cylindrical tank of liquid nitrogen at 77 K. The cylindrical tank of liquid nitrogen is also surrounded by an evacuated cylindrical tank to reduce heat transfer and heat exchange. Other coils called shimming coils are located at the bottom of the magnet and they are used to produce a homogeneous magnetic field at the sample location.

2. The probe is the interface between the NMR spectrometer and the sample. It is used to produce radio-frequency excitations within the sample and to receive the sample signal as well. So the probe includes two main electronic parts of the NMR spectrometer: the transmitter circuit and the receiver circuit. Also the probe holds a coil (figure 2.3) wrapped close to the sample to enhance the sensitivity of the receiving and excitation process, which is connected to a tuning and matching capacitors. In the tuning process, we change the capacitance of the tuning capacitor which causes a change in the resonance frequency of the tuning circuit (i.e. coil-tuning capacitor circuit) to match synthesizer frequency. The matching capacitor allows you to match the impedance of the resonant circuit to the impedance of the transmission line that it is attached to. In addition, the probe includes field gradient coils that are used to create an inhomogeneous magnetic field (field gradient) in order to measure the diffusion coefficient values of different molecular species in a sample. The field gradients can be along one axis as in the diffusion probe (Diff 30, 1-axis gradient) or along three axes as in the Micro-5 imaging (3-axis gradient) probe.

3. The transmitter circuit (figure 2.4) is mainly used to produce the radio-frequency (RF) pulse. The main part of this circuit is the synthesizer which is used to produce low power level
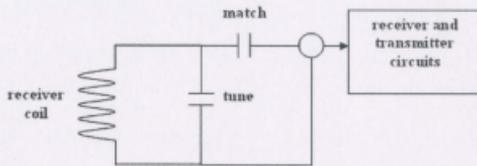
Figure 2.3: Schematic diagram of the receiver coil, the tunning capacitor, and the matching capacitor.

(few mW) RF-pulses. In order to control the time of the pulse, the synthesizer is connected to a gate, attenuator and high-power amplifier, all of which are computer controlled. The attenuator is used to reduce the power level to create soft RF pulses and the high-power amplifier is used to to increase the power level for the RF pulse to create hard pulses.
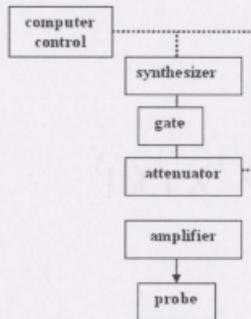
Figure 2.4: Schematic diagram of the transmitter circuit.

In addition, the transmitter circuit can change the orientation of the RF-pulse in the xy-plane by changing the phase shift of the magnetic field B_{RF} associated with the RF-pulse. In the laboratory frame, we know from equation 2.5, the RF pulse is given in terms of the

resonance component of the RF-pulse $\overrightarrow{B_{RF}} \approx \overrightarrow{B_{RF}^{Res}} = \frac{B_{RF}}{2}\left(\cos(\omega_{RF}t + \phi_p)\hat{i} + \sin(\omega_{RF}t + \phi_p)\hat{j}\right)$.

Having $\phi_p = 0$, in the rotating frame $\overrightarrow{B_{RF}}$ acts as a stationary magnetic field which is oriented along the x-axis (i.e. at $t = 0$, $\overrightarrow{B_{RF}} \approx \frac{B_{RF}}{2}\hat{i}$) since the xy-plane rotates at the same frequency as the frequency of RF-pulse. Changing the phase shift of the RF-pulse in the laboratory frame from zero to $\pi/2$, $\overrightarrow{B_{RF}}$ acts as a stationary magnetic field which is oriented along the y-axis in the rotating frame (i.e. at $t = 0$, $\overrightarrow{B_{RF}} \approx \frac{B_{RF}}{2}\hat{j}$).

4. The receiver coil is used to detect small amplitude sample magnetization (i.e. the NMR signal) which is amplified using a high performance pre-amplifier (HPPR). The HPPR is connected to the bottom of the probe by a short cable and it is located close to the bottom of the probe to minimize any attenuation or loss in the signal due to the transmission through the cable. The receiver and the transmitter circuits are connected to a diode called a duplexer. It is used to switch off and on the receiver and the transmitter circuits.

5. A variable temperature unit is used to increase, decrease, and control the temperature of the sample.

6. The `locking" system is responsible for preserving the stability of the magnetic field during the experiment. For example, a typical experiment in this work will involve detectable spin-1/2 protons in a deuterated solvent (so it includes many ^2H nuclei as well). The ratio of proton to deuterium Larmor frequencies is given by $\frac{\gamma^H}{\gamma^{2H}} \approx 6.5$. The locking system detects the signal of the deuterium nuclei in deuterated solvent. If the Larmor frequency of deuterium signal changes, (e.g. due to a drift in the B_o) a special current carrying coil at the base of the magnet creates a current to adjust the value of the external magnetic field B_o. Since one should average over many scans in NMR, it is the best that all scans to be carried out at the same Larmor frequency.

7. The quadrature receiver (figure 2.5) is used to detect the x and y-components of the trans-

verse magnetization. The x and y-components of the transverse magnetization are proportional to the x and y-components of the time domain NMR signal that is presented in a complex form: $S(t) = S_x + i S_y$. In order to detect both components of the time domain signal separately, the NMR signal with frequency ω_0 is manipulated in a mixer by multiplying it with the signal from the receiver reference with a frequency ω_{ref}. The receiver reference signal is split into two different paths, at two separate mixers, that have $\pi/2$ difference in the phase shift. The output signals (manipulated NMR signals) from the mixers are a combination of two signals at frequencies $\omega_0 + \omega_{ref}$ and $\omega_0 - \omega_{ref}$. These output signals pass through low-pass filters which retains the low-frequency ($\omega_0 - \omega_{ref}$) components that represent the x and y-components of the NMR signal. Despite the fact that both the x and y-components of the transverse magnetization are detected, p=-1 is the only observable coherence after the above mentioned manipulating process for the signal. The low-frequency components of the NMR signal can be received by the analogue-to-digital converter (ADC) that converts the analogue NMR signal to a digital signal which can be stored in the computer.
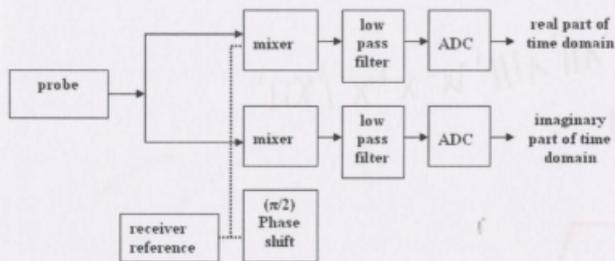
Figure 2.5: Schematic diagram of the quadrature receiver circuit.

In my work, one dimensional spectra, relaxation measurements, and diffusion measurements were obtained on a Bruker Avance II spectrometer with either a diffusion probe (Diff30, 1-axis

34

gradient) with maximum field gradient (1800 G/cm), a Micro-5 imaging (3-axis gradient) with maximum field gradient (200 G/cm), or a high resolution (TXI) probe with maximum field gradient (50 G/cm). In pulsed-field gradient NMR experiments (section 2.1.5.3), it is necessary to create pulsed gradients in the static magnetic field. For this 14 T spectrometer, the proton ^{1}H resonance frequency $\approx$ 600 MHz and the deuterium ^{2}H resonance frequency $\approx$ 92 MHz. Note that the gradient strengths in the Diff30 probe and the Micro-5 imaging probe are much higher than those in a standard liquid probes such as Bruker high resolution (TXI) probe.

2.1.5 NMR Techniques

Three main techniques have been used to measure three physical quantities: the longitudinal relaxation time T_1, the transverse relaxation time T_2, and diffusion coefficient D of different species in the solution.

2.1.5.1 Inversion Recovery Technique

This technique is used to measure the longitudinal relaxation time T_1 associated with different chemical groups inside a sample. The pulse sequence, figure 2.6, includes two successive pulses, $(\pi)_x$ and $(\frac{\pi}{2})_x$ pulses with a delay time τ between both pulses.[9]

The first $(\pi)_x$ inverts the magnetization of the sample, which is initially at equilibrium, from the +z-axis to the -z-axis. As soon as $(\pi)_x$ is turned off, the magnetization vector starts to relax back to its previous orientation along the z-axis during the delay time. No signal can be detected by the NMR device because there is no available magnetization component in the xy-plane. Then, the sample is exposed to a $(\frac{\pi}{2})_x$ pulse which is responsible for creating a transverse magnetization in the xy-plane which can be detected by the receiver coil and recorded as a peak with specific intensity and polarity.

The pulse sequence is repeated at different values of delay time τ. The intensity of the signal
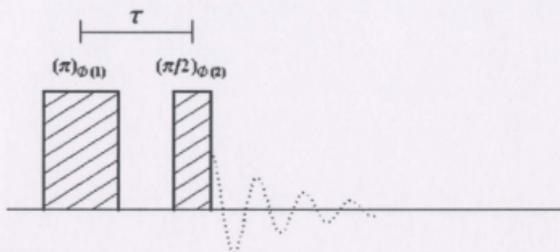
Figure 2.6: Inversion recovery pulse sequence. The phase cycle is: $\Phi(1)$= x, -x, x, -x, x, -x, x, -x; $\Phi(2)$= x, x, -x, -x, y, y, -y, -y; $\Phi(\text{receiver})$= x, x, -x, -x, y, y, -y, -y. $\Phi(1)$ and $\Phi(2)$ are the phase shifts of the first and second pulses in the pulse sequence respectively.

measured is proportional to the magnitude of the sample longitudinal magnetization $M_z(\tau)$ in the time τ after the $(\pi)_x$ pulse,[9]

$$M_z(\tau) = M_o\left(1 - 2\exp\left(\frac{-\tau}{T_1}\right)\right) \qquad (2.29)$$

where M_o is the magnitude of sample magnetization at equilibrium and T_1 is the longitudinal relaxation time. Based on equation 2.29, turning on the $(\pi/2)_x$ pulse immediately after turning off the $(\pi)_x$ pulse (i.e. $\tau = 0$) would give magnetization amplitude with a negative polarity $-M_o$ that is detected by the NMR receiver coil. On the other hand, turning on the $(\pi/2)_x$ pulse at large value of τ (i.e. $\tau = \infty$) after turning off the $(\pi)_x$ would give magnetization amplitude with a positive polarity $+M_o$.

Figure 2.7a shows the variation in the intensity (i.e. the longitudinal magnetization $M_z(\tau)$) of the PEO peak as a function of delay time τ, while figure 2.7b shows the variation in the intensity (i.e. the transverse magnetization $M_y(\tau)$) of the PEO peak as a function of delay time for PEO(0.5% w/v)/SDS(20 mM)/D_2O. According to equation 2.29, the longitudinal relaxation time T_1 is defined as the value of delay time at which the longitudinal sample magnetization recovers to

36
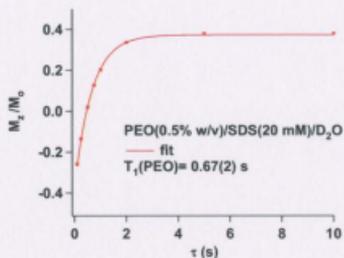
(a)
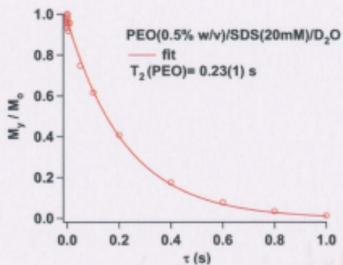
(b)

Figure 2.7: (a) The variation in the intensity (i.e. the longitudinal magnetization $M_z(\tau)$) of the PEO peak versus a delay time τ and (b) the variation in the intensity (i.e. the transverse magnetization $M_y(\tau)$) of the PEO peak versus a delay time for PEO(0.5% w/v) /SDS(20 mM)/D$_2$O sample at T=298 K

≈ 0.26 of its equilibrium magnetization value M_o.

2.1.5.2 Spin Echo Technique

The spin echo is very useful. It is used to measure the transverse relaxation time T_2.[9] A modified spin echo is also used to measure translational diffusion (section 2.1.5.3). The pulse sequence (figure 2.8) includes two successive pulses, $(\frac{\pi}{2})_x$ and $(\pi)_x$ pulse with a delay time τ between these two pulses and same period of delay time between $(\pi)_x$ and the signal acquisition.
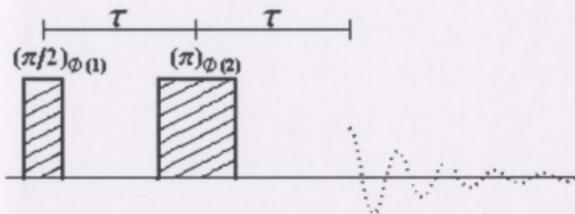
Figure 2.8: Spin echo pulse sequence. The phase cycle is: $\Phi(1)=$ x, x, -x, -x, y, y, -y, -y; $\Phi(2)=$ y, -y, y, -y, x, -x, x, -x; $\Phi(\text{receiver})=$ x, x, -x, -x, y, y, -y, -y. $\Phi(1)$ and $\Phi(2)$ are the phase shifts of the first and second pulses in the pulse sequence respectively.

The evolution of the sample magnetization (neglecting relaxation and assuming no field inhomogeneity) during the spin echo pulse sequence (e.g figure 2.8) is given as follows:[1]

$$\hat{I}_z \xrightarrow{(\pi/2)\hat{I}_x} -\hat{I}_y \xrightarrow{\Omega\tau\hat{I}_z} -\cos(\Omega\tau)\hat{I}_y + \sin(\Omega\tau)\hat{I}_x \xrightarrow{(\pi)\hat{I}_x} -\cos(\Omega\tau)\hat{I}_y - \sin(\Omega\tau)\hat{I}_x \xrightarrow{\Omega\tau\hat{I}_z} -\hat{I}_y \quad (2.30)$$

As shown in equation 2.30, the first $(\frac{\pi}{2})_x$ pulse disturbs the equilibrium magnetization and creates a transverse magnetization along the y-axis. After turning off the $(\frac{\pi}{2})_x$ pulse and during the first delay time τ between $(\frac{\pi}{2})_x$ and $(\pi)_x$ pulses, the nuclear spins start precessing slightly at different

frequencies (equation 2.22) such that some nuclear spins precess faster than the Larmor frequency while some others precess slower than the Larmor frequency (i.e. with values of Ω greater and less than zero in the rotating frame reference).

In discussing transverse relaxation, we introduced the idea that the transverse magnetization decays to zero due to loss in synchronization (secular contribution) of precessional motions of nuclei due to local field variations (caused by molecular motions). Such a decay in transverse magnetization is irreversible. However in the presence of non-random local field variations (such as a stray field gradient or an applied field gradient) the loss in transverse magnetization is at least partially reversible. The next $(\pi)_x$ inverts the orientation of individual nuclear spins to the opposite side in the xy plane. At the end of a second evolution period time τ, the dephasing in the transverse component of the sample magnetization due to the existence of inhomogeneous magnetic field is exactly reversed and results in a ``spin echo''.

The pulse sequence is repeated at different values of delay time τ in order to detect the time dependence of peaks intensities which is proportional to sample transverse magnetization $M_y(\tau)$:[9]

$$M_y(\tau) = M_y(0) \exp\left(\frac{-2\tau}{T_2}\right) \tag{2.31}$$

where $M_y(0)$ is the magnitude of the transverse magnetization right after turning off $(\frac{\pi}{2})_x$ pulse.

According to equation 2.31, the transverse relaxation time T_2 is defined as the value of delay time at which the transverse component of sample magnetization decays to ≈ 0.37 of its maximum value $M_y(0)$.

In our experiments, separate experiments were carried out at different τ values. In this ``quasi-two dimensional'' experiment, the second dimension is τ. T_2 can also be measured in a single experiment with multiple π pulses and an acquire after each π pulse, this is known as the Carr-Purcell-Meiboom-Gill (CPMG) pulse sequence.

2.1.5.3 Pulsed-Field Gradient (PFG) Spin Echo

Translational self diffusion of a molecule in a liquid is a random walk in a sequence of steps or hops of a molecule in the absence of concentration gradient. These molecular steps are attributed to the random thermal collisions with other molecules in the liquid such that over a sequence of molecular steps the net force impacting the molecule is zero due to symmetry. Yet at each time step collisions on an individual molecule are asymmetric.[10] This drives the molecule to move randomly under the influence of fluctuating forces.

There are two widely used techniques that employ pulsed magnetic field gradients. Magnetic resonance imaging (MRI) has been utilized vastly as a nondestructive and direct technique to study the structure of materials in industrial and medical fields, and diffusometry has been used as an effective tool to investigate the dynamics and analyze the diffusion of water molecules in porous materials. Diffusometry represents an indirect technique that is used to explore the effect of the walls of a restricted geometry (pores) on the flow and dynamics of water molecules. This provides quantitative information about the pore-size.[11]

Pulsed-field gradient (PFG) nuclear magnetic resonance is one of the techniques used to measure the translational diffusion coefficients of different molecular species inside a liquid. The sample is exposed to both strong uniform magnetic field B_o along the z-direction and a pulsed field gradient $g_z = dB_o/dz$ along the direction of the uniform magnetic field which modifies the precession frequency ω_i of a nuclear spin[12]

$$\omega_i = \gamma B_o + \gamma \vec{g}.\vec{r} = \gamma B_o + \gamma g_z z_i(t) \qquad (2.32)$$

where $z_i(t)$ is the position of a nuclear spin i at time t and $g_z = dB_o/dz$.

As in the spin-echo pulse sequence, a $(\frac{\pi}{2})_x$ pulse rotates the sample magnetization from the z-axis to the xy-plane.[12] At the end of the first delay time period, the nuclear spin possesses a phase shift $(\phi_i(\tau))_1$ due to the application of a field gradient pulse of magnitude g and duration δ at time t_1. At the end of the first delay time period, a $(\pi)_y$ pulse is applied which inverts the orientation

40
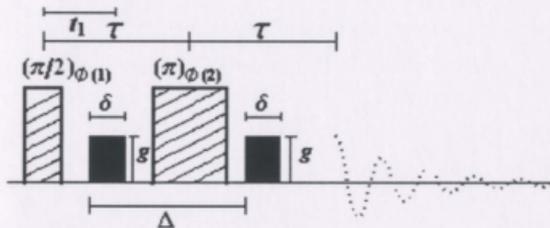
Figure 2.9: Hahn spin echo pulse sequence. The hashed pulses are radio-frequency electromag-netic pulses. The solid black pulses are magnetic field gradient pulses. The phase cycling is: $\Phi(1)=$ x, x, -x, -x, y, y, -y, -y; $\Phi(2)=$ x, y, x, y, -y, -x, -y, -x; Φ(receiver)= x, -x, -x, x, y, -y, -y, y. $\Phi(1)$ and $\Phi(2)$ are the phase shifts of the first and second RF-pulses in the pulse sequence, respectively.

of individual nuclear spins to the opposite side of xy plane (i.e. rephasing the dispersion of the individual nuclear spins which is attributed to nonhomogeneity in the applied uniform magnetic field B_o). During the second delay time period at time $t_1 + \Delta$ another field gradient pulse with the same duration and magnitude is applied. Assuming that a nuclear spin moves from one position to a new position along the z-axis during the time period Δ, then at the end of the PFG sequence the nuclear spin posses a total phase shift $\phi_i(2\tau)$[12]

$$
\begin{aligned}
\phi_i(2\tau) &= \left\{ \gamma B_o \tau + \gamma g \int_{t_1}^{t_1+\delta} z_i(t)dt \right\} - \left\{ \gamma B_o \tau + \gamma g \int_{t_1+\Delta}^{t_1+\Delta+\delta} z_i(t')dt' \right\} \\
&= \gamma g \left\{ \int_{t_1}^{t_1+\delta} z_i(t)dt - \int_{t_1+\Delta}^{t_1+\Delta+\delta} z_i(t')dt' \right\}
\end{aligned}
\tag{2.33}
$$

The first and the second integral terms in equation 2.33 represent the phase shift of the nuclear spin $(\phi_i(\tau))_1$ and $(\phi_i(\tau))_2$ at the end of the first delay time and at the end of the second delay time periods, respectively. In the absence of nuclear spin diffusion (i.e. when the net displacement of

nuclear spin along the direction of field gradient pulse is equal to zero) the total phase shift $\phi_i(2\tau)$ is equal to zero.

The sample contains a large number of nuclear spins which have different starting and finishing positions and so they possess different values of phase shifts. The resulting signal attenuation at the end of the pulse sequence is $S(2\tau)$:[12]

$$S(2\tau) = S(2\tau)_{g=0} \left\{ \int_{-\infty}^{\infty} P(\phi, 2\tau) \exp(i\phi) d\phi \right\} \qquad (2.34)$$

where $S(2\tau)_{g=0}$ is the signal intensity in the absence of field gradient pulses, and $P(\phi, 2\tau)$ is the phase distribution function, which is a Gaussian function with respect to ϕ because the molecular self-diffusion is a random varying quantity,

$$P(\phi, 2\tau) = \frac{1}{2\pi \left\langle (\phi(2\tau))^2 \right\rangle} \exp \left(\frac{-(\phi(2\tau))^2}{2 \left\langle (\phi(2\tau))^2 \right\rangle} \right) \qquad (2.35)$$

Therefore, equation 2.34 can be written in terms of $P(\phi, 2\tau)$

$$S(2\tau) = S(2\tau)_{g=0} \exp \left(-\frac{\left\langle (\phi(2\tau))^2 \right\rangle}{2} \right) \qquad (2.36)$$

In order to be able to derive the signal attenuation function $S(2\tau)$ in equation 2.36, we need to evaluate $\left\langle (\phi(2\tau))^2 \right\rangle$. Let us assume (following Callaghan[13]) a one dimensional displacement Z of a nuclear spin during the time period of a field gradient includes consecutive steps. The average displacement between any two successive steps is λ and the average time is τ_s. Based on that, the average displacement of a nuclear spin after n hops is given as

$$Z(t) = Z(n\tau_s) = \sum_{i=1}^{n} \lambda a_i \qquad (2.37)$$

where $a_i = +1$ or -1 indicates the diffusion of a nuclear spin along or in the opposite direction of the field gradient respectively. Using equation 2.37, we evaluate the one-dimensional mean square displacement

$$\left\langle (Z(t))^2 \right\rangle = \left\langle (Z(n\tau_s)^2) \right\rangle = n\lambda^2 = 2Dt \qquad (2.38)$$

42

where D is the self-diffusion of a nuclear spin.

Using equation 2.38, one can show that the mean-square value of the accumulative phase shift $\langle(\phi(2\tau))^2\rangle$ in the pulsed-field gradient spin echo is given as follows

$$\langle(\phi(2\tau))^2\rangle = \gamma^2 g^2 \frac{\lambda^2}{\tau_s}\delta^2\left(\Delta - \frac{\delta}{3}\right) = 2\gamma^2 g^2 D\delta^2\left(\Delta - \frac{\delta}{3}\right) \qquad (2.39)$$

By substituting equation 2.39 into equation 2.36, we evaluate the attenuation in the signal intensity

$$
\begin{aligned}
S(2\tau) &= S(2\tau)_{g=0}\exp\left(-\gamma^2 g^2 D\delta^2(\Delta - \frac{\delta}{3})\right) \\
&= S(0)\exp\left(\frac{-2\tau}{T_2}\right)\exp\left(-\gamma^2 g^2 D\delta^2(\Delta - \frac{\delta}{3})\right) \qquad (2.40)
\end{aligned}
$$

where $S(0)$ is the intensity of the signal in the absence of attenuation due to transverse relaxation and due to diffusion of nuclear spins.

2.1.5.4 Pulsed Field Gradient Stimulated Echo (PFG-STE)

This pulse sequence is preferable to measure the diffusion coefficients of molecules which have long longitudinal relaxation time T_1 compared to their transverse relaxation time T_2 ;$T_1 \gg T_2$.[14]

The pulse sequence (figure 2.10) includes three successive $(\frac{\pi}{2})_x$ pulses, delay time τ_1 between the first two $(\frac{\pi}{2})_x$ pulses and same period of delay between the third $(\frac{\pi}{2})_x$ pulse and the signal acquisition, delay time τ_2 between the second and third $(\frac{\pi}{2})_x$ pulses and two field gradient pulses each with duration δ and magnitude g inserted separately in the first and last τ_1 periods.[14]

The signal is subjected to attenuation due to diffusion, T_2 relaxation during τ_1 periods and T_1 relaxation during τ_2 period:[14]

$$S(g) = \frac{S(0)}{2}\exp\left(\frac{-2\tau_1}{T_2}\right)\exp\left(\frac{-\tau_2}{T_1}\right)\exp\left(-\gamma^2 g^2 D\delta^2(\Delta - \frac{\delta}{3})\right) \qquad (2.41)$$

The main advantages of using PFG-STE are summarized as follows:[14]

1. The longer part of diffusion time Δ is included in τ_2 period during which the magnetization is subjected to the T_1 relaxation with longitudinal relaxation time T_1 which is commonly
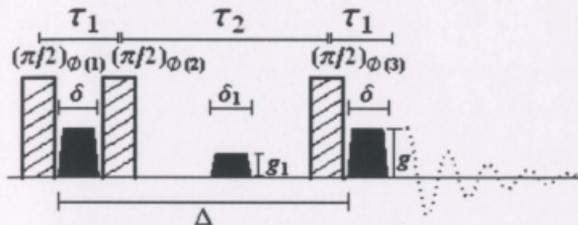
Figure 2.10: Pulsed field gradient stimulated echo pulse sequence. The phase cycle is: $\Phi(1)=$ x, x, x, x, -x, -x, -x, -x, y, y, y, y, -y, -y, -y, -y; $\Phi(2)=$ y, -y, x, -x; $\Phi(3)=$ y, -y, x, -x; $\Phi(\text{receiver})=$ x, x, -x, -x, -x, -x, x, x, -y, -y, y, y, y, y, -y, -y. $\Phi(1)$, $\Phi(2)$, and $\Phi(3)$ are the phase shifts of the first, second, and third RF-pulses in the pulse sequence respectively.

longer than T_2 for macromolecules in solution. So there is more opportunity to increase the value of Δ in order to measure more accurately the diffusion coefficient of macromolecules.

2. The attenuation due to T_2 relaxation in PFG-STE is smaller than the attenuation due to T_2 relaxation in Hahn-spin echo PFG since the period during which the magnetization is subjected to T_2 relaxation in PFG-STE is smaller than that in Hahn-spin echo PFG.

3. We are able to increase τ_1 periods in order to minimize the effects of eddy currents which are associated with the field gradient pulses.

2.2 Rheology

Rheology is a branch of science which is directed at investigating the mechanical response of matter to an external stress or strain. Matter is classified based on its mechanical response into simple liquids, simple solids, and complex fluids. While simple fluids exhibits viscous flow as a me-

chanical response to an applied stress and simple solids shows elastic instantaneous deformation, complex fluids have been found to exhibit remarkable viscoelastic behavior that combines both viscous and elastic response intermediate between simple liquids and simple solids.[15]

Viscoelastic behavior is seen in many materials such as polymer solutions, gels, micellar solutions, and colloidal suspensions used in cosmetics, detergents, inks, lubricants, paints, food, and pharmaceuticals. Moreover, complex fluids include biomaterials such as blood as well as personal care products used in daily life such as shampoo and toothpaste.

Silly putty is a good example of a complex fluid.[10] It exhibits viscoelastic behavior at different time scales. If silly putty experiences a stress on a slow time scale, it flows in a similar way as simple liquids, while if it experiences a stress on a short time scale, by rolling it up into a ball and drop it on the ground, it behaves like a simple elastic solid. In rheology, the scaling parameter that separates the liquid-like behavior from the solid-like behavior of viscoelastic materials, is called the Deborah number D_e. It is the ratio of the material relaxation time τ, that separates the liquid-like behavior from the solid-like behavior, to the time T of the applied stress or strain, $D_e = \tau/T$. Therefore, high Deborah number indicates solid-like behavior while low Deborah number indicates liquid-like behavior.[15]

2.2.1 Rheometer

A rheometer is a laboratory device which is used to study the mechanical response of fluids to a stress or strain.[16] Our rheological measurements have been carried out on an Anton Paar Physica MCR 301 rheometer, where the cone-plate measuring system (figure 2.11) has been used to extract the stress relaxation measurements, flow curves, and oscillatory shear curves (i.e. dynamic curves). The cone-plate geometry used in this Thesis is of R = 50 mm diameter and θ = 0.5° cone angle. The main advantage of using cone-plate geometry is that we only need to use a small sample amount in order to run our experiments. Also, the shear rate is homogeneous and it remains

constant throughout the sample.[16]

For this kind of rheometer, the cone is rotating with respect to a stationary plate. In a stress driven experiment, applying a torque M generates an angular displacement Φ that can be measured where $\dot{\gamma} = \frac{d\Phi}{dt\theta}$, while in a strain driven experiment applying an angular displacement Φ generates a torque M that can be measured where $\sigma = \frac{3M}{2\pi R^3}$. The rotational motion of the cone is resisted by a ``torsion bar'' which represents an elastic piece of metal that stores more mechanical energy as it is twisted. Therefore, the degree of torsion is an indicator for the shear stress, while the rotational speed of the cone and its dimension (i.e. the gap width) is an indicator for the shear rate $\dot{\gamma}$.[17]
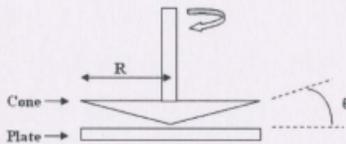
Figure 2.11: Cone-and-plate measuring system

2.2.2 Flow Curves

The viscous flow of simple liquids is characterized by the viscosity η while the elastic response of simple solids is characterized by the shear modulus G which reflects the energy stored.[10,18] These two parameters can be measured in a complex fluid by either applying steady or oscillatory stress or strain using the rheometer. Applying a stress on a simple liquid will produce a time-dependent strain which is equivalent to a constant value of strain rate in Newtonian liquids. Therefore, in

46

Newtonian liquids, the shear stress σ is linearly proportional to the strain rate $\dot{\gamma}$

$$\sigma = \eta\dot{\gamma} \qquad (2.42)$$

such that the liquid viscosity represents the proportionality constant. On the other hand, simple solids response to a constant applied stress σ by producing a shear strain γ which is linearly proportional to the applied stress

$$\sigma = G\gamma, \qquad (2.43)$$

in the case of Hookean solids, such that the shear modulus G represents the linearity constant.

The viscosity of complex fluids is not constant but it is a shear rate-dependent parameter. As an example, the viscosity of paint or yogurt decreases as the shear rate increases.[10,18] Complex fluids that exhibit this behavior are called shear thinning materials. On the other hand, the viscosity of whipped cream increases as the shear rate increases. This is knows as shear thickening. While some complex fluids undergo irreversible deformations under an applied shear stress (large stresses) which is known as plastic behavior, other complex fluids called Bingham fluids require a threshold yield stress in order to flow and exhibit linear shear stress/shear strain relationship. Examples of Bingham fluids are toothpaste, mayonnaise, and mustard.

2.2.3   Oscillatory Shear

Mechanical models are used in order to simplify our understanding of complex fluids viscoelastic behavior.[18] In these models, the viscous behavior is represented by a dashpot that includes a piston inside a cylinder filled with a liquid. A force F on the dashpot causes the piston to move with a speed $V = dX_{pist}/dt$ that is proportional to the applied force ($F = \eta V$). η is the liquid viscosity inside the cylinder and X_{pist} is the piston displacement. This equation is quite similar to that of a Newtonian liquid where the shear stress σ is linearly proportional to the shear strain rate $\dot{\gamma}$ (equation 2.42).

47

On the other hand, the elastic behavior of a complex fluid is represented by spring which has a spring constant G.[18] An applied force F causes a displacement X_{sp} in the spring that is proportional to F ($X_{sp}=F/G$). This equation is analogous to the equation for Hookean solids where the shear stress is linearly proportional to the shear strain γ (equation 2.43).

Figure 2.12: A spring and a dashpot connected in series. Maxwell model.

The Maxwell model is a mechanical model that includes a spring and dashpot connected in series (figure 2.12). If a displacement is imposed on the top end of the system in figure 2.12, this causes stretching of the spring.[18] The piston in the dashpot will be pulled out slowly since the viscous liquid in the cylinder resists the movement. Therefore, the total displacement X of this model is a combination of the displacement in the spring X_{sp} and the displacement in the piston X_{pist}. Based on that,

$$\frac{dX}{dt} = \frac{dX_{sp}}{dt} + \frac{dX_{pist}}{dt} = \frac{\dot{F}}{G} + \frac{F}{\eta}.$$ (2.44)

Equation 2.44 can be written in terms of shear strain rate $\dot{\gamma}$, shear stress σ, and shear stress rate $\dot{\sigma}$

$$\dot{\gamma} = \frac{\dot{\sigma}}{G} + \frac{\sigma}{\eta}.$$ (2.45)

In practice, the mechanical response of viscoelastic fluids to an oscillatory shear strain $\gamma = \gamma_o \sin(\omega t)$ can be explored using a rheometer, where γ_o is the amplitude of the shear strain. If this is substituted in equation 2.45, a first order linear differential equation is obtained. Based on that,

the resulting shear stress

$$\sigma = \gamma_o \left(G^{'} \sin(\omega t) + G^{''} \cos(\omega t) \right) \tag{2.46}$$

includes two components, in phase and out of phase with respect to the applied oscillatory strain. Here $G^{'}$ and $G^{''}$ are called the storage and loss modulus respectively

$$G^{'} = G_o \frac{(\omega \tau)^2}{1 + (\omega \tau)^2} \tag{2.47a}$$

$$G^{''} = G_o \frac{\omega \tau}{1 + (\omega \tau)^2} \tag{2.47b}$$

The storage modulus $G^{'}$ reflects the deformation energy stored in a test sample under an applied stress. As soon as the applied stress is removed, the stored energy is used to reform the structure of the sample partially or completely. On the other hand, the loss modulus $G^{''}$ reflects the deformation energy dissipated to change the structure (flowing of a test sample) of a test sample under the applied stress. A Maxwellian viscoelastic material will thus behave more solid-like at high frequencies ($G^{'} \gg G^{''}$ at high ω) and more liquid-like at low frequencies ($G^{''} \gg G^{'}$ at low ω).

By eliminating $\omega \tau$ from the expressions of the moduli in both equation 2.47a and equation 2.47b, the loss modulus $G^{''}$ can be presented and expressed in terms of the storage modulus $G^{'}$

$$\left(\frac{G^{''}}{G_o} \right)^2 + \left(\frac{G^{'}}{G_o} - \frac{1}{2} \right)^2 = \left(\frac{1}{2} \right)^2. \tag{2.48}$$

Equation 2.48 is valid for complex fluids which exhibit a single value of relaxation time. These fluids are called Maxwellian fluids. Based on equation 2.48, we can see that for Maxwellian fluids the functional behavior of $G^{''}/G_o$ versus $G^{'}/G_o$ (the so called Cole-Cole diagram) exhibits a semicircle of radius (1/2). This Cole-Cole diagram can be used to extract parameters such as the shear modulus (G_o) for a Maxwellian fluid.

49

2.2.4 Stress Relaxation

The stress relaxation measurement is another practical test that can be used to analyze the time-dependent behavior of different materials.[16,19] The tested material experiences a shear strain γ that is held constant for a period of time (a step-strain). The mechanical response of the material is then detected by measuring the shear stress $\sigma(t)$ over the same period of time:

$$\sigma(t) = G(t)\gamma. \qquad (2.49)$$

Different materials exhibit different stress relaxation behavior. As an example, the Hookean solid shows time-independent behavior for the stress relaxation (shows no stress relaxation), the Newtonian liquid shows a quick relaxation that is too short to observe in rheology as soon as the shear strain held constant, and viscoelastic fluids exhibit relaxation over the entire time period in ms-s time scales of the applied strain (figure 2.13).

(a)

(b)
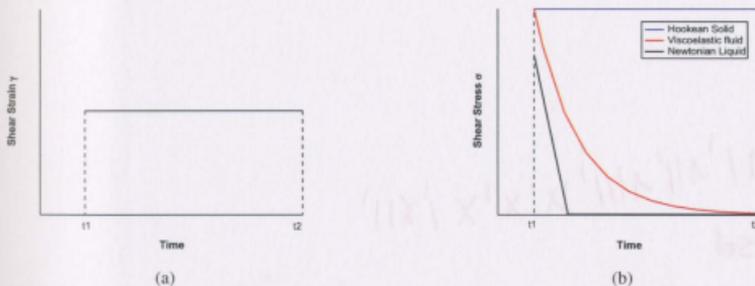
Figure 2.13: (a) An applied shear strain γ (b) the shear stress σ versus time in the time duration t_1 to t_2 for Hookean solid, viscoelastic fluid, and Newtonian liquid.

The stress relaxation function of viscoelastic fluids might be either an exponential decay with a single relaxation time

$$\sigma = \sigma_o \, \exp(-t/\tau) \qquad (2.50)$$

50

or a function with several relaxation times

$$\sigma = \sum_{k=1}^{N} \sigma_k \exp(-t/\tau_k).$$ (2.51)

The wormlike micellar system that has been studied in details in chapter 5 is an example of a viscoelastic fluid that exhibits a stress relaxation function with more than one relaxation time.

Bibliography

[1] James Keeler. *Understanding NMR Spectroscopy*. John Wiley & Sons Ltd, Chichester, 1st edition, 2005.

[2] Malcolm H. Levitt. *Spin Dynamics*. John Wiley & Sons, Chichester, 2nd edition, 2008.

[3] Anatole Abragam. *The Principles of Nuclear Magnetism*. Oxford University Press, New York, 1st edition, 1961.

[4] H. Wennerstrom, B. Lindman, O. Soderman, T. Drakenberg, and J. B. Rosenholm. ^{13}C magnetic relaxation in micellar solutions influence of aggregate motion on TI. *Journal of the American Chemical Society*, 101:6860–6864, 1979.

[5] Josette M. Landry, D. Gerrard Marangoni, Deborah A. Arden, Ian J. MacLennan, and Jan C. T. Kwak. A 1D- and 2D-NMR study of an anionic surfactant/neutral polymer complex. *Journal of Surfactants and Detergents*, 12:155–164, 2009.

[6] Olle Soderman, Peter Stilbs, and William S. Price. NMR studies of surfactants. *Concepts in Magnetic Resonance Part A*, 23A:121–135, 2004.

[7] Sherril D. Christian and John F. Scamehorn. *Solubilization in Surfactant Aggregates*. Marcel Dekker Inc, New York, 1st edition, 1995.

[8] Eamonn Butler. *Avance Beginners Guide*. Bruker Biospin GmbH, Rheinstetten, Germany, 2003.

[9] Metin Balci. *Basic ^1H-^{13}C-NMR Spectroscopy*. Elsevier B.V., Amsterdam, 1st edition, 2005.

[10] Richard. A. L. Jones. *Soft Condensed Matter*. Oxford University Press Inc, New York, 1st edition, 2002.

[11] Beau Webber. NMR looks deep inside nooks and crannies. *Physics*, 93:1, 2012.

[12] William S. Price. Pulsed-field gradient nuclear magnetic resonance as a tool for studying translational diffusion: Part I. basic theory. *Concepts in Magnetic Resonance*, 9:299–336, 1997.

[13] Paul T. Callaghan. *Principles of Nuclear Magnetic Resonance Microscopy*. Clarendon Press. Oxford, New York, 1st edition, 1991.

[14] William S. Price. Pulsed-field gradient nuclear magnetic resonance as a tool for studying translational diffusion: Part II. experimental aspects. *Concepts in Magnetic Resonance*, 10:197–237, 1997.

[15] Ian W. Hamley. *Introduction to Soft Matter-Revised Edition Synthetic and Biological Self-Assembling Materials*. John Wiley & Sons Ltd, Chichester, 1st edition, 2007.

[16] Thomas G. Mezger. *The Rheology Handbook*. Vincentz Network GmbH and Co. KG, Hannover, Germany, 2nd edition, 2006.

[17] Raymond Mckennell. Cone-plate viscometer comparison with coaxial cylinder viscometer. *Journal of Analytical Chemistry*, 28:1710–1714, 1956.

[18] Alexander Ya. Malkin and Avraam I Isayev. *Rheology: concepts, methods and applications*. ChemTec, Toronto, 1st edition, 2006.

[19] Christopher W. Macosko. *Rheology Principles, Measurements, and Applications*. John Wiley & Sons, Canada, 1st edition, 1994.

Chapter 3

An Overview of Self-Assembly: Polymers, Surfactants, and Proteins

Soft matter physics is a branch of science which represents a class of materials that are neither simple liquids nor crystalline solids. These materials can be easily deformed under thermal fluctuations at room temperature. Soft materials are very common in our daily life and they have wide applications.[1,2] Materials composed of polymers and surfactants have applications which include laxatives, lubricants, skin creams, cosmetics, and detergents. Proteins represent an essential component of the biological cell. Small-molecule liquid crystals, too, fall under the category of soft materials. However, the systems we are discussing in this chapter are macromolecular systems such as polymers, micelles, and proteins.

3.1 Polymers

A polymer is a giant molecule or macromolecule composed of many repeat units which are bonded to each other via covalent bonds. Each single structural unit is called a monomer. Based on the type of repeat unit or monomer, a polymer is classified as homopolymer or copolymer. A homopolymer

is constructed from only one type of monomer while a copolymer's structure includes two different types of monomers or more.[2]

Polymer molecules are characterized using various physical and chemical parameters. Some physical parameters are the degree of polymerisation, the number averaged molecular weight, the weight average molecular weight, and the polydispersity.[2] The degree of polymerisation is the number of structural repeat units or monomers in a polymer chain. Unlike atoms, or small-molecule synthesis, polymer synthesis never yields molecules with identical degree of polymerization. The number average molecular weight $\overline{M_n} = \sum N_i M_i / \sum N_i$, the weight average molecular weight $\overline{M_w} = \sum N_i M_i^2 / \sum N_i M_i$ and the polydispersity index PDI = $\overline{M_w}/\overline{M_n}$ are used to characterize a polymer solution or a polymer melt that consists of the same type of molecules but with different chain lengths, where N_i is the number of polymer chains (molecules) of molecular weight M_i.[2]

In addition, as a chemical parameter, the functionality of a monomer controls the number of its chemical bonds with other monomers. If the functionality of each monomer in a polymer chain is two then the polymer is considered to be a linear polymer (i.e. single chain polymer) while if the functionality of each monomer is more than two then the polymer is classified as a branched polymer.

3.1.1 The Hydrodynamic Radius and Brownian Motion

A common feature of all classes of molecules described in this chapter is that, in solution, they are Brownian objects. The hydrodynamic radius R_H is a parameter accessible to a variety of experimental techniques. Some techniques used are nuclear magnetic resonance (NMR),[3] dynamic light scattering (DLS),[4] and small angle X-ray (SAXS), and neutron scattering.[5,6] The hydrodynamic radius is used to characterize the size of any molecule or aggregate: polymer, protein, or micelle. It is broadly defined as a radius of a sphere which diffuses in the same way as the suspended diffusive

molecule in a bulk solution.

Consider a suspended solute molecule in a bulk solution. This molecule is exposed to random collisions with solvent molecules due to thermal energy. This creates a force which is fluctuating as a function of time, which forces the suspended molecule to move randomly with the passage of time. This random motion is called Brownian motion. Since the molecule moves randomly between the time steps then the mean displacement of the molecule is zero (i.e. $\langle R(t) \rangle = 0$), while the mean-squared displacement is[2,7]

$$\langle R^2(t) \rangle = 6Dt. \tag{3.1}$$

Einstein[8] and Sutherland[9] independently found that the diffusion coefficient can be related to the Stokes drag of the suspended particle, $D = (K_B T)/\xi_{Stokes}$. For an isolated sphere $\xi_{Stokes} = 6\pi\eta R_H$ and

$$D = \frac{K_B T}{6\pi\eta R_H} \tag{3.2}$$

where D is the diffusion coefficient of the suspended molecule and η is the viscosity of the solution. Equation 3.2 is known as Stokes-Einstein-Sutherland relation. We see from equation 3.2 that the hydrodynamic radius R_H is inversely proportional to the diffusion coefficient D of the suspended molecule. So we are able to estimate the size of a suspended particle in a solution by measuring the diffusion coefficient of the molecule itself. A key challenge in a real solution is that Stokes-Einstein-Sutherland equation is only truly valid at infinite dilution. Therefore, extracting the hydrodynamic radii in solutions that are not in the dilute limit is not always straight forward.

3.1.2 Obstruction Effects and Hydrodynamic Corrections

In the dilute regime, the interactions between suspended particles are negligible. The only available interaction is the interaction between suspended particles and the small size solvent molecules which cause a motion of a suspended molecule in a random walk path. At higher concentrations,

57

the situation is more complicated. In these systems, the suspended macromolecules are in a regime where there are significant interactions between macromolecules. These interactions hinder the random walk motion of macromolecules inside the bulk solution. So in addition to the interaction between macromolecules and solvent particles in the solution, the hydrodynamic interaction, which is an indirect interaction, takes place at least between the nearby macromolecules, where simply, the motion of a suspended macromolecule creates a solvent flow field which can affect the random walk path of other macromolecules in the solution. In addition, the existence of charged suspended macromolecules creates an excess hindrance to the random walk motion due to the existence of electrostatic interactions. The strength of this hindrance decreases with increasing the ionic strength of the solution between charged macromolecules.[10]

The diffusion of a macromolecule on a time scale at which the hydrodynamic interaction dominates over direct interactions (Coulomb, van der Waals, etc.) is defined as a short-time self diffusion[11] D_s. In the long time limit, the macromolecule diffuses over a distance lager than the interparticle distance. In addition to the direct interactions between macromolecules, direct collisions take place between nearby macromolecules.[11] In this long-time limit, the macromolecular diffusion is defined as long-time self diffusion D_L.

A few theories have been established which consider the reduction in the self-diffusion of macromolecules due to either obstruction effect or direct interparticle interactions. One model, due to Han and Herzfeld,[12] finds that the reduction in the self-diffusion (equation 3.3) of a biological macromolecule (i.e. protein molecule) due to the effect of crowding takes the form

$$D = D_o \exp\left(-\frac{2}{3}\left(3\frac{\Phi}{1-\Phi} + \frac{9}{2}\frac{\Phi^2}{(1-\Phi)^2} + \frac{9}{4}\frac{\Phi^3}{(1-\Phi)^3}\right)\right), \quad (3.3)$$

where D_o is the self-diffusion of a macromolecule in the dilute limit and Φ is the macromolecule volume fraction. This model treats the self-diffusion of a globular protein molecule as a hard sphere diffusing among other spherocylinder proteins with different sizes and with an isotropic distribu-

tion. The formation of protein aggregates in the solution causes a reduction in the hindrance of a globular protein by other protein molecules. Moreover, anisotropic alignment of spherocylinder proteins cause an extra reduction in the hindrance.

Two other models, due to Medina-Noyola et al.[11] (equation 3.4) and Tokuyama and Oppenheim[13] (equation 3.5), have been derived to deal with a reduction in the self-diffusion D_L of the colloidal particles as hard spheres in the long-time diffusion limit. Medina-Noyola model deals with the self-diffusion in the long time limit in a system of charged hard sphere particles. Both direct interactions (van der Waals and Coulomb interactions) and hydrodynamic interactions are included. Medina-Noyola et al. found an expression of the form

$$D_L = D_0 \frac{(1 - \Phi)^3}{[1 + (3/2)\Phi + 2\Phi^2 + 3\Phi^3]}, \tag{3.4}$$

, Tokuyama and Oppenheim show that in the long-time limit the hydrodynamic interactions dominate the dynamics of uncharged hard-sphere particles more than the direct interactions (van der Waals), and find an expression of the form

$$D_L \approx D_0 \frac{\left(1 - \frac{9\Phi}{32}\right)}{1 + H(\Phi) + \frac{(\Phi/0.57)}{(1-\Phi/0.57)^2}} \tag{3.5}$$

where $H(\Phi) = \frac{(2A^2)}{1-A} - \frac{B}{(1+2B)} - \frac{AB(2+B)}{(1+B)(1-A+B)}$, $A = \sqrt{9\Phi/8}$, and $B = 11\Phi/16$.

Figure 3.1 shows the variation of the scaled diffusion coefficient as a function of molecular volume fraction in three different models. The self-diffusion coefficient is scaled by the theoretical value at zero volume fraction.[14,15] Based on these models, figure 3.1 shows that the reduction in the self-diffusion in a system composed of a globular protein (black line) is smaller than the reduction in systems composed of charged (line) or uncharged colloids (red line). Also, as can be seen from figure 3.1, the models differ significantly from each other even in the limit of low volume fraction Φ.
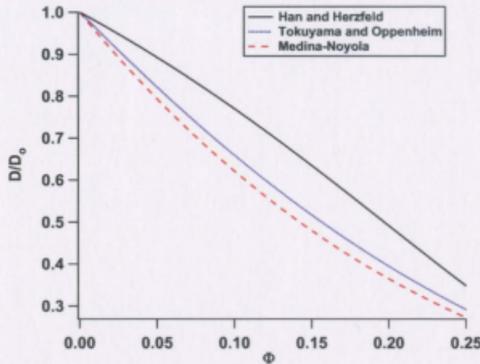
Figure 3.1: The long-time self-diffusion coefficients obtained in the works of Han and Herzfeld black (solid) (globular protein), Tokuyama and Oppenheim blue (dotted) (charged colloids), and Medina-Noyola red (dashed) (uncharged colloids) line .

3.1.3 Radius of Gyration

The size of either a linear or branched polymer can be characterized by a useful quantity called the radius of gyration R_g. The squared radius of gyration is defined by the equation

$$R_g^2 = \frac{1}{N} \sum_{i=1}^{N} (\overrightarrow{R_i} - \overrightarrow{R_{cm}})^2 = \frac{1}{N^2} \sum_{i=1}^{N} \sum_{j \neq i}^{N} (\overrightarrow{R_i} - \overrightarrow{R_j})^2 \qquad (3.6)$$

where $\overrightarrow{R_{cm}} = \frac{\sum_{j=1}^{N} M_j \overrightarrow{R_j}}{\sum_{j=1}^{N} M_j} = \frac{1}{N} \sum_{j=1}^{N} \overrightarrow{R_j}$ is the polymer's center of mass vector for a specific polymer conformation and $\overrightarrow{R_i}$ and $\overrightarrow{R_j}$ are the position vectors of the i-th and j-th monomers, respectively, for a specific polymer conformation. A polymer chain in melt or solution changes conformation rapidly in time. The quantity that is accessible experimentally is the ensemble average of the square radius of gyration over all possible configurations: $\langle R_g^2 \rangle$.

60

3.1.4 Persistence Length

Many models have been used in order to estimate physical volume occupied by a polymer chain. One of the simplest is the freely rotating chain model, which assumes that a polymer chain consists of n backbone monomers which are connected to each other with bond vectors $(\vec{r_1}, \vec{r_2}, \vec{r_3}, ..., \vec{r_i}, ...)$. All bond vectors have the same length ℓ with different orientations such that the angles between any two nearby bond vectors is the same (i.e. θ) (figure 3.2). The mean-square-end-to-end distance[7] $\langle R^2 \rangle = \langle \vec{R_n} \cdot \vec{R_n} \rangle = \sum_{i=1}^{n} \sum_{j=1}^{n} \langle \vec{r_i} \cdot \vec{r_j} \rangle$, where $\vec{r_i}$ and $\vec{r_j}$ are two bond vectors which are separated by $j - i$ other bond vectors.
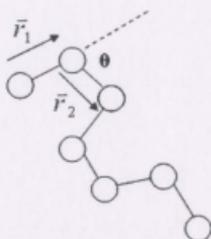
Figure 3.2: A schematic representation of a polymer chain in the freely rotating chain model.

Simply, $\vec{r_j}$ has two components: one that is perpendicular and one that is parallel to the nearby bond vector $\vec{r_{j-1}}$. The average of the normal component of $\vec{r_j}$ is zero since this component can rotate freely in any direction perpendicular to $\vec{r_{j-1}}$, i.e., there is an equal probability of finding the component oriented along any direction perpendicular to $\vec{r_{j-1}}$. This assumption is an essential part of a freely rotating chain model. The other component, which is along $\vec{r_{j-1}}$, is equal to $\ell \cos \theta$. The correlation between bond vectors $\vec{r_i}$ and $\vec{r_j}$ is $\langle \vec{r_i} \cdot \vec{r_j} \rangle = \ell^2 (\cos \theta)^{(j-i)}$. For large $(j - i)$, $(\cos \theta)^{(j-i)}$ becomes very small. Indeed, the correlation can be written in an exponential form:

$$\langle \vec{r_i} \cdot \vec{r_j} \rangle = \ell^2 \exp\left(-\frac{(j-i)\ell}{\ell_p}\right) \tag{3.7}$$

where ℓ_p is the persistence length.

3.1.5 Freely Jointed Chain Model, Equivalent Freely Jointed chain model, and Kuhn Length

The freely jointed chain model assumes that a polymer chain is composed of n segments (i.e. monomers) each with length ℓ such that each segment rotates freely, independently, and it is uncorrelated to any other segment's orientation. Based on this model, each segment (monomer) in a polymer chain with n monomers has n random possible steps which are not correlated to each other.[2,7] According to this model, the mean-square end-to-end distance is simply given as[2,7]

$$\left\langle R^2 \right\rangle = \sum_{i=1}^{n} \sum_{j=1}^{n} \left\langle \vec{r_i} \cdot \vec{r_j} \right\rangle = \ell^2 \sum_{i=1}^{n} \sum_{j=1}^{n} \left\langle \cos\theta_{ij} \right\rangle = n\ell^2 \qquad (3.8)$$

where $\left\langle \cos\theta_{ij} \right\rangle$ measures the angular correlation between i-th and j-th segment and is zero for $i \neq j$.

Equation 3.8 can be written in a more general form (not assuming uncorrelated bond angles):

$$\left\langle R^2 \right\rangle = \ell^2 \sum_{i=1}^{n} \sum_{j=1}^{n} \left\langle \cos\theta_{ij} \right\rangle = \ell^2 \sum_{i=1}^{n} C_i = nC_n\ell^2 \qquad (3.9)$$

where: $C_i = \sum_{j=1}^{n} \left\langle \cos\theta_{ij} \right\rangle$ and $C_n = \frac{1}{n}\sum_{i=1}^{n} C_i$. The quantity C_n is called Flory's characteristic ratio. For a long polymer chain (i.e. $n \to \infty$), $\left\langle R^2 \right\rangle = n\ell^2 C_\infty$.

Another simple model is the equivalent freely jointed chain model. This model is based on the freely jointed chain model and it assumes that the polymer chain includes N (where N < n) subsegments called Kuhn monomers which are not correlated to each other. Each subsegment has a length b, called the Kuhn length, where $b > \ell$. Each Kuhn monomer includes several monomers in it. Based on this, the Kuhn length b of a long polymer chain can be written in terms of mean square end-to-end distance $\left\langle R^2 \right\rangle$ equation 3.9 and the end-to-end distance R_{max} of the equivalent freely polymer chain:

$$\left\langle R^2 \right\rangle = Nb^2 = bR_{max} = C_\infty n\ell^2. \qquad (3.10)$$

As an example, let us consider a linear chain, non-ionic polymer polyethylene oxide, one of the components in our study of polymer-surfactant aggregates (Chapter 4). The PEO chain in the

study has ≈ 450 monomers (each of length ≈ 0.44 nm). The Kuhn length[16] $b \approx 1.8$ nm and the Flory characteristic ratio[7] $C_\infty = 6.7$.

3.1.6 Polymer Solutions and Models of Polymer Dynamics

Polymer solutions are classified into either dilute, semidilute, or concentrated solutions depending on the volume fraction of the polymer molecules in the solution. In the dilute regime, the average distance between polymer chains is larger than the average size of a polymer chain. So a polymer chain diffuses freely without any obstructions from other polymer chains. In the semidilute regime, the pervaded volume of a polymer chain includes both solvent molecules and other polymer chains which form entangled network. In this regime the polymer exhibits strongly viscoelastic behavior, it is therefore very interesting to be considered in some detail.[7]

In the semidilute regime, there is a characteristic length below which a monomer in a polymer chain is completely surrounded by solvent molecules and some monomers from the same polymer chain. This characteristic length is called the correlation length ζ. Beyond this length the monomer is surrounded not only by solvent and monomers from the same polymer chain, but also monomers from other nearby chains. A "blob" of diameter ζ contains a number g of Kuhn monomers in it. A schematic diagram is shown in figure 3.3. The correlation length ζ scales as

$$\zeta \approx bg^\nu \tag{3.11}$$

where b is the Kuhn monomer length and ν is a scaling exponent that has a value of 1/2 for a random walk and 0.588 for a self-avoiding walk.[2,7] At length scales which are much smaller than the correlation length, a thermal blob of characteristic length ζ_T can be defined. We can think of a polymer chain as a coil which includes a number of thermal blobs. At length scales smaller than the thermal blob, the cumulative interactions (i.e. the hydrodynamic interactions and excluded volume interactions) between the polymer section and the solvent molecules is less than the thermal energy.

Therefore, when coarse-grained at this length scale, the polymer chain exhibits a random walk.
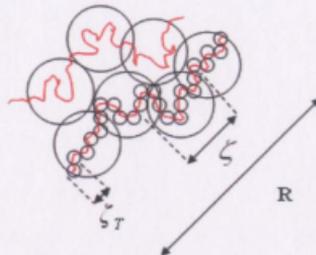
Figure 3.3: Schematic diagram of a polymer chain. The plot shows the end-to-end distance R, the blob correlation length ζ, and the correlation length ζ_T of the thermal blob.

For length scales larger than the thermal blob but smaller than the correlation length (i.e. $\zeta_T <$ length scale $< \zeta$), the net interactions between the polymer section and the solvent molecules dominates and becomes larger than the thermal energy. At this length scale, the excluded volume effect becomes important and the polymer chain section exhibits a self-avoiding walk. On length scales larger than the correlation length ζ, at which the overlap between the polymer chains is seen, the polymer chain exhibits a random walk again with the excluded volume interactions screened due to overlapping between chains.

The overlap volume fraction Φ^* separating the dilute regime from the semi-dilute regime is defined as[7]

$$\Phi^* \approx b^3 \frac{N}{R^3} \qquad (3.12)$$

where $R = bN^\nu$ is the root mean square end to end distance of a polymer chain with N Kuhn monomers and Kuhn length b and $V \approx R^3$ is the volume of the solution spanned by a polymer chain (known as the pervaded volume). Equation 3.12 shows that the overlap concentration Φ^* measures the volume fraction of a polymer chain inside the pervaded volume (V).

Based on the schematic diagram[7] of a polymer chain in figure 3.3, we may write the end-to-end

distance R in terms of the number of thermal blobs (N/g_T) and the thermal blob size (ζ_T)

$$R \approx \zeta_T \left(\frac{N}{g_T} \right)^{\nu} \tag{3.13}$$

where g_T is the number of Kuhn monomers in the thermal blob.

However, we mentioned that on length scales smaller than the thermal blob size ζ_T the polymer segment exhibits a random walk with $\zeta_T = b \, g_T^{0.5}$. On the other hand, on length scales on the order of magnitude of the thermal blob size or bigger than the thermal blob size ζ_T, the excluded volume interaction takes place. This entropic interaction is in the order of magnitude of the thermal energy

$$K_B T \nu \frac{g_T^2}{\zeta_T^3} \approx K_B T \tag{3.14}$$

where ν is the volume occupied by the Kuhn monomer.

Combining equation 3.14 with the fact that $\zeta_T = b \, g_T^{0.5}$, we may write the thermal blob size ζ_T and the number of Kuhn monomer g_T in terms of the Kuhn length b and the volume occupied by the Kuhn monomer ν

$$g_T \approx \frac{b^6}{\nu^2}, \; \zeta_T \approx \frac{b^4}{\nu}. \tag{3.15}$$

By combining both equation 3.15 and equation 3.13, we may write the end to end distance in terms of the volume occupied by the Kuhn monomer ν, the length of the Kuhn monomer b, and the number of Kuhn monomers

$$R \approx b \left(\frac{\nu}{b^3} \right)^{2\nu-1} N^{\nu}. \tag{3.16}$$

By substituting equation 3.16 in equation 3.12, the overlap volume fraction can be presented as follow

$$\Phi^{\star} \approx \left(\frac{b^3}{\nu} \right)^{6\nu-3} N^{1-3\nu} \propto N^{1-3\nu}. \tag{3.17}$$

semi-dilute regime and concentrated regime of a polymer solution on length scales larger than the blob correlation length ζ. In these regimes, a polymer chain exhibits a random walk.

Each monomer in a polymer chain experiences friction with an associated friction coefficient ξ such that the total friction experienced by the whole chain is $\xi_R = N\xi$. Using the Stokes-Einstein-Sutherland equation $D_R = (K_B T)/(N\xi)$, where D_R represents the diffusion coefficient of the Rouse chain, we may write[7]

$$\tau_R = R^2/D_R = (R^2 N\xi)/(K_B T) \tag{3.22}$$

where τ_R is called the Rouse time. Once again using the scaling relation, the Rouse time can be written

$$\tau_R = \frac{\xi b^2}{K_B T} N^{1+2\nu} \equiv \tau_0 N^{1+2\nu}. \tag{3.23}$$

Here, $\tau_0 = (\xi b^2)/(K_B T)$ is the Kuhn monomer characteristic time. On a time scale smaller than τ_0, the Rouse polymer chain shows elastic behavior while on a time scale longer than the Rouse time τ_R of the polymer chain, Rouse polymer chain is diffusive and shows viscous behavior. In the intermediate time scale (i.e. $\tau_0 < t < \tau_R$), the polymer chain exhibits viscoelastic behavior.[7]

The Zimm model[7, 18] considers the hydrodynamic interactions between monomers on the polymer chain and between monomers and solvent molecules in the pervaded volume. This is valid for length scales smaller than the blob correlation length. The Zimm model is valid for a dilute polymer solution where only monomers from the same chain interact with each other through strong hydrodynamic interactions. In this regime, a polymer chain exhibits a self-avoiding walk.

In the Zimm model, a polymer chain diffuses as one unit and drags with it solvent molecules which are highly affected by the hydrodynamic interactions associated with monomers in the chain. The total friction ξ_Z experienced by a chain is on the order of $\eta_s R$ where η_s is the solvent viscosity and R is the end to end distance of a polymer chain. Based on the Stokes-Einstein-Sutherland

equation, the Zimm chain diffuses a distance of the order of the chain size R during the Zimm time scale τ_Z and we can write

$$\tau_Z \approx \frac{R^2}{D_Z} \approx \frac{\eta_s}{K_BT}R^3. \tag{3.24}$$

Back to the Rouse model, the Rouse time can be written in terms the characteristic time ($\tau_\zeta = (\eta_s/K_BT) \zeta^3$) of the blob $\tau_R = \tau_\zeta (N/g)^{1+2\nu}$ where $\nu = 0.5$ since in the Rouse model a polymer chain exhibits a random walk. On length scales smaller than the blob correlation length ζ, we are in the regime where the Zimm model is valid. Therefore, using equation 3.21, the characteristic time of the blob is[7]

$$\tau_\zeta \approx (\zeta)^3 \frac{\eta_s}{K_BT} \approx \frac{\eta_s}{K_BT} b^3 \left(\frac{b^3}{v}\right)^{3(2\nu-1)/(3\nu-1)} \Phi^{-(3\nu)/(3\nu-1)}. \tag{3.25}$$

Using both equation 3.25 and equation 3.20, the Rouse time τ_R can be written in terms of Kuhn monomer length b, number of Kuhn monomers N, and the volume fraction of polymer solution Φ

$$\tau_R \approx \frac{\eta_s b^3}{K_BT} N^2 \Phi^{(2-3\nu)/(3\nu-1)}. \tag{3.26}$$

In addition, using equation 3.19 and equation 3.20, the polymer chain end to end distance R in the semi-dilute regime is given as:[7]

$$R \approx \zeta \left(\frac{N}{g}\right)^{\frac{1}{2}} \approx bN^{1/2}\Phi^{-(2\nu-1)/(6\nu-2)}. \tag{3.27}$$

Using equation 3.22, equation 3.27, and equation 3.26, the diffusion coefficient D of a polymer chain in semi-dilute regime can be written in term of the polymer volume fraction

$$D \approx \frac{K_BT}{\eta_s bN} \Phi^{-(1-\nu)/(3\nu-1)} \equiv D_Z (\Phi/\Phi^\star)^{-(1-\nu)/(3\nu-1)} \tag{3.28}$$

where the total polymer volume fraction and the correlation volume fraction must be the same for densely packed correlation volumes. The total polymer volume fraction Φ and the overlap volume

68

fraction Φ^* are related to the polymer mass concentration C and to the overlap concentration C^* respectively[7]

$$\Phi = \frac{C}{\rho} = C \frac{v_{mon} N_{Av}}{M_{Mon}} \qquad (3.29a)$$

$$\Phi^* = \frac{C^*}{\rho} = \frac{N v_{mon}}{V} \qquad (3.29b)$$

where the polymer mass concentration is the ratio of the mass of the polymer dissolved in a solution and the total volume of a solution, N_{Av} is Avogadro's number, v_{mon} is the volume occupied by a single chemical monomer, V is the pervaded volume of a polymer chain, and ρ is the polymer density or the ratio of the monomer molar mass (M_{mon}) and monomer molar volume ($v_{mon} N_{Av}$).

Equation 3.28 allows a comparison between the dynamics of a polymer chain in the Rouse model and Zimm model. Both models predict a power law scaling as a function of the volume fraction. In the Zimm model, a polymer chain exhibits a self-avoiding walk with $v = 0.588$. This predicts an exponent $(1 - v)/(3v - 1) = 0.54$ in equation 3.28. On the other hand, in the Rouse model, a polymer chain exhibits a random walk with $v = 0.5$. This would predict an exponent $(1 - v)/(3v - 1) = 1$ in equation 3.28.

Equation 3.28 is used in chapter 5 to extract information about the dynamics in the semidilute regime of a `living polymer´ wormlike micellar solution.

3.2 Surfactants and Micelles

Surfactants or amphiphiles belong to a category of molecules that have two attached chemical groups with completely different tendencies to form bonds with water molecules. Typically one of the chemical groups is hydrophobic and is non-soluble in water, while the other chemical group is a hydrophilic head-group which is soluble in water and has the ability to form hydrogen bonds

with water molecules.[2] Often the hydrophobic group is a hydrocarbon-rich chain (such as an alkyl chain) and it is called the hydrophobic "tail".

According to the chemical properties of both hydrophobic and hydrophilic sections, simple surfactants (amphiphiles) can be classified into four categories.[2] First, these are anionic surfactants which have single hydrocarbon chain bonded to anionic head-group. One example is sodium dodecyl sulphate (SDS) which dissociates in an aqueous medium into the $C_{12}H_{25} - (SO_4)^{-1}$ ion and Na^+ ion, and sodium stearate where the surfactant ion is $C_{18}H_{37} - (COO)^{-1}$. These kind of surfactants are commonly used in detergent products. SDS self-assembles into almost spherical as well as rodlike micelles. A system composed of anionic surfactant SDS and non-ionic polymer polyethylene oxide PEO is studied extensively in chapter 4 using NMR.

The second category of surfactants are cationic surfactants. A cationic surfactant has a single hydrocarbon chain bonded to a cationic head-group. One example is hexadecyltrimethyl-ammonium bromide (CTAB) which consists of $C_{16}H_{33} - N^{+1}(CH_3)_3$ ion and a Br^- ion. CTAB has a tendency to form elongated cylindrical micelles.

The third category of surfactants are non-ionic surfactant. These have single hydrocarbon chains bonded to a non-ionic head-group such as $C_{12}H_{25} - (OCH_2CH_2)_5$. Also surfactants which includes two hydrocarbon chains bonded to a non-ionic head-group such as pluronic P105. Pluronic P105 includes two hydrocarbon chains $(OCH_2C_2H_5)_{58}$ attached to $(OCH_2CH_2)_{37}$ head group, where these kind of surfactants are used in cosmetics and some pharmaceuticals.

The fourth category of surfactant are zwitterionic surfactants. The surfactant ion has zero net charge such as tetradecyl dimethyl ammonium propane sulfonate (TDPS) $C_{19}H_{41}NO_3S$. It has recently been shown to form long cylindrical micelles. The structure and dynamics of an elongated cylindrical micellar system composed of zwitterionic surfactant TDPS and anionic surfactant SDS in brine is studied in studied in chapter 5. Complementary techniques are used, including diffusometry, relaxometry, deuterium NMR, and rheometry to extract information about the microscopic structure of this system.

70

3.3 Micellar Aggregates and Cluster Phases

An amphiphilic molecule includes a hydrophobic chain and a hydrophilic head-group. Its hydrophilic groups energetically prefer maximal exposure to water molecules while its hydrophobic groups prefer other hydrophobic groups.
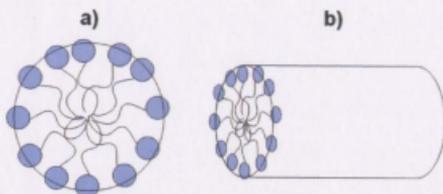
Figure 3.4: Micellar Shapes: a) Spherical micelle and b) Cylindrical micelle

The presence of an amphiphilic molecule in aqueous solution breaks the nearby hydrogen-bond network between water molecules because this molecule has a hydrophobic component that is not able to form hydrogen bonds with the nearby water molecules. It forces the nearby water molecules to rearrange themselves into configurations that maximize the hydrogen bonds. The number of configurations will be less than the number of available arrangements in the absence of an amphiphilic molecule. As a result, the number of available configurations of water molecules in the presence of an amphiphilic molecule decreases, which causes a decrease in the entropy and so an increase in the free energy. This imposes amphiphiles to form finite size aggregates. The simplest of these aggregates are micelles. A micelle is a fluid-like object which is suspended in an aqueous solution. Micelles can be spherical (figure 3.4a) or cylindrical (figure 3.4b).[2] More generally, surfactants ˜micro-phase-separate˝in solution with a large number of possible aggregate structures. The amphiphilic nature of the surfactant molecule is crucial to micro-phase-separate.

The balance between molecular shape and size as well as different interactions (electrostatic

71

repulsion and hydrophobic interactions) plays a crucial role in specifying the preferred micellar shape and the geometry of the amphiphilic aggregates. The geometry of a micellar amphiphilic aggregate defines by the surfactant packing parameter $p = v/(\ell_c a_o)$, where a_o is the optimum head-group area of an amphiphilic molecule, ℓ_c is the chain length of the hydrocarbon chain, and v is the hydrocarbon chain volume. Consider a spherical micelle of radius r composed of M molecules each with volume v. The total micellar volume $V = 4\pi r^3/3 = Mv$ and the surface area $A = 4\pi r^2 = Ma_o$ with $r = 3v/a_o$. The condition for the formation of a spherical micelle is satisfied when the radius r of the micelle is less than the critical chain ℓ_c, $v/(\ell_c a_o) \leq 1/3$. On the other hand, increasing the ionic strength of the solution causes an increase in the screening of the electrostatic repulsion interaction between the ionic head groups which reduces the optimum head-group area a_o. As a result, the surfactant packing parameter $v/(\ell_c a_o)$ increases and then the spherical micelles transform to cylindrical micelles when $(1/3) < p \leq (1/2)$.[19]

The tendency of molecules to form equilibrium aggregates has not been observed only in surfactant solutions. It has been shown that protein and colloid systems form equilibrium mesoscopic aggregates that have finite size.[20] However, inspite of the large number of studies that have been accomplished in the field of "equilibrium clusters" in the last few years, important questions have not fully answered. What are the exact potentials responsible for the formation of the clusters? What is the origin of these potentials? Finally, what are the factors that impact the cluster size?[20]

Therefore, the formation of what are called "equilibrium clusters" in colloidal systems and macromolecular systems have been investigated extensively. Despite the fact that recent studies investigate cluster formation in different systems, we will explain in more detail the studies that explore cluster formation in systems that are more relevant to our research field.

Recently, NMR-based studies constituting chapter 6 of this thesis have revealed strong evidence for the formation of a coexistent phase that consists of lysozyme clusters and monomers.[21] Cardinaux et al.[22] also find that the fraction of lysozyme monomers in the cluster phase increases by increasing the lysozyme volume fraction. Computer simulation studies[23] also find the existence

72

of protein clusters inside the lipid biomembrane. These protein assemblies are formed due to the balance between short-range attraction and long-range attraction. Within the lipid membrane there are hundreds of different types of protein. Each type of protein molecule has an affinity to form clusters of the same type. In charged colloid systems,[24] computer simulation showed an evolution of the cluster shape and size from small finite size clusters at low volume fraction to one large cluster that spans all the colloids in the system.

Another example is a theoretical study by Groenewold et al.[25] They showed in particular that head-tail anisotropic interactions (such as those that result in micelles and other micro-phases) are not necessary in order to form stable, finite-size clusters in equilibrium. The stability of this cluster phase is attributed to the balance between the long-range repulsion and short-range interactions. This conclusion was confirmed experimentally by Stradner et al.,[26] but questioned by experimental work by Shukla et al.[27] Our experiments in chapter 6 are designed to resolve these questions.

Stradner et al.[26] reported the formation of finite size clusters in a colloidal system. The equilibrium cluster formation in this system was driven by the combination of long-range electrostatic repulsion due to the charge on the colloids and short-range attraction due to non-adsorbed polymers. Similar aggregates were detected experimentally in solutions of globular protein lysozyme.[22,26,28] The hypothesis of two combined potentials was supported by computer simulation studies in colloidal[29] and protein[22,30,31] systems. Moreover, extensive studies including scattering techniques,[27,32–35] nuclear magnetic resonance,[14,33,36,37] and computer simulation studies[31,38] have been accomplished in the field of irreversible, non-equilibrium cluster formation for lysozyme solutions.

3.3.1 Spherical Micelles

In order to make our understanding of micelle formation quantitative, let us consider a solution which contains solute molecules with volume fraction ϕ such that at equilibrium $\phi = \sum_{N=1}^{\infty} X_N$, where X_N is the volume fraction of solute molecules in aggregates which includes N molecules. At

equilibrium, the chemical potential μ_N of a molecule in an aggregate which includes N molecules is[2, 39]

$$\mu_N = \mu_N^o + \frac{K_B T}{N} \log \frac{X_N}{N} \qquad (3.30)$$

where μ_N^o is the free energy per molecule in an isolated aggregate of N molecules. Rewriting equation 3.30, the volume fraction X_N is given[2, 39]

$$X_N = N \exp\left(\frac{N(\mu_N - \mu_N^o)}{K_B T}\right) = N \left[X_1 \exp \frac{(\mu_1^o - \mu_N^o)}{K_B T}\right]^N \qquad (3.31)$$

where X_1 is the volume fraction of individual solute molecules in the bulk solution (i.e. aggregates of size one or monomers). So according to equation 3.31, if the free energy μ_1^o per molecule or monomer in monomeric state is equal to the free energy μ_N^o per molecule in an N-molecules aggregate, then $X_N = N [X_1]^N$. Since X_1 is always less than one so $X_N \ll 1$. Under this condition most of molecules are in a monomeric state. According to equation 3.31, the main condition to form aggregates of N monomers is $\mu_N^o < \mu_1^o$ for some value of N (e.g. having a minimum value of μ_N^o as a function of N). At this point, for any amphiphile added to the solution, the volume fraction X_1 of the amphiphilic in the monomeric state stays approximately constant, while the volume fraction X_N of the amphiphilic in the aggregate state starts increasing gradually (figure 3.5). Interestingly, this picture, while sketched in text books has not been directly demonstrated in experiments. Such a direct demonstration is presented in chapter 4.

As described above, the formation of a spherical micelle is based on the fact that the radius r of the micelle is less than the critical chain length ℓ_c. Also, the micelle must include a number of surfactant molecules $N = M$ at which the free energy per molecule in isolated N-molecule aggregates $\mu_N^o = \mu_M^o$ is minimum. If the number of surfactant molecules N is smaller than the optimum M, this causes an increase in the area per head-group which exposes the hydrophobic chains more to the water in bulk solution which cause an increase the free energy. On the other hand, if the number of molecules N is larger than the optimum number M, this causes an increase
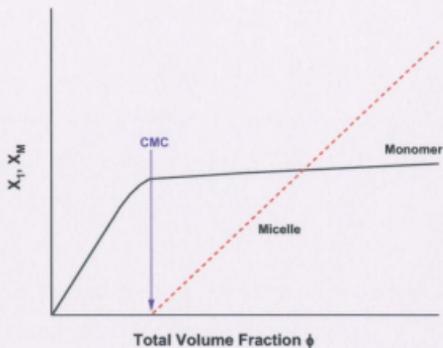
Figure 3.5: The volume fraction of amphiphile molecules in monomeric state X_1 (black line) and micellar state X_M (red dashed line) as a function of total volume fraction of amphiphile. The critical micellar concentration (CMC) is both the plateau value of X_1 curve (on the y-axis) and the volume fraction value (on the x-axis) where X_M becomes non-zero.

in the electrostatic repulsion between the head-groups since they are highly packed on the surface of the micelle which force some head-groups to enter the core of the micelle which causes an increase in the free energy.

By rewriting equation 3.31 in terms of the volume fraction X_M of amphiphile molecules in optimum spherical aggregates, we get the relation between the volume fraction X_1 of free amphiphile molecules in the bulk solution and the volume fraction of amphiphile molecules in the optimum spherical aggregates:[2]

$$X_M = M \left[\frac{X_1}{\exp\left(\frac{-\Delta\mu}{K_B T}\right)} \right]^M = M \left[\frac{X_1}{\phi_c} \right]^M \qquad (3.32)$$

where $\Delta\mu = \mu_1^o - \mu_M^o$ and $\phi_c = \exp\left(\frac{-\Delta\mu}{K_B T}\right)$ is the total volume fraction of amphiphiles above which optimum size micelles start forming inside the solution. ϕ_c is the characteristic value for the critical micellar concentration CMC. The total volume fraction $\phi = \sum_{N=1}^{\infty} X_N$ of amphiphiles is either equal to X_1 if $\phi < \phi_c$ (i.e. no micelles below ϕ_c) or it is equal to $\phi_c + X_M$ if $\phi > \phi_c$. Thus, ϕ_c also represents the maximum volume fraction of free amphiphiles in the bulk solution. According to equation 3.32, if the concentration X_1 is small, $X_1 < \phi_c$ then the volume fraction X_M of the spherical micelles is approximately zero. When X_1 approaches ϕ_c then X_M starts to increase gradually (figure 3.5).

3.3.2 Cylindrical Micelles and Wormlike Micelles

We have mentioned in section 3.3 that the balance between the electrostatic repulsion interaction and hydrophobic interaction between surfactant molecules in a micelle plays a role in specifying a shape of amphiphilic aggregates.

Ionic amphiphiles represents a category of surfactant molecules which have an ionic head group; an example is sodium dodecyl sulfate (SDS) which is used in household soaps. It has an anionic SO_4^- head group and releases Na^+ ion into solution. These molecules form spherical micelles with $p \leq 1/3$ at the critical micelle concentration CMC. As the total concentration of

molecules increases above the CMC value, the concentration of sodium ions increases in the solution (i.e. an increase in the ionic strength of the solution). This causes a transformation from a spherical to a cylindrical micellar state.[19]

Cylindrical micelles behave like charged rigid rods. Adding salt or increasing the surfactant concentration cause an increase in the concentration of counterions in the solution. This causes a decrease in the electrostatic repulsions among charges on a micellar backbone.[40] This is associated with an increase in the energy required to create two hemispherical end-caps (known as the scission energy) of a micelle.[41] As a result, this might promote the growth of a micellar chain either by association of monomers at the chain ends or by recombining with other neaby chain ends.[42] Longer micelles can behave like flexible polymer chains with a length larger than the persistence length (see section 3.1.4). This kind of micellar structure is called a wormlike micelle. Therefore, a new category of surfactant self-assembly emerges.

A typical wormlike micelle is an elongated semi-flexible aggregate with a persistence length on the order of 400 Å, a total length up to a few micrometers and a diameter of a few nanometers.[40,43] The micellar aggregate behaves as a rigid rod at length scales shorter than its persistence length, while at length scales much longer than the persistence length, it behaves like a polymer chain (i.e. it can be modeled as a three dimensional random walk). However, if the scission energy is small enough, then the micellar chain can break and recombine.[40,41] So, while a polymer solution includes polymer molecules that have same lengths, a wormlike micellar solution contains dynamic aggregates of chains with different contour lengths.[40,41] It is sometimes called a living polymer for this reason. In the concentration regime above the overlap volume fraction Φ^* (equation 3.12), a network of entangled wormlike micelles formed inside a micellar solution. Dynamics of a wormlike micelle is thought to be similar to polymer dynamics, exhibiting curvilinear motion along a tube-like contour that is defined by the locus of its entanglements with other nearby wormlike micellar chains. This motion is called reptation.[43]

We mentioned in section 2.2.4 that the Cole-Cole diagram (i.e. G''/G_o versus G'/G_o) of a

Maxwellian fluid exhibits a semicircle of radius (1/2). Also, Maxwellian fluids show a mono-exponential stress relaxation function with a single relaxation time τ. In a wormlike micelle τ is defined as:

$$\tau = \sqrt{\tau_b \tau_R} \tag{3.33}$$

where τ_b is the time required for a micellar chain to break into two segments and τ_R is time required for the micellar chain to leave its tube-like contour.[40,41] Also, the breaking and recombination time τ_b is given in term of the average length of the micellar chain L

$$\tau_b = \frac{1}{k_b L} \tag{3.34}$$

where k_b is the rate constant for the breakage.[40,41]

At the low frequencies window of dynamic measurements (section 2.2.3), the wormlike micellar chains response to an applied stress by reptating out of their original tube-like contours. During the reptating process, each micellar chain in a wormlike micelle breaks and recombines many times. This is due to the fact that at low frequencies $\tau_b \ll \tau_R$. Based on that, no memory for the initial length and the position of a chain in the tube-like contour.[41] Therefore, the stress relaxation function is mono-exponential (equation 2.50). However, at high frequencies these wormlike micellar systems show a deviation from the Maxwellian model. In this regime, the breaking and recombination process is not the dominant relaxation mechanism. This is attributed to the existence of additional faster relaxation mechanisms such as Rouse and breathing relaxation mechanisms.[40] The Rouse relaxation mechanism is attributed to stretches that are experienced by micellar chains segments that are shorter than the entanglement length (i.e. the length of micellar chain segment between two entanglement points), while the breathing relaxation mechanism is attributed to the fluctuations in tube-like contours.[40] The crossover from Maxwellian model regime to Rouse regime takes place at a frequency value of the order of the inverse of the breaking and recombination time τ_b of micellar chains.

78

If the average length of micellar chains is not long enough, this causes an expected increase in τ_b (i.e. equation 3.34). This causes an increase in the ratio τ_b/τ_R. Under this circumstance, a wormlike micellar system shows deviation from Maxwellian behavior at low frequencies (Inset: figure 5.5a). In addition, the stress relaxation function exhibits multi-exponential behavior. Chapter 5 includes a thorough study for a wormlike micellar system that does not exhibit Maxwellian behavior at low frequencies.

Because of their distinctive and remarkable rheological behavior, wormlike micellar solutions have been a target of many theoretical and experimental research studies that are summarized in the introduction of chapter 5. A wormlike micellar solution shows viscoelastic properties similar to polymer solutions above the overlap concentrations, either in the regime at which the hydrodynamic interactions take place between the nearby micelles (i.e. the semidilute regime) or the regime at which the micelles start occupying the pervaded volumes of other nearby wormlike micelles (i.e. entanglement or concentrated regime). Moreover, wormlike micelles are used widely in many industrial and commercial applications such as drag reduction in fluid flow (enhancing smooth flow in pipes which provides fluids for heating and cooling purposes), detergents, and cleaners.[40,44,45] Therefore, complementary measurements are presented in chapter 5 that are incorporated to investigate the dynamics and the structure of a new wormlike micellar system. The chosen system is composed of a mixed zwitterionic TDPS surfactant and anionic SDS surfactant in brine solution. Zwitterionic surfactant aggregates are one step closer to the complexity of the (often zwitterionic) protein-lipid complexes in biophysical systems.

3.3.3 Proteins

Proteins are organic macromolecules which consist of a sequence or a linear array (i.e. unbranched) of chemical groups called amino acids which are covalently bonded to each other. These covalent bonds are called peptide bonds. An amino acid (figure 3.6) represents the building block in a

79

protein molecule. Its generic structure is composed of a carbon atom called the α carbon atom, which is covalently bonded to a hydrogen atom, carboxyl group (COO$^-$), amino group (NH$_3^+$), and side chain group (R group).[46]
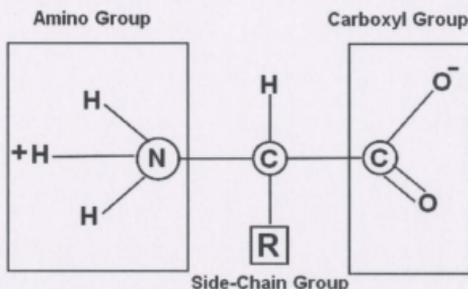
Figure 3.6: A schematic representation of an amino acid.

The variation in the chemical properties of different amino acid groups is characterized by the side chain group (R group) which can be nonpolar and hydrophobic, polar, or charged and hydrophilic. Different chemical structures of side chain groups create twenty different amino acid groups which are used to build proteins.

The structure of a protein is characterized through different levels: primary structure, secondary structure, tertiary structure, and quaternary structure. The primary structure represents the backbone or the linear array of amino acids (or polypeptide) which build up the protein molecule. So the number, the chemical composition of the side chain groups, and the sequential arrangement of the amino acid building blocks characterize the primary structure and determine the chemical properties of the protein molecule. The secondary structure represents the three dimensional shape of a protein segment. This shape can be affected by hydrogen bonds between nearby parts. For example, the hydrogen bond between N-H on the i-th amino acid and C=O chemical groups on the (i+4)-th amino acid in the protein chains in the amino acids of a protein chain gives rise to the

alpha-helical shape of a protein segment. Another category of secondary structure is the β-sheet.

The tertiary structure represents the three dimensional structure of the entire protein molecule, the orientation, and the arrangement of the protein side groups.[46] It includes the intramolecular interactions between α−helix and β-sheets segments on the same protein molecule. The intramolecular interactions in this structure category are non-covalent interactions such as ionic bonds, van der Waals bonds, hydrogen bonds, and hydrophobic interactions. According to this, each protein molecule has its unique three dimensional structure with a single well defined conformation of amino acids as well as side group orientations.

The van der Waals interaction (equation 3.35) dominates in non-polar molecules.[47] It is an attractive interaction that is attributed to the combination of the interaction between instantaneous electric dipole moments that results from electron cloud fluctuations in the molecule and the interaction between electric dipole moments in the molecules,

$$U(r) = -\frac{3}{4}\left(\frac{1}{4\pi\epsilon_o}\right)^2 \frac{\alpha^2}{r^6}\hbar\omega, \qquad (3.35)$$

where ϵ_o, α and $\hbar\omega$ are the dielectric constant of free space, the polarizability, and the ionization energy, respectively.

Another interaction which is dominant among non-polar molecules or non-polar segments of molecules is called the hydrophobic interaction.[47] This interaction was discussed in the introduction to section 3.3. The existence of non-polar side chains (hydrophobic amino acids residues) in the protein molecule drives the non-polar side chains to associate in order to minimize contact with water molecules in the aqueous environment.[47] Therefore, the hydrophobic interaction plays a crucial role to the stabilization of tertiary structure in proteins.

Lysozyme represents an example of a globular protein which contains both hydrophobic and hydrophilic amino acid groups. The globular shape of lysozyme in an aqueous solution is attributed to the tendency of amino acid units to arrange themselves in a special structure to minimize the

contact between hydrophobic groups and water molecules, and maximize the contact between hydrophilic segments and water molecules. The protein molecule has one configuration which reduces its free energy to the minimum value, this configuration is called the protein native state.

In addition, proteins such as lysozyme have an ability to associate into aggregates (dimers, trimers, or high-order aggregates) in an aqueous solution. Some studies have shown that the formation of protein clusters or aggregates are attributed to the combination between a short-range attraction and a long-range repulsion. The short-range attraction component has the $1/r^6$ distance dependent van der Waals attraction.[2,39] The long range interaction is sometimes represented by a screened Yukawa electrostatic repulsion[2,30,31,48]

$$U_Y(r) = A \frac{e^{-\kappa(r-r_o)}}{r} \qquad (3.36)$$

where r_o is the average diameter of a protein molecule that is represented as a hard sphere-like object, $A = \left((ze)^2/(4\pi\epsilon_r\epsilon_o(1 + \kappa r_o/2)^2)\right)$ represents the overall strength of the interaction and κ^{-1} is the Debye screening length,

$$\kappa^{-1} = \left(\frac{\epsilon_r\epsilon_o K_B T}{2n_o(ze)^2}\right)^{0.5} \qquad (3.37)$$

where ze is the charge of a protein molecule, ϵ_o and ϵ_r represent the permittivity of the vacuum and the relative permittivity of the solvent respectively.

From equation 3.37 it is clear that both temperature and the concentration of dissolved ions in solution play a crucial role in modifying the nature of the electrostatic interaction between protein molecules. Therefore, both temperature and ionic concentration can be used to control aggregate formation in a protein solution.[26,28] Many studies have revealed formation of protein aggregates and crystals. The study of equilibrium protein aggregates is the subject of chapter 5.

3.4 Co-authorship statement

All experimental work and the sample preparation were performed by the principle author Mr. Suliman Barhoum. The principle author did the data analysis after intellectual discussion with his supervisor Dr. Anand Yethiraj in the Department of Physics and Physical Oceanography at Memorial University of Newfoundland. Also, the principle author prepared drafts of the manuscripts for articles upon which chapters 4, 5, and 6 are based. Dr. Ronaldo Castillo of Instituto de Física, Universidad Nacional Autónoma de México in Mexico contributed by suggesting the experimental system and in editing and constructing the manuscript upon which chapter 5 is based. Dr. Valerie Booth of Department of Biochemistry, Memorial University of Newfoundland in Canada contributed by providing us with the peptide, discussing the experimental plan and results, and in editing and constructing the manuscript upon which chapter 7 is based.

Bibliography

[1] Ian W. Hamley. *Introduction to Soft Matter-Revised Edition Synthetic and Biological Self-Assembling Materials*. John Wiley & Sons Ltd, Chichester, 1st edition, 2007.

[2] Richard. A. L. Jones. *Soft Condensed Matter*. Oxford University Press Inc, New York, 1st edition, 2002.

[3] Deborah K. Wilkins, Shaun B. Grimshaw, Veronique Receveur, Christopher M. Dobson, Jonathan A. Jones, and Lorna J. Smith. Hydrodynamic radii of native and denatured proteins measured by pulse field gradient nmr techniques. *The Journal of Biochemistry*, 38:16424–16431, 1999.

[4] Bruce J. Berne and Robert Pecora. *Dynamic Light Scattering With Application to Chemistry, Biology, and Physics*. John Wiley & Sons Inc, New York, 1st edition, 1976.

[5] L. A. Feigin and Dimitrii Ivanovich Svergun. *Structure Analysis by Small-Angle X-Ray and Neutron Scattering*. Plenum Press, New York, 1st edition, 1987.

[6] Otto Glatter and Otto Kratky. *Small-Angle X-ray Scattering*. Academic press, London, 1st edition, 1982.

[7] Michael Rubinstein and Ralph H. Colby. *Polymer Physics*. Oxford University Press, New York, 1st edition, 2003.

[8] Albert Einstein. Zur theorie der brownschen bewegung. *Annalen der Physik*, 17:549–550, 1906.

[9] William Sutherland. A dynamical theory of diffusion for non-electrolytes and the molecular mass of albumin. *Philosophical Magazine and Journal of Science*, 54:781–785, 1905.

[10] Robert J. Hunter. *Foundations of Colloid Science*. Oxford University Press Inc, New York, 2nd edition, 2001.

[11] Magdaleno Medina-Noyola. Long-time self-diffusion in concentrated colloidal dispersions. *Physical Review Letters*, 60:2705, 1988.

[12] Jining Han and Judith Herzfeld. Macromolecular diffusion in crowded solutions. *Biophysical Journal*, 65:1155–1161, 1993.

[13] Michio Tokuyama and Irwin Oppenheim. Dynamics of hard-sphere suspensions. *Physical Review E*, 50:R16–R19, 1994.

[14] William S. Price, Fumihiko Tsuchiya, and Yoji Arata. Lysozyme aggregation and solution properties studied using PGSE NMR diffusion measurements. *Journal of the American Chemical Society*, 121:11503–11512, 1999.

[15] V. V. Krishnan. Determination of oligomeric state of proteins in solution from pulsed-field-gradient self-diffusion coefficient measurements. a comparison of experimental, theoretical, and hard-sphere approximated values. *Journal of Magnetic Resonance*, 124:468–473, 1997.

[16] Wilson Poon and David Andelman. *Soft Condensed Matter Physics in Molecular and Cell Biology*. CRC Press, New York London, 1st edition, 2006.

[17] Prince E. Rouse. A theory of the linear viscoelastic properties of dilute solutions of coiling polymers. *The Journal of Chemical Physics*, 21:1272–1280, 1953.

[18] Bruno H. Zimm. Dynamics of polymer molecules in dilute solution: Viscoelasticity, flow birefringence and dielectric loss. *The Journal of Chemical Physics*, 24:269–278, 1956.

[19] Mohamed Daoud and Claudine E. Williams. *Soft Matter Physics*. Springer, Germany, 1st edition, 1999.

[20] Anthony D. Dinsmore, Paul L. Dubin, and Gregory M. Grason. Clustering in complex fluids. *The Journal of Physical Chemistry B*, 115:7173–7174, 2011.

[21] Suliman Barhoum and Anand Yethiraj. NMR detection of an equilibrium phase consisting of monomers and clusters in concentrated lysozyme solutions. *The Journal of Physical Chemistry B*, 114:17062–17067, 2010.

[22] Frederic Cardinaux, Anna Stradner, Peter Schurtenberger, Francesco Sciortino, and Emanuela Zaccarelli. Cluster-driven dynamical arrest in concentrated lysozyme solutions. *The Journal of Physical Chemistry B*, 115:7227–7237, 2011.

[23] Nicolas Meilhac and Nicolas Destainville. Clusters of proteins in biomembranes: Insights into the roles of interaction potential shapes and of protein diversity. *The Journal of Physical Chemistry B*, 115:71907199, 2011.

[24] Annalisa Fierro, Tiziana Abete, Antonio Coniglio, and Antonio de Candia. Clusters in colloidal systems. *The Journal of Physical Chemistry B*, 115:72817287, 2011.

[25] Jan Groenewold and Willem Kegel. Colloidal cluster phases, gelation and nuclear matter. *Journal of Physics: Condensed Matter*, 16:S4877–S4886, 2004.

[26] Anna Stradner, Helen Sedgwick, Frederic Cardinaux, Wilson C. K. Poon, Stefan U. Egelhaaf, and Peter Schurtenberger. Equilibrium cluster formation in concentrated protein solutions and colloids. *Nature*, 432:492–495, 2004.

[27] Anuj Shukla, Efstratios Mylonas, Emanuela Di Cola, Stephanie Finet, Peter Timmins, Theyencheri Narayanan, and Dmitri I. Svergun. Absence of equilibrium cluster phase in concentrated lysozyme solutions. *Proceedings of the National Academy of Sciences*, 105:5075–5080, 2008.

[28] Anna Stradner, Frederic Cardinaux, and Peter Schurtenberger. A small-angle scattering study on equilibrium clusters in lysozyme solutions. *The Journal of Physical Chemistry B*, 110:21222–21231, 2006.

[29] Francesco Sciortino, Stefano Mossa, Emanuela Zaccarelli, and Piero Tartaglia. Equilibrium cluster phases and low-density arrested disordered states: The role of short- range attraction and long-range repulsion. *Physical Review Letters*, 93:1–4, 2004.

[30] Frederic Cardinaux, Anna Stradner, Peter Schurtenberger, Francesco Sciortino, and Emanuela Zaccarelli. Modeling equilibrium clusters in lysozyme solutions. *A Letters Journal Exploring The Frontiers of Physics*, 77:1–5, 2007.

[31] Fredrik Carlsson, Martin Malmsten, and Per Linse. Monte carlo simulations of lysozyme self-association in aqueous solution. *The Journal of Physical Chemistry B*, 105:12189–12195, 2001.

[32] Lionel Porcar, Peter Falus, Wei-Ren Chen, Antonio Faraone, Emiliano Fratini, Kunlun Hong, Piero Baglioni, and Yun Liu. Formation of the dynamic clusters in concentrated lysozyme protein solutions. *The Journal of Physical Chemistry Letters*, 1:126129, 2009.

[33] Jaroslaw Poznanski, Jedrzej Szymanski, Teresa Basinska, Stanislaw Slomkowski, and Wojciech Zielenkiewicz. Aggregation of aqueous lysozyme solutions followed by dynamic light scattering and ^{1}H NMR spectroscopy. *Journal of Molecular Liquids*, 121:21–26, 2005.

[34] Yun Liu, Emiliano Fratini, Piero Baglioni, Wei-Ren Chen, and Sow-Hsin Chen. Effective long-range attraction between protein molecules in solutions studied by small angle neutron scattering. *Physical Review Letters*, 95(118102):1–4, 2005.

[35] N. Niimura, Y. Minezaki, M. Ataka, and T. Katsura. Aggregation in supersaturated lysozyme solution studied by time-resolved small angle neutron scattering. *Journal of Crystal Growth*, 154:136–144, 1995.

[36] William S. Price, Fumihiko Tsuchiya, and Yoji Arata. Time dependence of aggregation in crystallizing lysozyme solutions probed using NMR self-diffusion measurements. *Biophysical Journal*, 80:15851590, 2001.

[37] Elena Ilyina, Vikram Roongta, Hong Pan, Clare Woodward, and Kevin H. Mayo. A pulsed-field gradient NMR study of bovine pancreatic trypsin inhibitor self-association. *The Journal of Biochemistry*, 36:3383–3388, 1997.

[38] Sean R. McGuffee, , and Adrian H. Elcock. Atomically detailed simulations of concentrated protein solutions: The effects of salt, pH, point mutations, and protein concentration in simulations of 1000-molecule systems. *Journal of the American Chemical Society*, 128:12098–12110, 2006.

[39] Jacob Israelachvili. *Intermolecular and Surface Forces*. Academic Press Limited, London, 2nd edition, 1991.

[40] Cecile A. Dreiss. Wormlike micelles: where do we stand? Recent developments, linear rheology and scattering techniques. *Soft Matter*, 3:956–970, 2007.

[41] Mike E. Cates and Sauveur-Jean Candau. Statics and dynamics of worm-like surfactant micelles. *Journal of Physics: Condensed Matter*, 2:6869–6892, 1990.

[42] Johan T. Padding, Wim J. Briels, Mikhail R. Stukan, and Edo S. Boek. Review of multi-scale particulate simulation of the rheology of wormlike micellar fluids. *Soft Matter*, 5:4367–4375, 2009.

[43] Jean-Franois Berret. *Rheology of wormlike micelles: equilibrium properties and shear banding transitions, in: R.G. Weiss, P. Terech (Eds.), Molecular Gels: Materials with Self-Assembled Fibrillar Networks*. Springer, The Netherlands, 1st edition, 2006.

[44] Jiang Yang. Viscoelastic wormlike micelles and their applications. *Current Opinion in Colloid & Interface Science*, 7:276–281, 2002.

[45] Raoul Zana and Eric W. Kaler. *Giant Micelles. Properties and Applications*. Taylor & Francis Group, New York, 1st edition, 2007.

[46] Ian M. Rosenberg. *Protein Analysis and Purification*. Birkhauser, Boston, 1st edition, 1996.

[47] Andrey Karshikoff. *Non-Covalent Interactions in Proteins*. Imperial College Press, New York, 1st edition, 2006.

[48] Fajun Zhang, Maximilian W. A. Skoda, Robert M. J. Jacobs, Richard A. Martin, Christopher M. Martin, and Frank Schreiber. Protein interactions studied by saxs: Effect of ionic strength and protein concentration for bsa in aqueous solutions. *The Journal of Physical Chemistry B*, 111:251–259, 2007.

[42] Johan T. Padding, Wim J. Briels, Mikhail R. Stukan, and Edo S. Boek. Review of multi-scale particulate simulation of the rheology of wormlike micellar fluids. *Soft Matter*, 5:4367–4375, 2009.

[43] Jean-Franois Berret. *Rheology of wormlike micelles: equilibrium properties and shear banding transitions, in: R.G. Weiss, P. Terech (Eds.), Molecular Gels: Materials with Self-Assembled Fibrillar Networks*. Springer, The Netherlands, 1st edition, 2006.

[44] Jiang Yang. Viscoelastic wormlike micelles and their applications. *Current Opinion in Colloid & Interface Science*, 7:276–281, 2002.

[45] Raoul Zana and Eric W. Kaler. *Giant Micelles. Properties and Applications*. Taylor & Francis Group, New York, 1st edition, 2007.

[46] Ian M. Rosenberg. *Protein Analysis and Purification*. Birkhauser, Boston, 1st edition, 1996.

[47] Andrey Karshikoff. *Non-Covalent Interactions in Proteins*. Imperial College Press, New York, 1st edition, 2006.

[48] Fajun Zhang, Maximilian W. A. Skoda, Robert M. J. Jacobs, Richard A. Martin, Christopher M. Martin, and Frank Schreiber. Protein interactions studied by saxs: Effect of ionic strength and protein concentration for bsa in aqueous solutions. *The Journal of Physical Chemistry B*, 111:251–259, 2007.

Chapter 4

An NMR Study of Macromolecular Aggregation in a Model Polymer-Surfactant Solution

4.1 Abstract

A model complex-forming nonionic polymer-anionic surfactant system in aqueous solution has been studied at different surfactant concentrations. Using pulsed-field-gradient diffusion NMR spectroscopy, we obtain the self-diffusion coefficients of poly(ethylene glycol) (PEO) and sodium dodecyl sulfate (SDS) simultaneously and as a function of SDS concentration. In addition, we obtain NMR relaxation rates and chemical shifts as a function of SDS concentration. Within the context of a simple model, our experimental results yield the onset of aggregation of SDS on PEO

chains (CAC=3.5 mM), a crossover concentration (C_2=60 mM) which signals a sharp change in relaxation behavior, as well as an increase in free surfactant concentration, and a critical concentration (C_m=145 mM) which signals a distinct change in diffusion behavior and a crossover to a solution containing free micelles. C_m also marks the concentration above which obstruction effects are definitely important. In addition, we obtain the concentration of SDS in monomeric form and in the form of free micelles, as well as the average number of SDS molecules in a PEO-SDS aggregate (N_{Aggr}). Taken together, our results suggest continuous changes in the aggregation phenomenon over much of the concentration but with three distinct concentrations that signal changes in the nature of the aggregates.[1]

4.2   Introduction

Multicomponent solutions consisting of polymers, surfactants, proteins, and other macromolecules are common to many biological systems as well as cosmetic and pharmaceutical preparations.[2–4] The understanding of the nature of macromolecular aggregates and complexes is consequently of great technological relevance. The poly (ethylene oxide) (PEO)-sodium dodecyl sulfate (SDS) polymer-surfactant system in aqueous solution is a useful model system for the study of macromolecular complex formation.

A quantitative study of complex formation in the PEO/SDS system is a starting point to study more complex biological systems with crowded environments, e.g., cellular environments composed of different kinds of macromolecules at high concentration.[5–7] Diffusion processes in cells are likely to be strongly influenced by macromolecular crowding effects.[8,9]

In spite of the wealth of knowledge about the PEO-SDS system[4,10,11](summarized in Sec. 4.3), important questions have only partial answers. Are SDS conformations in the surfactant-polymer aggregate quantitatively different from those in the SDS micelle? Where in the aggregation regime do free micelles also form (and is there a distinct transition)? When do crowding effects become

important? The partitioning of the SDS concentration between the monomeric state, the surfactant-polymer aggregate, and free micelles as a function of the total SDS concentration remains unquantified. In this study we use NMR spectroscopy to address these questions with high experimental precision.

4.3 Background

The interaction between PEO and SDS molecules in aqueous solution has been studied by many researchers.[12-20] We summarize below briefly what is known via a variety of techniques[12,13,15-23] including NMR relaxometry[12,24,25] and diffusometry.[11,13,19,20,26]

1. The critical micelle aggregation (CMC) is a critical concentration above which SDS micelles begin to form in a pure surfactant solution.[27,28] SDS micelles have been shown in a neutron scattering study to be best fit to an oblate ellipsoid shape (or a disk-like shape) at $C^{SDS} \approx 39$ mM, with half axes a = 12 Å and b = 20.3 Å.[29]

2. The critical concentration above which PEO-SDS aggregates begin to form[13,16,19,21,26] is called the critical aggregation concentration (CAC).

3. There is a second higher SDS concentration termed as C_2 that signals a change in the nature of the PEO-SDS aggregates. This has been identified either as the concentration where free micelles coexist with PEO-SDS aggregates[14-16] or the concentration that signals the saturation in the number of SDS molecules N_{Aggr} that aggregate on a PEO molecule[14,30] (the notation C_m has been employed for the former to distinguish it from C_2).[18] Pulsed gradient spin echo NMR spectroscopy has been used[11] to measure the self diffusion coefficient of PEO molecules at different SDS concentrations: Progressive changes in the values of the PEO diffusion coefficients with increasing concentrations were observed, attributed to the aggregation of SDS molecules on PEO molecules, the saturation of the polymer molecules

with surfactant, and the transition of SDS micelles from sphere to rod-like micelles, respectively.[25]

4. Finally, a non-monotonic viscosity maximum has been observed at SDS concentration near or above C_2.[24,31] While small angle neutron scattering has provided strong evidence for the SDS aggregating on the polymer in the form of micelle subunits,[14] but the nature of the surfactant-polymer interaction is not yet clear.

Table 4.1: Critical aggregation concentration values for PEO/SDS system[12,13,17–20] using NMR, conductivity measurements, and Isothermal Titration Calorimetry (ITC).

Experiment	PEO M_w(g/mole)	PEO Conc. %w/v	T(°C)	CAC (mM)	C_2(mM)
NMR[12]	300,000	≈ 0.2	20	4.5	-
Conductivity[17]	20,000	0.2	25	4.5	-
ITC[18]	20,000	≈ 0.1	25	≈ 4.4	-
NMR[13]	20,000	≈ 0.2	25	≈ 5.7	15-25
NMR[19]	4000	0.2	25	3.3	-
NMR[20]	20,000	≈ 0.2	25	4.6	-

Table 4.1 shows the values of critical aggregation concentration (CAC) for the PEO/SDS system in aqueous solution that have been measured using different techniques. For the purpose of comparison, we converted some CAC concentration values from mass percentage (weight percent) to molar concentration (C) using:[20] $C = \frac{\rho_{D_2O}}{M_s} \frac{wt\%}{100 - wt\%}$ where ρ_{D_2O} and M_s are the density of deuterium oxide in (g/L) and the molecular mass of surfactant, respectively. There is a spread of about 30% in both the CAC and C_2 values reported.

NMR spectroscopy has been used as a powerful technique to study macromolecular dynamics[32] in polymer-surfactant systems (and the PEO-SDS system in particular) since it can report on

93

molecular motion inside aqueous solutions via the longitudinal relaxation time T_1 and the transverse relaxation time T_2.[12,33] In addition, pulsed-field-gradient diffusion NMR spectroscopy is used to measure the molecular self-diffusion coefficient.[34,35] All of these physical quantities will change due to the interaction between molecules, molecular aggregation, and micellization.[36]

A key feature of the current study is the simultaneous measurement of diffusion coefficient of SDS, PEO, and DOH components, in addition to relaxation rates, in samples that span the entire concentration range from below the CAC to just below the micellization. The simultaneous measurement of diffusion coefficients of all components allows us to pinpoint the different regimes quantitatively, to establish regimes of absolute validity of a simple model, and to make a strong quantitative statement in the same system about the CAC, the saturation concentration C_2, and the micellization concentration C_m.

4.4 Experimental

Poly(ethyleneoxide) (PEO) with 20,000 average molecular mass and sodium dodecyl sulfate (SDS, > 99% purity) with 288.38 average molecular mass were purchased from Sigma-Aldrich Canada and were used as received without purification. The PEO chain in the study has ≈ 450 monomers (each of length ≈ 0.44 nm). The Kuhn length $\ell_k \approx 1.8$ nm.[37] Deuterium oxide D_2O with 99.9% isotopic purity was purchased from Cambridge Isotope Laboratories.

We prepared three different solutions: PEO(0.5%w/v)/D_2O, SDS(455mM)/PEO(0.5%w /v)/D_2O, and SDS(794mM)/PEO(0.5%w/v)/D_2O. Samples with SDS concentration below 455 mM were prepared by mixing PEO(0.5%w/v)/D_2O stock solution with SDS(455mM)/PEO(0.5%w /v)/D_2O stock solution, while we used SDS(794mM)/PEO(0.5% w/v)/D_2O stock solution to prepare the samples with SDS concentrations larger than 455 mM.

The one dimensional (1D) proton NMR spectrum has been observed for different species in all samples at a resonance frequency of 600 MHz on a Bruker Avance II spectrometer.
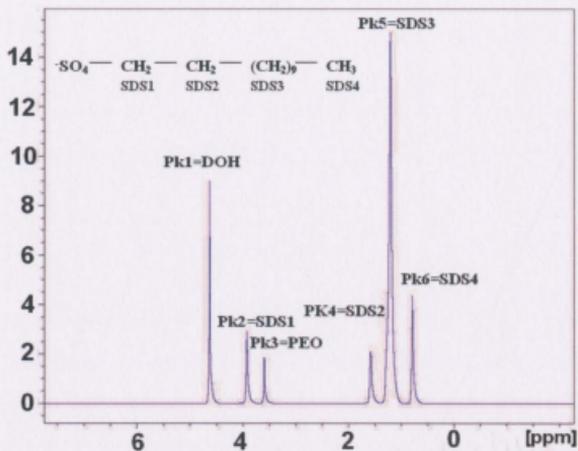
Figure 4.1: One-dimensional ^1H – NMR spectrum for PEO(0.5% w/v)/SDS(455 mM)/D_2O sample at a sample temperature 298 K. Inset: the chemical formula of SDS molecule.

Figure 4.1 shows six well-separated peak related to this system. Peak 1 is the DOH peak created due to the quick exchange of protons between D_2O and H_2O molecules in solution. Peaks 2 and 4-6 are associated with protons of sodium dodecyl sulfate (SDS) molecule SDS1, SDS2, SDS3, and SDS4 as shown in figure 4.1. Peak 3 is associated with protons of the Poly(ethylene oxide) molecule. The 1D spectrum of the SDS/D_2O system similarly includes only five peak regions because it is polymer free. All NMR experiments were performed at T = 298 K.

The self-diffusion measurements were carried out in a diffusion probe (Diff 30) and with maximum field gradient (1800 G/cm). Diffusion was measured with a pulsed field gradient stimulated-echo sequence[34] with (almost square) trapezoidal gradient pulses. The diffusion coefficient of a molecule in aqueous solution is obtained from the attenuation of the signal according to the equation:[34]

$$\ln\left(\frac{S(k)}{S(0)}\right) = -Dk \qquad (4.1)$$

where S(k) is the "intensity" of the signal (the integration of the relevant peak region) in the presence of field gradient pulse, S(0) is the intensity of the signal in the absence of field gradient pulse, $k = (\gamma \delta g)^2 (\Delta - \delta/3)$ is a generalized gradient strength parameter, $\gamma = \gamma^H = 2.6571 \times 10^8$ $T^{-1}.s^{-1}$ is the gyromagnetic ratio of the ^1H nucleus, $\delta = 2$ ms is the duration of the field gradient pulse, $\Delta = 100$ ms is the time period between the two field gradient pulses, and g is the amplitude of the field gradient pulse.

Figure 4.2 shows the signal attenuation and the self-diffusion coefficients for five peaks corresponding to Pk2, Pk4, Pk5, Pk6 (SDS1, SDS2, SDS3, SDS4) and Pk3 (PEO). It is clear from figure 4.2 that the signal attenuation is mono-exponential for all peaks over the whole range of SDS concentration. The values of the self-diffusion coefficients D for different molecules were calculated from the slopes of the curves in figure 4.2. The gradient pulse duration was $\delta = 2$ ms, while the time period between the gradient pulses was $\Delta = 100$ ms. The gradient pulse strength g was increased in a linear sequence of 16 steps up to 480 G/cm for PEO diffusion while for SDS
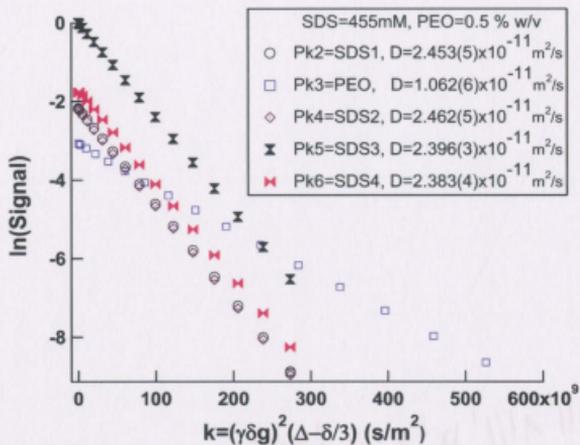
Figure 4.2: The attenuation of the signal $S(k)/S(0)$ on a log scale versus $k = (\gamma \delta g)^2 (\Delta - \delta/3)$ for PEO (0.5% w/v)/SDS (455 mM)/D_2O sample with $\delta = 2 \times 10^{-3}$s, $\Delta = 100 \times 10^{-3}$s.

diffusion g was increased in a linear sequence of 16 steps up to 350 G/cm.

The relaxation measurements were performed using a Bruker high resolution (TXI) probe. The inversion recovery technique was used to measure T_1, eight time delays were used to measure T_1 for the PEO peak region, and the intensity data were fitted to the equation $I(t) = I_o(1 - 2\exp(\frac{-t}{T_1}))$.[38] A $(\frac{\pi}{2})_x - t/2 - (\pi)_x - t/2 -$ acquire spin echo experiment was used to measure T_2, 16 values, at delay times t, of the integrated intensity of the PEO peak were taken to measure T_2 and the intensity data were fitted to the equation $I(t) = I_o \exp(\frac{-t}{T_2})$.[38]

4.5   Results and Discussion

4.5.1   Chemical shift measurements

Chemical shift studies are a well-established method to characterize critical concentrations.[30, 39] Figure 4.3a shows the variation in the chemical shift difference between the protons of SDS1 and SDS4 chemical groups for each SDS/D_2O and PEO(0.5% w/v)/SDS/D_2O sample over the whole range of SDS concentration. The chemical shift difference is sensitive to the average local environment of the SDS molecule. Assuming fast chemical exchange, the observed chemical shift is a weighted average of the SDS in free and in micellar form. Below the CMC/CAC this results (see Gao, Wasilyshen and Kwak,[39] equation 1, and Cui et al[28]) in a reciprocal relationship between the observed chemical shift and the total SDS concentration. In particular,

$$\delta_{Obs} = \delta_{free}, \qquad\qquad C^{SDS} \leq C^*$$

$$\delta_{Obs} = \left(\frac{C^*}{C^{SDS}}\right)\delta_{free} + \left(1 - \frac{C^*}{C^{SDS}}\right)\delta^*, \qquad C^{SDS} > C^* \qquad (4.2)$$

where: C^* denotes CMC or CAC and δ^* denotes $\delta_{micelle}$ or $\delta_{aggregate}$ for SDS/D_2O or PEO(0.5% w/v)/SDS/D_2O, respectively.

By linearly fitting the plot of the chemical shift difference against $1/C^{SDS}$ using the piece-wise function in Equation 4.2 (figure 4.3a, inset), we obtained the critical micelle concentration
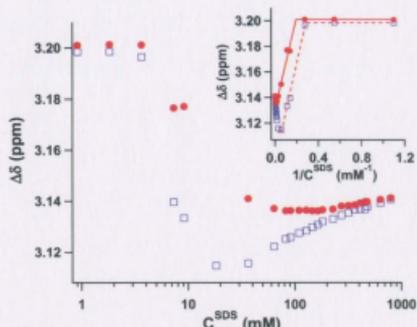
(a)
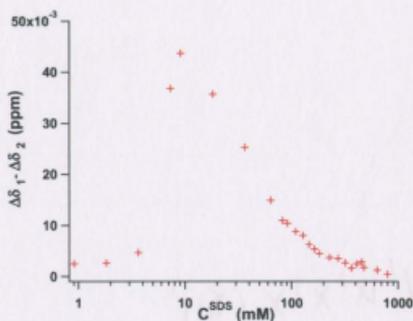
(b)

Figure 4.3: (a) Chemical shift difference ($\Delta\delta$) between the protons of SDS1 and SDS4 for each PEO(0.5% w/v)/SDS/D_2O (opened squares) and SDS/D_2O (solid circles) sample versus SDS concentration. Inset: $\Delta\delta$ versus reciprocals of SDS concentrations and (b) The difference in the value of $\Delta\delta$ between SDS/D_2O samples ($\Delta\delta_1$) and PEO(0.5% w/v)/SDS/D_2O samples ($\Delta\delta_2$) versus SDS concentration. The difference between PEO/SDS and pure SDS solutions is greatest between ≈ 4 and 100 mM.

[CMC=5.1(4) mM] and the critical aggregation concentration [CAC=3.5(1) mM].

The SDS1 group is more susceptible to the extra-micellar environment than SDS4 group. A lower $\Delta\delta$ (e.g., figure 4.3a) indicates better shielding of the SDS1 group. This indicates that for a fixed C^{SDS}, the SDS1 group is better shielded in the presence of PEO.

Figure 4.3b shows the variation in the difference in the value of $\Delta\delta_1$ for SDS/D_2O samples and the corresponding $\Delta\delta_2$ for PEO(0.5% w/v)/SDS/D_2O samples. The difference ($\Delta\delta_1 - \Delta\delta_2$) reports on the effect of PEO on the local environment of SDS at any given concentration. This difference is smallest at very low (< 3mM) and at very high (> 400mM) SDS concentration and largest at 10mM.

4.5.2 Self-diffusion measurements

We have prepared 20 samples each of SDS/D_2O and SDS/PEO/D_2O with constant PEO concentration of 0.5% w/v at different SDS concentrations (C^{SDS}).

Figure 4.4a shows the self-diffusion coefficient of SDS in a solution of SDS/D_2O (no polymer). For C^{SDS} < 100mM we can fit the self-diffusion coefficient curve of SDS in SDS/D_2O solution, the model used is described in the discussion. From this fit the value of CMC agrees well with the value obtained from the chemical shift measurements [e.g. figure 4.3a].

Figure 4.5a(a) shows the self-diffusion coefficient of SDS, PEO, and DOH in SDS(794mM)/PEO (0.5%w/v)/D_2O. The self-diffusion coefficient of SDS in SDS/PEO/D_2O remains constant up to about C^{SDS} =3.5 mM. On the other hand, the self-diffusion coefficient curve of PEO begins to exhibit a noticeable decrease only at a higher value of SDS concentration ($\approx$ 10 mM). This behavior is consistent with SDS molecules associating with PEO. The effect of this association should affect the dynamics of the smaller SDS molecule more strongly than it affects much larger polymer chains.[20] Upon increasing the SDS concentration, the diffusion coefficient of both PEO and SDS decreases sharply for C^{SDS} < 100 mM. For C^{SDS} > 100 mM, the SDS and PEO diffusion coeffi-

(a)

$C^{SDS} < CMC$ CMC $C^{SDS} > CMC$
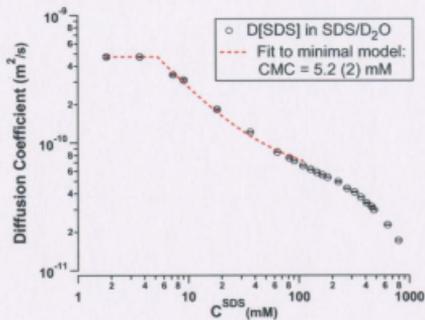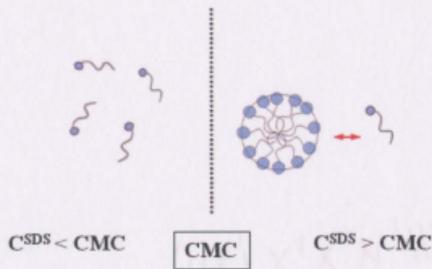
(b)

Figure 4.4: (a) SDS self-diffusion coefficient in SDS/D_2O versus SDS concentration. Error bars smaller than the symbol size. The fit to the minimal model breaks down above $\approx$ 100 mM due to obstruction effects (see text) and (b) schematic diagram for the partitioning of SDS molecules in SDS/D_2O. Monomers for $C^{SDS} < CMC$ and micelles and monomers for $CMC < C^{SDS}$.
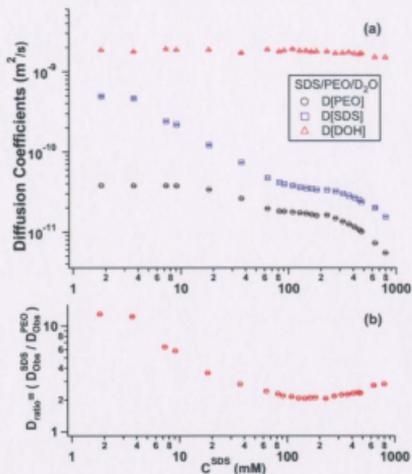
(a)
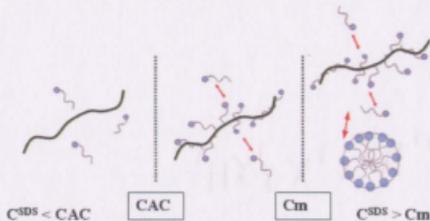
(b)

Figure 4.5: (a) Self-diffusion coefficient of PEO, SDS, and DOH in PEO(0.5% w/v)/SDS/D$_2$O versus SDS concentration (b) Ratio of SDS self-diffusion coefficient (D$_{Obs}^{SDS}$) to PEO self-diffusion coefficient (D$_{Obs}^{PEO}$). Error bars smaller than the symbol size and (c) schematic diagram for the partitioning of SDS molecules in PEO(0.5% w/v)/SDS/D$_2$O. Monomers for C^{SDS} < CAC, aggregates and monomers for CAC < C^{SDS} < Cm, and micelles, aggregares and monomers for Cm < C^{SDS}.

cients show a slower functional dependence on SDS concentration, and both curves in this regime have a remarkably similar shape (the ratio of observed SDS and PEO diffusion coefficients is not constant above 100 mM, but the variation is much weaker).

4.5.3 Relaxation measurements

According to the two-step model for relaxation in surfactant systems,[33,40–42] both the proton longitudinal relaxation rate R_1 and the transverse relaxation rate R_2 at different SDS concentrations are sensitive to fast local motions (˜free state˜) as well as slower aggregate motions (˜aggregate state˜). The difference $\Delta R = R_2 - R_1$ reports[42] on the slower (aggregate) motions.

Longitudinal T_1 and transverse T_2 relaxation measurements were made for the PEO peak at different SDS concentration. Figure 4.6 shows the variation of proton longitudinal relaxation rates $R_1 = 1/T_1$ (e.g., figure 4.6a), transverse relaxation rates $R_2 = 1/T_2$ (e.g., figure 4.6b), and the difference $\Delta R = R_2 - R_1$ (e.g., figure 4.6c) for PEO molecule at different SDS concentrations.

The relaxation rates measurements share a characteristic of a plateau above 60 mM, which coincides roughly with what we observe from the diffusion measurements. It represents an onset of the regime at which PEO chains saturate with SDS molecules. As has been noted before[42] the interpretation of NMR relaxation data is somewhat more involved than that of NMR diffusion data. We thus use the polymer relaxation rate measurements only as independent confirmation of the diffusometry results.

4.5.4 Discussion

We begin by discussing the chemical shift results. Below the CAC and CMC respectively, the chemical shift difference between the SDS4 and SDS1 group (representing difference in shielding between the group least and most proximate to the SO_4^- ion) is ≈ 3.2 ppm for both pure SDS and the SDS/PEO system. At a given C^{SDS}, the difference $\Delta\delta_1 - \Delta\delta_2$ represents the difference in the
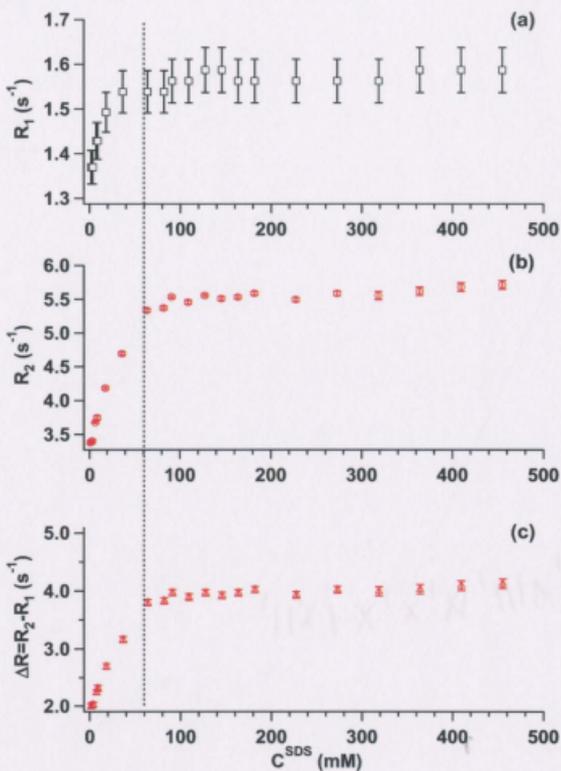
Figure 4.6: (a) Proton longitudinal relaxation rates R_1, (b) Transverse relaxation rates R_2 and (c) The difference $\Delta R = R_2 - R_1$ for PEO versus SDS concentration.

chemical environment due solely to the presence of the polymer. The difference is maximum at about 10 mM and decreases continuously for large C^{SDS}.

Next we discuss the diffusion results, beginning with the most dilute samples. From the SDS diffusion at the lowest SDS concentration (e.g. figure 4.5a and figure 4.4a), we note no difference here due to the presence of PEO. We estimate the corresponding hydrodynamic radius R_H/ radius of gyration R_G using values of the SDS and PEO diffusion coefficients at the lowest SDS concentration and the relevant forms of the Sutherland-Stokes-Einstein equation:[20]

$$R_H = \frac{K_B T}{6 \pi \eta D}, \; R_G = \frac{R_H}{0.7},$$ (4.3)

where K_B is Boltzmann's constant, T is the absolute temperature, and η is the solvent viscosity ($\eta_{D_2O} \approx 1.1$ mPa.s). For the SDS molecule this yields a hydrodynamic radius R_H is $\approx 4.01(3)$ Å. This is comparable to the hydrodynamic radius of 3.9 Å of an all-trans N = 12 carbon chain. The hydrodynamic radius is defined as $\frac{1}{R_H} = \frac{1}{N^2} \sum_{i,j=1, i \neq j}^{N} \left\langle \frac{1}{r_{ij}} \right\rangle$, where r_{ij} is the distance between sites i and j on the chain, e.g., see Yethiraj.[43] We also obtain the radius of gyration of the PEO molecule R_G is $\approx 7.43(1)$ nm. This agrees with the calculated value in the previous studies.[20]

The concentration of free surfactants above the CMC in SDS/D_2O solutions is expected to be constant ($C_{free}^{SDS} = $ CMC), while below the CMC concentration of free surfactants equals the total concentration of surfactants, $C_{free}^{SDS} = C^{SDS}$. The standard minimal model for pure surfactant systems is thus

$$D_{Obs}^{SDS} = D_{free}^{SDS}, \qquad\qquad\qquad C^{SDS} \leq CMC,$$

$$D_{Obs}^{SDS} = \left(\frac{CMC}{C^{SDS}} \right) D_{free}^{SDS} + \left(1 - \frac{CMC}{C^{SDS}} \right) D_{micelle}^{SDS}, \qquad C^{SDS} > CMC.$$ (4.4)

We assume that $D_{micelle}^{SDS}$ is constant for small enough SDS concentrations. Fitting to the above model we obtain a good fit for $C^{SDS} < 100$mM (e.g., figure 4.4a), yielding the following parameters: $D_{free}^{SDS} = 4.7(1) \times 10^{-10}$ m²/s, $D_{micelle}^{SDS} = 6.0(9) \times 10^{-11}$ m²/s, and CMC = 5.2(2) mM. The CMC thus obtained is consistent with the value obtained from the chemical shift results (e.g.,

figure 4.3a).

For surfactant-polymer aggregates, the situation is more complicated because aggregate size is expected to change a lot. Because the pulsed-field-gradient signal attenuation is mono-exponential, we conclude that the exchange of SDS molecules between the SDS/PEO in aggregates and in free solution must be very rapid on the NMR time scale. Thus, we postulate a minimal two species: free SDS and SDS in an aggregate) model: that the observed self-diffusion coefficients for SDS is a linear combination of the self-diffusion coefficient of the free molecules in bulk solution and that of the bound molecules associated with the complexes,[20, 26]

$$D_{Obs}^{SDS} = f\,D_{free}^{SDS} + (1-f)\,D_{Aggregate}^{SDS}, \tag{4.5}$$

where f is the fraction of free surfactant in the monomer state in the aqueous solution, D_{free}^{SDS} and $D_{Aggregate}^{SDS}$ are the self-diffusion coefficient of free SDS molecules (free ``monomers´´ in the bulk solution) and the SDS species associated with the polymer, respectively. Since we know that there is unlikely to be free PEO, we assume that $D_{Aggregate}^{SDS}$ in equation 4.5 is identical to the observed PEO diffusion coefficient D_{Obs}^{PEO}

$$D_{Obs}^{SDS} = f\,D_{free}^{SDS} + (1-f)\,D_{Obs}^{PEO}. \tag{4.6}$$

In the intermediate ($C^{SDS} > 100$ mM) regime, we note that the functional form of the SDS and the PEO diffusion coefficients are remarkably similar (e.g., figure 4.5aa). However a close look at the ratio $D_{Obs}^{SDS}/D_{Obs}^{PEO}$ (e.g., figure 4.5ab) shows a minimum just above 100 mM, and then a small steady increase. Using equation 4.6 we calculate the SDS free fraction over the entire range of SDS concentration. This is shown in figure 4.7.

We can see clearly from figure 4.7 that the fraction of free SDS in the bulk solution starts decreasing rapidly at the critical aggregation concentration up to ≈ 100 mM where about 4% of free SDS is available in the bulk solution. At the highest SDS concentration (where a transition to rod-like micelles is thought to take place) the free SDS fraction is $f \approx 2\%$. In addition, the functional

106
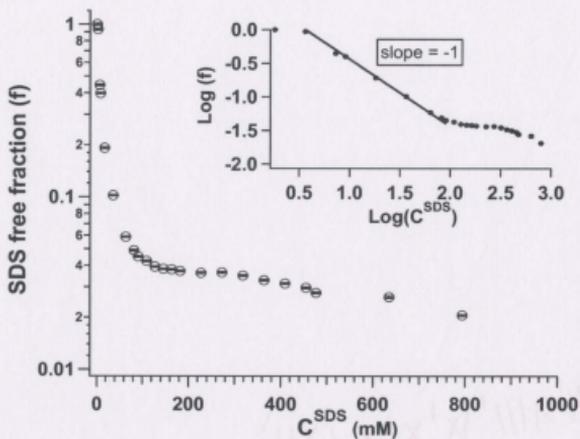
Figure 4.7: SDS free fraction f versus SDS concentration. Inset: A log-log plot yields a slope of -1 for 3.5 mM < C^{SDS} <60 mM. Error bars smaller than symbol size.

dependence of the free SDS fraction f on SDS concentration C^{SDS} shows a linear behavior in the regime where charged SDS/PEO aggregates are expected to form, $\log(f) = -\log(C^{SDS}) + 0.56(1)$. Thus, $f \propto 1/C^{SDS}$ in this concentration range. In figure 4.8, we therefore plot the *concentration* of free SDS , $C_{f2} = f.C^{SDS}$. The concentration of free SDS molecules C_{f2} in the 3.5-60 mM range is almost constant. Fitting this range to a flat line represents an accurate way to estimate the value of CAC, CAC $= C_{free}^{SDS} = 3.53(8)$ mM. This is the most precise method to determine the CAC that we know of. This result is not consistent with surfactant-specific electrode data[44] that suggest that the free SDS concentration is not constant in this region. Interpretation of these latter results above the CAC, however, involves an additional calibration procedure. The diffusometry results for SDS/PEO solutions are very analogous to what is expected for pure SDS solutions, where the SDS monomer concentration reaches a plateau value that is close to the CMC.[27]
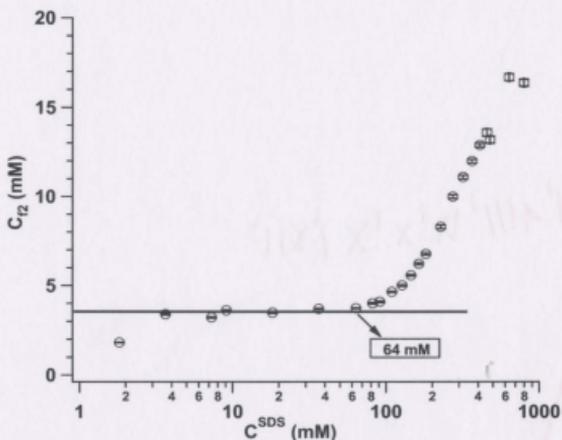
Figure 4.8: Minimal two-species model: the dependence of the concentration of free SDS C_{f2} on the total SDS concentration. Error bars smaller than symbol size.

Samples at concentrations above the one at 64 mM exhibit a sharp increase in C_{f2} (e.g., fig-
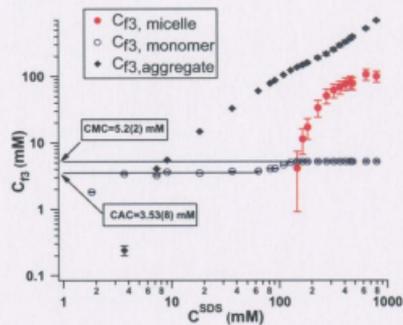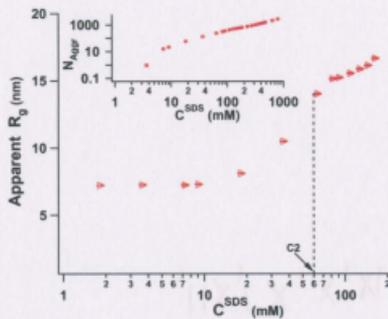
Figure 4.9: (a) Three-species model: the dependence of the concentration of free SDS monomers $C_{f3,monomer}$ and SDS molecules in the micelles $C_{f3,micelle}$ on the total SDS concentration and (b) The apparent radius of gyration of PEO-SDS aggregates, R_g, versus SDS concentration. The concentration C_2 is shown as a guide. Inset: Number of SDS molecules per PEO molecule in an SDS/PEO aggregate, N_{Aggr}, versus SDS concentration. Error bars smaller than symbol size.

ure 4.8). The sharp increase in C_{f2} is clearly not physical. The minimal model for the pure SDS system implies that the free SDS concentrations never exceeds the CMC. We may thus assume that all the excess SDS in the PEO/SDS/D$_2$O system is actually in the form of free micelles. If we denote the total SDS concentration when the free SDS concentration reaches CMC as C_m, then clearly the two-species model, which is valid below C_m, breaks down above C_m. Thus our minimal three-species model is summarized as follows:

$$D_{Obs}^{SDS} = \left(\frac{C_{f3,monomer}}{C^{SDS}}\right) D_{free}^{SDS} + \left(\frac{C_{f3,aggregate}}{C^{SDS}}\right) D_{Obs}^{PEO}, \qquad C^{SDS} \leq C_m$$

$$D_{Obs}^{SDS} = \left(\frac{CMC}{C^{SDS}}\right) D_{free}^{SDS} + \left(\frac{C_{f3,micelle}}{C^{SDS}}\right) D_{micelle}^{SDS} + \left(\frac{C_{f3,aggregate}}{C^{SDS}}\right) D_{Obs}^{PEO}, \qquad C^{SDS} > C_m, \qquad (4.7)$$

where $C_{f3,monomer}$ is the concentration of free SDS molecules and $C_{f3,micelle}$ is the concentration of SDS molecules in the micelles, and

$$C_{f3,aggregate}[mM] = C^{SDS} - C_{f3,monomer}, \qquad C^{SDS} \leq C_m$$

$$C_{f3,aggregate}[mM] = C^{SDS} - (CMC + C_{f3,micelle}), \qquad C^{SDS} > C_m. \qquad (4.8)$$

From the observed diffusion coefficients (D_{Obs}^{SDS}, D_{Obs}^{SDS}, and D_{Obs}^{PEO}) and having a reasonable estimate $D_{micelle}^{SDS}$ from the pure SDS solutions we can calculate $C_{f3,monomer}$ below C_m and $C_{f3,micelle}$ above C_m. This is depicted in figure 4.9a. We can also estimate the radius of gyration of the PEO – SDS aggregates using equation 4.3 (e.g., figure 4.9b). This is only valid when crowding effects are negligible. This is clearly the case for $C^{SDS} < C_2 \approx 60$ mM when the volume fraction Φ in a system of pure spherical SDS micelles is ≈ 0.04 mM); C_2 is the concentration where the SDS monomer concentration starts to increase above the plateau CAC value (e.g., figure 4.9a), and the polymer relaxation rate has reached a plateau value (e.g., figure 4.6). Figure 4.9b (inset) shows the variation of the average number of SDS molecules $N_{Aggr} = \frac{C_{f3,aggregate}[mM]}{0.25[mM]}$, where we have used a PEO concentration of 5 mg/ml and $M_w = 20,000$, for an SDS/PEO aggregate over the whole range of SDS concentration.

110

Fitting model to data yields $C_m \approx 145$ mM. The logarithmic increase in $C_{f3, \text{micelle}}$ above C_m is consistent with the modest increase in the ratio of observed SDS to PEO diffusion coefficients.

Finally, the top curve in figure 4.5a shows the variation of the measured self-diffusion coefficient of DOH molecule at different SDS concentrations. The DOH self-diffusion coefficient is almost constant for $C^{SDS} < 100$ mM where both PEO and SDS self-diffusion coefficients are decreasing. For $C^{SDS} > 100$ mM there is a decrease in the DOH self-diffusion coefficient. This could arise from DOH molecules that associate with the surface of charged SDS micelles or SDS-PEO aggregates, as well as obstruction effects (in a system of pure spherical SDS micelles we estimate the volume fraction to be $\Phi \approx 0.07$ at $C^{SDS} = 100$ mM.

Figure 4.10 shows the variation of DOH relative diffusion coefficient y as a function of SDS concentration, where y is defined by:

$$D_{\text{Obs}}^{\text{DOH}} \approx y D_{\text{Bulk}}^{\text{DOH}}. \tag{4.9}$$
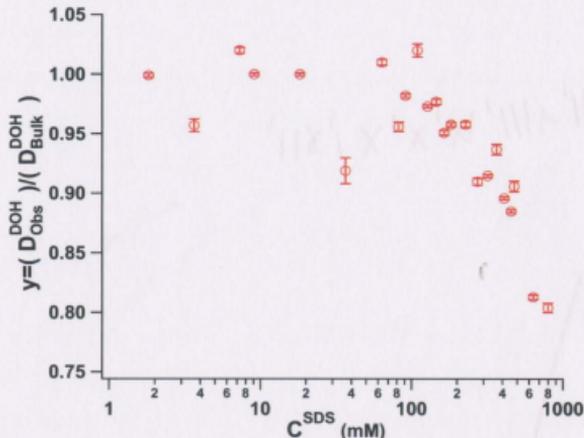
Figure 4.10: Relative DOH diffusion coefficient exhibits a noticeable decrease above ≈ 100mM

We find in this study that there are two distinct concentrations above the CAC:

1. From diffusion measurements, we infer that when the SDS free concentration C_{free}^{SDS} rises above CAC, this indicates the onset of more crowded surfactant environment. We denote this first concentration as C_2. This coincides with the crossover concentration for relaxation behavior (e.g., figure 4.6), $C_2 = 60$ mM. This corresponds to $N_{Aggr} \approx 240$.

2. The ratio of SDS to PEO diffusion coefficients exhibits a minimum at ≈ 100 mM. Applying the minimal model (equation 4.7) to our diffusion results for PEO-SDS yields a critical concentration $C_m \approx 145$ mM, above which free micelles must exist. The increase in the ratio of observed SDS and PEO diffusion coefficients above C_m is therefore simply attributable to the proliferation of free micelles (which are smaller and more mobile than the the polymer-surfactant aggregate).

The chemical shifts, diffusometry, and relaxometry results present a coherent picture. The SDS monomer concentration saturates at the CAC value, while N_{Aggr} (number of SDS molecules aggregated on the polymer) gradually increases. At C_2, the increase in SDS monomer concentration is sharp, however the aggregation number continues to increase. The relatively broad crossover as seen by the polymer is thus consistent with a sharper crossover in the free SDS concentration.

4.6 Conclusion

The study of the molecular dynamics in the SDS/PEO system using the NMR technique gives us an opportunity to make quantitative statements about macromolecular aggregates in a model polymer-surfactant system. The ratio of SDS and PEO diffusion coefficients in PEO(0.5%w/v)/SDS/D_2O solution (e.g, figure 4.5a) revealed a sharp decrease below 100 mM followed by a slight increase for $C^{SDS} > 100$ mM. Moreover, for $C^{SDS} > 100$ mM the DOH diffusion coefficient decreases, likely

indicating an increase in the fraction of water associated with the charged surfactant (e.g., figure 4.10), as well as an increase in obstruction effects.

Relaxation rate difference measurements report on slower aggregate motions. Proton NMR relaxation rate measurements show a clear separation between two regimes of aggregate motions with a crossover at a concentration $C_2 = 60$ mM.

We assumed that the self-diffusion coefficient for SDS is a linear combination of the self-diffusion coefficient of both free SDS molecules and the polymer-associated SDS molecules below C_2 while it includes a third species (free micelles) above C_m. Our analysis revealed that the concentration of free SDS molecules is almost constant ($\pm 3\%$) from 3.5 mM up to a concentration $C_2 = 60$ mM (e.g., figure 4.8). Self-consistently, this plateau concentration value coincides with the CAC, giving us additional confidence in the model in this range. Indeed, the average free SDS concentration in this range is a very accurate way to locate the CAC, we obtain a value of 3.53(8) mM.

Allowing for a third species (free micelles) when $C_{f3} > $ CMC, we find that $C_{f3,micelle}$ increases sharply at $C^{SDS} = C_m$ (e.g., figure 4.9a). The average number of SDS molecules for each PEO molecule N_{Aggr} increases over the entire range of SDS concentration (e.g., figure 4.9b) i.e. it never saturates.

We were able to calculate the concentration of free SDS molecules $C_{f3,monomer}$, the SDS concentration in the PEO – SDS aggregates $C_{f3,aggregate}$, and the concentration of SDS molecules in the micelles $C_{f3,micelle}$ over the entire range of SDS concentration. To summarize:

1. The concentration of free (monomeric) SDS $C_{f3,monomer}$ is constant at CAC for a range of total SDS concentrations below $C_2 = 60$ mM (e.g., figure 4.8). We can make a strong statement here, no free micelles exist below 60 mM. Above C_2, the free monomer concentration $C_{f3,monomer}$ begins to increase. This indicates the onset of surfactant crowding environment on the polymer chain. Since the monomer concentration is still below the CMC value for

113

pure SDS solutions, micelles are still not expected.

2. Above $C_m = 145$ mM, free micelles form (e.g., figure 4.9a). $C_{f3,monomer}$ stays at the CMC for concentrations above C_m, while the concentration of SDS molecules in the micelles $C_{f3,micelle}$ increases from zero to over 100 mM.

3. In the range between CAC and C_2, the chemical environment for the SDS molecules in SDS – PEO solution (as seen from the chemical shift differences labeled in figure 4.3) is maximally different from that at identical concentration in pure SDS solution. This indicates that the SDS conformations in the micelle in pure SDS solution are different from those in the SDS – PEO aggregate (e.g., figure 4.3); in particular, the SDS1 group (closest to the ionic head group of the surfactant) is less well shielded than in SDS-PEO aggregates. Our NMR results do not provide a more detailed geometric picture of the nature of the aggregates.

4. The PEO-SDS aggregate keeps increasing in size (e.g. figure 4.9b and inset). While $C_{f3,micelle}$ increases logarithmically, the number of SDS molecules attached to the aggregate increases roughly linearly with SDS concentration. Our three-species model is likely an under-estimate of the micellar concentration, as it assumes $D_{micelle}^{SDS}$ is a constant (which is an overestimate at higher concentrations due to obstruction effects).

5. There is a clear unambiguous distinction (e.g. figure 4.9a) between C_2 (the onset of surfactant crowding on the polymer chain) and C_m (the onset of free micelles in solution). This is seen qualitatively from relaxation and diffusion data and quantitatively from fits to a minimal model to interpret the diffusion coefficients.

6. The validity of minimal models is unambiguous and clear below C_2. Above C_m ($\phi \approx 0.1$), all results (e.g., figure 4.3b, figure 4.4a, figure 4.9b, and figure 4.10) point to the importance of crowding.

114

Taken together, our results suggests continuous changes in the aggregation phenomenon over the investigated concentration with three distinct concentrations that signal changes in the nature of the aggregates.

Bibliography

[1] Suliman Barhoum and Anand Yethiraj. An NMR study of macromolecular aggregation in a model polymer-surfactant solution. *The Journal of Chemical Physics*, 132:024909/1–9, 2010.

[2] E. Desmond Goddard and James V. Gruber. *Principles of Polymer Science and Technology in Cosmetics and Personal Care*. Marcel Dekker Inc, Dekker, New York London, 1st edition, 1999.

[3] Francoise M. Winnik and Sudarshi T.A. Regismond. Fluorescence methods in the study of the interactions of surfactants with polymers. *Colloids and Surfaces A: Physicochemical and Engineering Aspects*, 118:1–39, 1996.

[4] E. Desmond Goddard. Polymer-surfactant interaction part 1. uncharged water-soluble polymers and charged surfactants. *Colloids and Surfaces*, 19:255–300, 1986.

[5] Daniel S. Banks and Cecile Fradin. Anomalous diffusion of proteins due to molecular crowding. *Biophysical Journal*, 89:2960–2971, 2005.

[6] Reginald John Ellis. Macromolecular crowding: an important but neglected aspect of the intracellular environment. *Current Opinion in Structural Biology*, 11:114–119, 2001.

[7] Jedrzej Szymanski, Adam Patkowski, Agnieszka Wilk, Piotr Garstecki, and Robert Holyst. Diffusion and viscosity in a crowded environment: from nano- to macroscale. *The Journal of Physical Chemistry B*, 110:25593–25597, 2006.

[8] Matthias Weiss, Markus Elsner, Fredrik Kartberg, and Tommy Nilsson. Anomalous subdiffusion is a measure for cytoplasmic crowding in living cells. *Biophysical Journal*, 87:3518–3524, 2004.

[9] Pau Bernado, Jose Garcia de la Torre, and Miquel Pons. Macromolecular crowding in biological systems:hydrodynamics and nmr methods. *Journal of Molecular Recognition*, 17:397–407, 2004.

[10] Krishnan Chari, John Kowalczyk, and Jyotsana Lal. Conformation of poly(ethylene oxide) in polymer-surfactant aggregates. *The Journal of Physical Chemistry B*, 108:2857–2861, 2004.

[11] Krishnan Chari, Brian Antalek, and John Minter. Diffusion and scaling behavior of polmer-surfactant aggregates. *Physical Review Letters*, 74:3624–3627, 1995.

[12] Hans Evertsson, Stefan Nilsson, Christopher J. Welch, and Lars-Olof Sundelof. Molecular dynamics in dilute aqueous solutions of ethyl(hydroxyethyl)cellulose and sodium dodecyl sulfate as investigated by proton NMR relaxation. *Langmuir*, 14:6403–6408, 1998.

[13] Magne Ivar Gjerde, Willy Nerdal, and Harald Hoiland. Interactions between poly(ethylene oxide) and sodium dodecyl sulfate as studied by NMR, conductivity, and viscosity at 283.1–298.1 K. *Journal of Colloid and Interface Science*, 197:191–197, 1998.

[14] B. Cabane and R. Duplessix. Organization of surfactant micelles adsorbed on a polymer molecule in water: a neutron scattering study. *Journal de Physique*, 43:1529–1542, 1982.

[15] Maria de Fatima Carvalho Costa, Sandro Jose Froehner, Angelo Adolfo Ruzza, Sonia de Fatima Santos, and Dino Zanette. Discrepancies over the onset of surfactant monomer aggrega-

tion interpreted by fluorescence, conductivity and surface tension methods. *Quimica Nova*, 21:272–277, 1998.

[16] Fioretta Asora, Luigi Feruglio, and Giorgio Pellizer. ^{23}Na relaxation in SDS and SDES-polymer systems. *Colloids and surfaces A: Physicochemical and engineering aspects*, 245:127–132, 2004.

[17] J. Francois, J. Dayantis, and J. Sabbadin. Hydrodynamical behaviour of the poly(ethylene oxide)-sodium dodecylsulphate complex. *European Polymer Journal*, 21:165–174, 1985.

[18] Luca Bernazzani, Silvia Borsacchi, Donata Catalano, Paolo Gianni, Vincenzo Mollica, Matteo Vitelli, Fioretta Asora, and Luigi Feruglio. On the interaction of sodium dodecyl sulfate with oligomers of poly(ethylene glycol) in aqueous solution. *The Journal of Physical Chemistry B*, 108:8960–8969, 2004.

[19] H.Z. Yuan, L. Luo, L. Zhang, S. Zhao, S.Z. Mao, J.Y. Yu, L.F. Shen, and Y.R. Du. Aggregation of sodium dodecyl sulfate in poly(ethylene glycol) aqueous solution studied by ^{1}H NMR spectroscopy. *Colloid and Polymer Science*, 280:479–484, 2002.

[20] Erik Pettersson, Daniel Topgaard, Peter Stilbs, and Olle Soderman. Surfactant/nonionic polymer interaction. A NMR diffusometry and NMR electrophoretic investigation. *Langmuir*, 20:1138–1143, 2004.

[21] Edson Minatti and Dino Zanette. Salt effects on the interaction of poly(ethylene oxide) and sodium dodecyl sulfate measured by conductivity. *Colloids and Surfaces A: Physicochemical and Engineering Aspects*, 113:237–246, 1996.

[22] Magne Ivar Gjerde, Willy Nerdal, and Harald Hoiland. A NOESY NMR study of the interaction between sodium dodecyl sulfate and poly(ethylene oxide). *Journal of Colloid and Interface Science*, 183:285–288, 1996.

[23] Elson S. de Alvarenga, Claudio F. Lima, and Angelo M. L. Denadai. Study of aqueous solution of sodiumdodecylsulfate and polyethyleneoxide 10000 by NMR NOESY. *Z. Naturforsch*, 59a:291–294, 2004.

[24] Krishnan Chari, Brian Antalek, Min Y. Lin, and Saroj K. Shin. The viscosity of polymer-surfactant mixtures in water. *The Journal of Chemical Physics*, 100:5294–5300, 1994.

[25] Jing Zhao and B. M. Fung. NMR study of the transformation of sodium dodecyl sulfate micelles. *Langmuir*, 9:1228–1231, 1993.

[26] Magne Ivar Gjerde, Willy Nerdal, and Harald Hoiland. Solubilization of 1-butanol in a sodium dodecyl sulfate-poly(ethylene oxide) system by NMR and conductivity at 298.1 and 283.1 K. *Colloid and Polymer Science*, 276:503–510, 1998.

[27] Jacob Israelachvili. *Intermolecular and Surface Forces*. Academic Press Limited, London, 2nd edition, 1991.

[28] Xiaohong Cui, Shizhen Mao, Maili Liu, Hanzhen Yuan, and Youru Du. Mechanism of surfactant micelle formation. *Langmuir*, 24:10771–10775, 2008.

[29] Magnus Bergstrom and Jan Skov Pederson. Structure of pure SDS and DTAB micelles in brine determined by small-angle neutron scattering (SANS). *Physical Chemistry Chemical Physics*, 1:4437–4446, 1999.

[30] Bernard Cabane. Structure of some polymer-detergent aggregates in water. *The Journal of Physical Chemistry*, 81:1639–1645, 1977.

[31] Rajaram Nagarajan, Christopher Drew, and Charlene M. Mello. Polymer-micelle complex as an aid to electrospinning nanofibers from aqueous solutions. *The Journal of Physical Chemistry C*, 111:16105–16108, 2007.

[32] Magnus Nydn and Krister Holmberg. NMR for studying structure and dynamics in colloidal systems. *Current Opinion in Colloid & Interface Science*, 14:169–170, 2009.

[33] Josette M. Landry, D. Gerrard Marangoni, Deborah A. Arden, Ian J. MacLennan, and Jan C. T. Kwak. A 1D- and 2D-NMR study of an anionic surfactant/neutral polymer complex. *Journal of Surfactants and Detergents*, 12:155–164, 2009.

[34] William S. Price. Pulsed-field gradient nuclear magnetic resonance as a tool for studying translational diffusion: Part I. basic theory. *Concepts in Magnetic Resonance*, 9:299–336, 1997.

[35] Charles S. Johnson. Diffusion ordered nuclear magnetic resonance spectroscopy: principles and applicationst. *Progress in Nuclear Magnetic Resonance Spectroscopy*, 34:203–256, 1999.

[36] Mao Shi-Zhen and Du You-Ru. ^{1}H NMR studies of surfactants in aqueous solutions. *Acta Physica Sinica*, 19:675–680, 2003.

[37] Wilson Poon and David Andelman. *Soft Condensed Matter Physics in Molecular and Cell Biology*. CRC Press, New York London, 1st edition, 2006.

[38] James Keeler. *Understanding NMR Spectroscopy*. John Wiley & Sons Ltd, Chichester, 1st edition, 2005.

[39] Z. Gao, R. E. Wasylishen, and Jan C. T. Kwak. NMR studies in surfactant and polymer-surfactant systems : micelle formation of sodium w-phenyldecanoate and interaction with poly(ethylene oxide). *Journal of Colloid and Interface Science*, 137:137–146, 1990.

[40] H. Wennerstrom, B. Lindman, O. Soderman, T. Drakenberg, and J. B. Rosenholm. ^{13}C magnetic relaxation in micellar solutions influence of aggregate motion on TI. *Journal of the American Chemical Society*, 101:6860–6864, 1979.

[41] Roderick E. Wasylishen, Jan C. T. Kwak, Z. Gao, Elisabeth Verpoorte, J. B. Macdonald, and Ross M. Dickson. NMR studies of hydrocarbons solubilized in aqueous micellar solutions. *Canadian Journal of Chemistry*, 69:822–833, 1991.

[42] Olle Soderman, Peter Stilbs, and William S. Price. NMR studies of surfactants. *Concepts in Magnetic Resonance Part A*, 23A:121–135, 2004.

[43] Arun Yethiraj. A monte carlo simulation study of branched polymers. *The Journal of Chemical Physics*, 125:1–10, 2006.

[44] S. M. Ghoreishi, Y. Li., D. M. Bloor, J. Warr, and E. Wyn-Jones. Electromotive force studies associated with the binding of sodium dodecyl sulfate to a range of nonionic polymers. *Langmuir*, 15:4380–4387, 1999.

Chapter 5

Characterization of Dynamics and Internal Structure of a Mixed-Surfactant Wormlike Micellar System Using NMR and Rheometry

5.1 Abstract

We use complementary experiments - proton NMR diffusometry and relaxometry, deuterium NMR lineshapes and rheometry - to construct a comprehensive picture of the microscopic structure of a mixed-surfactant wormlike micellar system composed of a zwitterionic surfactant and an anionic surfactant in brine. In this system, the time of micellar breaking and recombination τ_b is not small

compared with the micellar reptation time τ_R, weakening the condition to obtain a stress relaxation function with just one relaxation time at long times. From NMR relaxometry, we determined the overlap concentration. Deuterium NMR spectral lineshapes indicate the presence of orientational disordered domains with slow exchange between domains. NMR diffusometry and rheology probe different timescales and yield complementary information indicating polymer-like behaviour at the corresponding lengthscales. Via NMR, surfactant diffusion coefficients are seen to decrease with increasing diffusion time, consistent with restricted diffusion within a reptating micelle. At the same time, comparison of measurements with protonated and deuterated surfactant strongly suggest that the short and long time diffusion coefficients measured correspond to intra-micellar and micellar diffusion respectively. Fitting the diffusion results to a simple model, the average end-to-end micellar distance was estimated to be in the 1 μm range and only weakly dependent on concentration. The water diffusion measurements, on the other hand, imply a great degree of water structuring at the micellar surface. We also found that the wormlike micelles obeyed simple polymer-like scaling behaviors with a crossover from Zimm-like (diffusion) to Rouse-like (rheology) exponents.

5.2 Introduction

Amphiphilic molecules in aqueous solution form aggregates with different structures such as bilayers, vesicles, spherical, and cylindrical or wormlike micelles, depending on molecular geometry as well as on the net charge and surfactant concentration.[1] Wormlike micelles are interesting due to the fact that they are elongated objects like polymers (which have interesting dynamics and hydrodynamic effects[2-5]); however they continuously break and recombine.[6-10] This has technological applications (from heat-transfer fluids to oil-field applications to drain-openers[9]) because unlike normal polymers they can reform after breaking and can thus survive repeated shear.[6]

Much work has been carried out on the study of wormlike micelles via theory[8,11-13] and com-

puter simulation[14,15] and there have been several reviews of the subject.[6,7,10,15,16] Experimentally, wormlike micellar systems can be composed of cationic, anionic, zwitterionic or non-ionic surfactants.[6,8,17–20] Mixtures of cationic and anionic surfactant,[21] zwitterionic dimeric surfactant solutions[22] and cationic surfactants solutions[20,23] have also been investigated. Rheology has been used to explore the phase and micellar structure in several systems. A common surfactant in wormlike micelle literature is cetyl trimethylammonium bromide (CTAB)[24–28] which forms cylindrical wormlike surfactant micelles; systems forming reverse micelles have also been reported.[29,30]

Small-angle neutron scattering and dynamic light scattering studies have reported on isotropic to nematic phase transitions,[24] transitions from vesicles to wormlike micelles,[31] the concentration dependence of the hydrodynamic correlation length,[32] and the effect of adding salt on the micellar growth.[33] Scattering measurements have also characterized important lengths of the micellar network[34] and have been used to investigate local structure and flexibility.[35,36] Combinations of rheology and small angle neutron scattering (Rheo-SANS) have also been used to study concentration dependences of shear thinning and alignment in a block copolymer wormlike micellar system.[37]

Pulsed-field-gradient nuclear magnetic resonance was used to identify sub-diffusive behavior in a wormlike reverse micelle system.[38] This technique has been employed in other (polymer and protein) soft matter systems[39–41] to provide information that is complementary to scattering methods, and is especially useful when the system contains large and/or multi-component aggregates. This is because spectral separations of different chemical components is easy in NMR, challenging in scattering, and practically impossible in rheology.

Recently, a multi-component system consisting of mixtures of two similar-sized surfactants, one zwitterionic (N-tetradecyl-N,N-dimethyl-3-ammonio-1-propanesulfonate or TDPS) and the other anionic (sodium dodecyl sulfate or SDS) in brine[34,42,43] has been studied by rheology and scattering techniques. The TDPS/SDS system was studied in a range of TDPS concentrations C_z spanning both dilute and semidilute regime at different surfactant ratios R= [SDS]/[TDPS] and different temperatures.[34,42,43] The average micelle contour length is found to be in the micron range

and (for $R = 0.55$) to increase with C_z when the wormlike micelles are totally screened by salt addition, while the "mesh size" reflecting intermicellar correlations was in the 50 - 100 nm regime and insensitive to changes in C_z, the surfactant concentration ratio or temperature.[34] An interesting feature of this system is that while $R = 0.55$ mixtures could be fit to Maxwellian viscoelastic behavior with a single relaxation time for the stress relaxation modulus G(t) at long times,[43] those for $R = 0.43 - 0.45$ show deviations from the Maxwellian model.[43] Two timescales are relevant in wormlike micellar systems. τ_b refers to the breaking/recombination timescale, while τ_R is the reptation timescale. If the micellar chain breaks and recombines many times during the reptation process (i.e.; $\tau_R \gg \tau_b$), the tube-like contour segments exhibit a single relaxation rate.[8]

In previous work,[39] we have shown that mixed-species (polymer-surfactant) aggregates are easier to study than single-species (surfactant) aggregates because the dynamics of each species can be independently and simultaneously measured via complementary NMR experiments. This allows models of aggregate structure to be sufficiently constrained. In this work, we use the TDPS-SDS system (with $R = 0.45$) to obtain unprecedented detail about both the structure and dynamics in a system where the linear rheology is not dominated by a single relaxation time at low frequencies.

In this work, we used NMR diffusometry and relaxation measurements as well as deuterium NMR to explore the dynamics and the structure of the micellar aggregates. Relaxation in NMR refers usually to two processes by which nuclear magnetization prepared in a non-equilibrium state returns to the equilibrium distribution. Different physical processes are responsible for the relaxation of the components of the nuclear spin magnetization vector $\vec{M}$ parallel and perpendicular to the external magnetic field, $\vec{B_0}$ (which is conventionally oriented along the z axis). These two principal relaxation processes are termed T_1 and T_2 relaxation, respectively. The longitudinal T_1 and transverse relaxation T_2 times can be measured directly using NMR, and can be used to report on changes in the local environment.[44]

In the NMR diffusion experiment, the sample experiences both an external uniform magnetic field from the magnet and a non-uniform spatially well-defined magnetic field (i.e.; pulsed field

gradient). Therefore, the molecular diffusion is measured from the signal attenuation that arises from the dephasing of nuclear spin coherence.[45, 46] Deuterium NMR, on the other hand, is an effective probe of orientational order of the hydrocarbon chains.[47] Thus we are able to obtain independent dynamical information on all components in a 3-component system via spectral separation (via either a difference in chemical shift or spin label) of diffusion coefficients.

Utilizing these complementary NMR techniques on the TDPS-SDS system (with $R = 0.45$), in tandem with rheology, we obtain unprecedented detail about both the structure and dynamics in the case where the linear rheology of the system is not dominated by a single relaxation time at low frequencies.

5.3 Experimental

5.3.1 Materials

N-tetradecyl-N,N-dimethyl-3-ammonio-1-propanesulfonate (TDPS, $M_w = 363.6$, purity > 99%), sodium dodecyl sulfate (SDS, $M_w = 288.38$, purity > 99%), and SDS-D25($M_w = 313.53$, 98 atom % D) were purchased from Sigma-Aldrich Canada and were used as received. We prepared stock solutions of TDPS/SDS/NaCl(0.5M)/D_2O as well as TDPS/SDS – D25/NaCl(0.5M)/H_2O at $C_z = 50$ mM, as well as the brines NaCl(0.5M)/D_2O and NaCl(0.5M)/H_2O. Samples with TDPS concentration and protonated/deuterated SDS below 50 mM (in the semidilute regime) were prepared by diluting with brine made of D_2O/ H_2O respectively. The sample in the concentrated regime $C_z = 140$ mM was prepared separately. The surfactant ratio in all samples was $R = $ [SDS]/[TDPS] = 0.45. Deuterium oxide D_2O (for all protonated SDS samples) and deuterium-depleted H_2O (for deuterated SDS samples) were purchased from Cambridge Isotope Laboratories. While surfactant mixtures were prepared by addition of constituents by mass, the volume fraction is the relevant quantity when considering hydrodynamic corrections. We estimate a volume fraction

Φ using

$$\Phi = \frac{V_{TDPS} + V_{SDS}}{V_{TDPS} + V_{SDS} + V_{NaCl(0.5M)/H_2O}} \qquad (5.1)$$

where $V_\alpha = m_\alpha/\rho_\alpha$, V_α, m_α and ρ_α are the volume, mass, and density of the α component in solution, with α indicating TDPS, SDS or NaCl(0.5M)/H_2O. Note that this is an estimate of volume fraction by the assumption of volume additivity. Because of the densities ($\rho_{TDPS} = \rho_{SDS} \approx 1 g/cm^3$, and $\rho_{NaCl(0.5M)/H_2O} \approx 1.02 \ g/cm^3$) our estimated volume fraction is essentially equivalent to the mass fraction.

NMR spectra were collected on a Bruker Avance II spectrometer with a ^1H resonance frequency of 600.33 MHz and a ^2H resonance frequency of 92.15 MHz. We can easily separate the water peak at 4.7 ppm and the surfactant peaks spectrally in the NMR spectrum. However due to the broad (super-Lorentzian) lineshapes we are unable to spectrally separate TDPS and SDS peaks (0 - 4 ppm). Thus we prepared some samples with deuterated SDS. We are then able to compare surfactant dynamics of TDPS (proton NMR with deuterated SDS yields only the TDPS peaks) with surfactant dynamics of TDPS-SDS peaks in protonated SDS samples.

Relaxation measurements were performed using a Micro-5 imaging (3-axis gradient) probe. The inversion recovery technique was used to measure T_1: sixteen time delays were used, and the integrated intensities in the spectrum were fitted to the equation: $I(t) = I_o (1 - 2 \exp(-t/T_1))$.[44] A $(\pi/2)_x$-t/2-$(\pi)_x$-t/2-acquire spin echo experiment was used to measure T_2: 16 values, at delay time t, of the integrated intensity were taken to measure T_2 and were fitted to the equation: $I(t) = I_o \exp(-t/T_2)$.[44]

Three-axis self-diffusion measurements were carried out in a Micro-5 imaging (3-axis gradient) probe with a maximum gradient strength of 200 G/cm or a Diff30 diffusion probe with a maximum field gradient 1800 G/cm employing a pulsed-field gradient stimulated-echo sequence[46] with trapezoidal gradient pulses. In our experiments, the duration δ of field gradient pulse is 2 ms, and the gradient g was varied in steps from 0% to $\approx$ 100%. For deuterated SDS samples, ^2H

NMR spectra were collected using a $(\pi/2)_x$-t-$(\pi/2)_y$-t-acquire quadrupole echo experiment with 256 scans was used, with t = 10 μs.

Spectrally resolved molecular diffusion coefficients along the field direction (D_z) and perpendicular to the field direction (D_x and D_y) are obtained from the attenuation of the signal according to the equation:[45]

$$D = \frac{-1}{k} \ln\left(\frac{S(k)}{S(0)}\right) \qquad (5.2)$$

where S(k) is the integrated intensity of the signal in the presence of field gradient while S(0) is the intensity of the signal in absence of field gradient, and $k = (\gamma \delta g)^2 (\Delta - \delta/3)$ is a generalized gradient strength parameter. The diffusion time Δ is the duration in the pulse sequence in which molecular diffusion has an affect on the signal attenuation. The signal attenuation as a function of k associated with TDPS-SDS peaks is a single exponential over the whole range of TDPS concentration. When there is free bulk diffusion, the diffusion coefficient does not depend on diffusion time Δ.

5.3.2 Rheometry

Rheological measurements were carried out on an Anton Paar Physica MCR 301 rheometer. All the rheometric measurements were done at T = 298 K using the cone-plate geometry of 50 mm diameter and 0.5° cone angle. The stress relaxation experiments were performed with an applied shear strain γ = 0.5. The flow curves experiments were carried out with shear strain rate $\dot{\gamma}$ varying from 0.001 to 150 1/s. In addition, the oscillatory shear experiments were performed with an angular frequency ω varied in log-ramp from 50 rad/s to 0.01 rad/s.

5.4 Results and Discussion

5.4.1 NMR Relaxation and the Overlap Concentration

Longitudinal T_1 and transverse T_2 relaxation measurements were carried out for TDPS/SDS/NaCl (0.5M)/D_2O samples at different TDPS concentration C_z. The proton longitudinal relaxation rate $R_1 = 1/T_1$ (figure 5.1) can be fit to a mono-exponential decay, with a significant increase as one crosses the overlap concentration (reported to be at 7 mM by Lopez-Diaz et al[42]). The monoexponential fit is phenomenological. The change in R_1 indicates a change in the local environment for the surfactant molecules which corresponds well with the wormlike micelle overlap concentration. Based on the exponential fit, we extract a characteristic concentration of $C^{threshold} = (5.9 \pm 0.6)$ mM (i.e.; $C^{threshold} \approx C^*$). The T_2 relaxation time (not shown) shows no appreciable change as a function of TDPS concentration C_z.
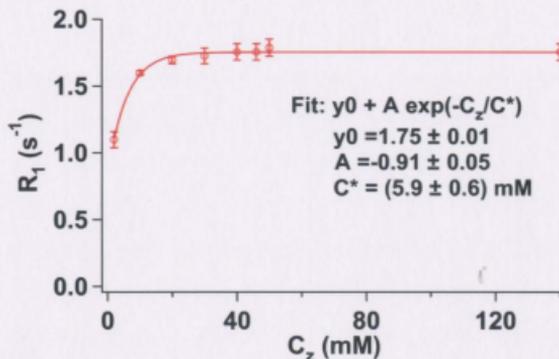

Figure 5.1: Proton longitudinal relaxation rate $R_1 = 1/T_1$ versus TDPS concentration C_z for TDPS/SDS /NaCl(0.5M)/D_2O samples at T=298K.

5.4.2 Deuterium NMR and Orientational Structure

Measurements with deuterated SDS provide good opportunities to look at the orientational structure of the SDS (using deuterium NMR), and to separate the dynamics of the TDPS (using proton diffusometry). We also use these samples to measure the variation of the water diffusion coefficient with surfactant concentration.

Figure 5.2a shows ^{2}H NMR spectra for $C_z = 46$ mM as a function of temperature. The appearance of a single broad peak in the deuterium NMR spectrum implies a structure that is intermediate between an isotropic liquid and an oriented liquid. It is likely an indication of the presence of a liquid crystal mesophase in domains with wide orientational angular distribution where there is a slow exchange between the domains.[47] As we will describe below, this is consistent with the interpretations of figure 5.3a where we see only a small anisotropy in the measured diffusion coefficient. This averages out the first-order quadrupole coupling.[48] We may fit the deuterium NMR lineshape to the absorption Lorentzian function

$$S(\omega) = \frac{(W/2)}{(W/2)^2 + (\omega - \omega^0)^2} \tag{5.3}$$

where ω and ω^0 are the frequency coordinate and the Larmor frequency of the deuterium (spin-1) nuclei respectively. W is the deuterium peak width at half maximum of the absorption peak.

For deuterated SDS samples (TDPS/SDS – D25/NaCl(0.5M)/H$_2$O) at two TDPS concentrations ($C_z = 10$ and 46 mM), we can extract the deuterium peak width at half maximum (W) of the absorption peak as a function of temperature between 298K and 323K. This peak width in shows an exponential behavior as a function of reciprocal of temperature $1/T$. By globally fitting both data sets in figure 5.2b to one exponential function $W = A \exp(E_a/K_BT)$, we estimate the activation energy to be $E_a \approx 21.8(1)K_BT$. The activation energy associated with narrowing of the spectral lines likely is associated with either slow re-orientation in the local environment of a molecule, or slow molecular exchange between environments with different local orientational order.

Water diffusion in aqueous surfactant solutions has been shown to be a weighted average of
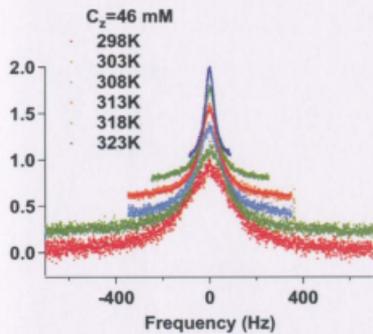
(a)
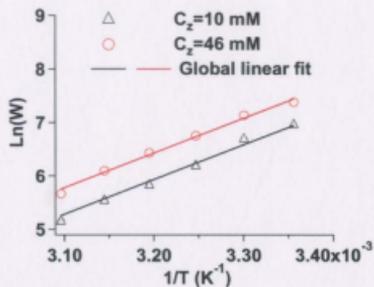
(b)
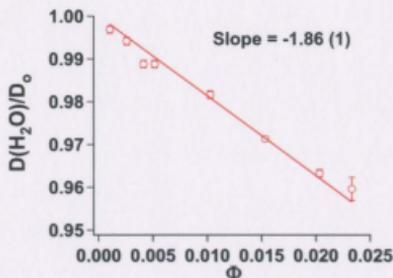
(c)

Figure 5.2: (a) The deuterium NMR lineshape is well fit to a Lorentzian function. The peak width W for $C_z = 46$mM decreases with increasing temperature in the range from 298K to 323K (b) The peak width W exhibits an Arrhenius temperature dependence: results for $C_z = 10$mM and 46mM can both be fit with a single activation energy and (c) Relative H_2O diffusion coefficient versus total surfactant volume fraction Φ in TDPS/SDS – D25/NaCl(0.5M)/H_2O samples at T=298K.

two kinds of water, bulk water and surface associated water.[49] The water molecule is a polar molecule, and it associates with a surface of charged molecules or charged aggregates. It has been shown to be a reasonable approximation to assume that the surface-associated water is essentially stationary in comparison to the bulk water.[39,49] Thus, water diffusion coefficients obtained as a function of surfactant packing fraction report directly on the fraction of surface-associated water. Figure 5.2c shows the variation of the relative self-diffusion coefficient of H_2O molecules in TDPS/SDS – d25/NaCl(0.5M)/H_2O over the range of total surfactant volume fraction Φ from 0.001 to 0.023.

The H_2O diffusion coefficient values are scaled to the bulk diffusion coefficient (i.e.; $D_o = 2.23 \times 10^{-9}$ m^2/s) of H_2O molecule in 0.5 M brine, which we also measured. The decrease in H_2O diffusion coefficient with increasing surfactant volume fraction arises from H_2O molecules associating with the surface of charged cylindrical TDPS-SDS micelles in the aqueous solution. From simple geometry for a cylindrical micelle, we related the observed diffusion coefficient to the thickness of the water layer h (assumed to be static - this is valid since the surfactant diffusion coefficient is 3 orders of magnitude smaller than that of water) and the diameter of the bare cylindrical micelle d:

$$\frac{D}{D_o} \approx 1 - \left(1 + 4\left(h/d + (h/d)^2\right)\right)\Phi. \tag{5.4}$$

A single H_2O monolayer has thickness 0.3nm. Fitting the observed diffusion coefficient in figure 5.2c, we find that h/d = 0.182 ± 0.004. Allowing for the surface-associated water to diffuse like the surfactant diffusion modifies this result slightly to h/d = 0.186 ± 0.004. Given a micellar diameter of d $\approx$ 6nm,[42] this implies a water layer thickness of $\approx$ 3 to 4 monolayers.

5.4.3   Three-axis diffusometry and micelle structure

The observed self-diffusion coefficient (figure 5.3a) measured along z, x, and y axes display a very similar behaviour, and thus exhibit insignificant effects of ordering in the $\approx$ 14 T magnetic field. D_z, D_x and D_y all decrease as a function of diffusion time Δ. If what we measure is only

(a)

(b)

(c)
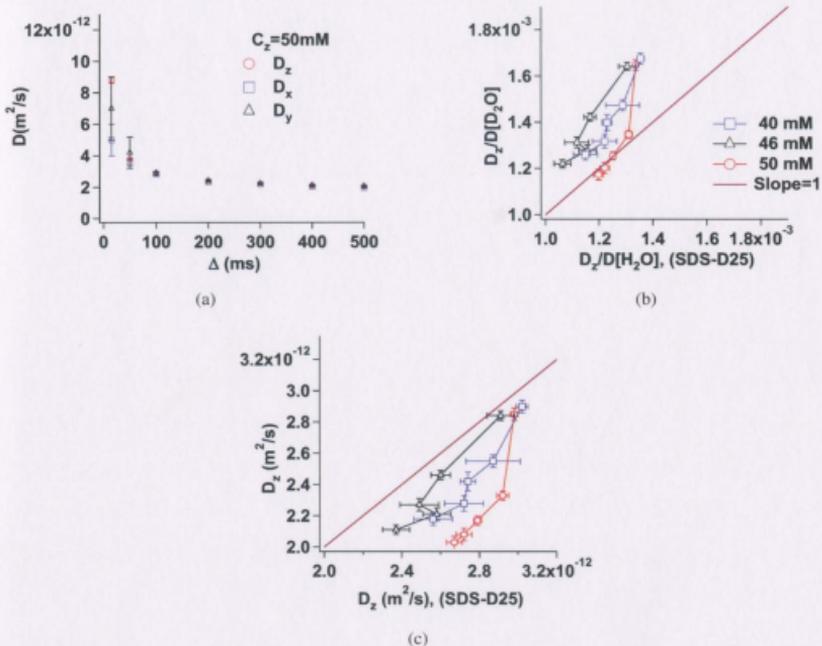
Figure 5.3: (a) TDPS-SDS self-diffusion coefficient (D_x, D_y, D_z) versus diffusion time Δ. $C_z = 50$ mM. (b) Relative z-self diffusion coefficient $\frac{D_z}{D[D_2O]}$ of TDPS/SDS/NaCl(0.5M)/D_2O versus $\frac{D_z}{D[H_2O]}$ of TDPS/SDS $-$ D25/NaCl(0.5M)/H_2O. If the values were equal they would be on the 45 degree line and (c) D_z for non deuterated SDS samples versus that for deuterated SDS samples. $C_z =$ 40mM, 46mM and 50mM at T = 298K.

the self diffusion of the wormlike micelle, then we would not expect D to show a dependence on Δ. For $\Delta \geq 15$ ms, the wormlike micelle is already in the long-time limit due to the fact that the RMS displacement over the millisecond timescale is much larger than the average mesh size of the TDPS/SDS/NaCl(0.5M) micellar solution $\xi \approx 75$ nm.[34]

The observed decrease of D with Δ suggests strongly that the observed diffusion coefficient is a combination of micellar self-diffusion and surfactant self-diffusion inside the micelle. This is confirmed by comparing surfactant diffusion coefficients for systems with non-deuterated and fully deuterated SDS. This is akin to contrast matching experiments in neutron scattering. The surfactant self diffusion coefficient D_z was measured for TDPS/SDS $-$ D25/NaCl(0.5M)/H_2O samples with deuterated SDS at 3 TDPS concentrations (40 mM, 46 mM, and 50 mM). Here we measure the TDPS self-diffusion coefficient, whereas in the protonated samples one measures an average value of TDPS and SDS diffusion coefficients. If the two values are equal they would lie on the 45 degree line. The values obtained for the relative diffusion coefficients in figure 5.3b are only closest to the 45 degree line at the smallest values (corresponding to largest Δ). This is consistent with the notion that the micellar diffusion coefficient should depend only on the micelle size and the solvent viscosity. Therefore, assuming a Stokes-Einstein-like relation for the micelle in the solvent $D \propto 1/\eta$, the diffusion coefficient relative to the solvent diffusion coefficient should be the same for both systems.

Figure 5.3c on the other hand shows the bare self diffusion coefficients D_z. Here we see that the values for deuterated and non-deuterated samples are closest to the 45 degree line for small Δ (i.e.; for large D_z). This is consistent with surfactant diffusion within the micelle - these values should indeed be insensitive to solvent viscosity.

Three-axis diffusion measurements thus show that there is very insignificant anistropy in the wormlike micelle conformations in the presence of a large magnetic field. Moreover, comparisons of measurements in deuterated and non-deuterated surfactant show a clear trend: micellar diffusion is dominant for large Δ, while intramicellar diffusion is dominant for small Δ.
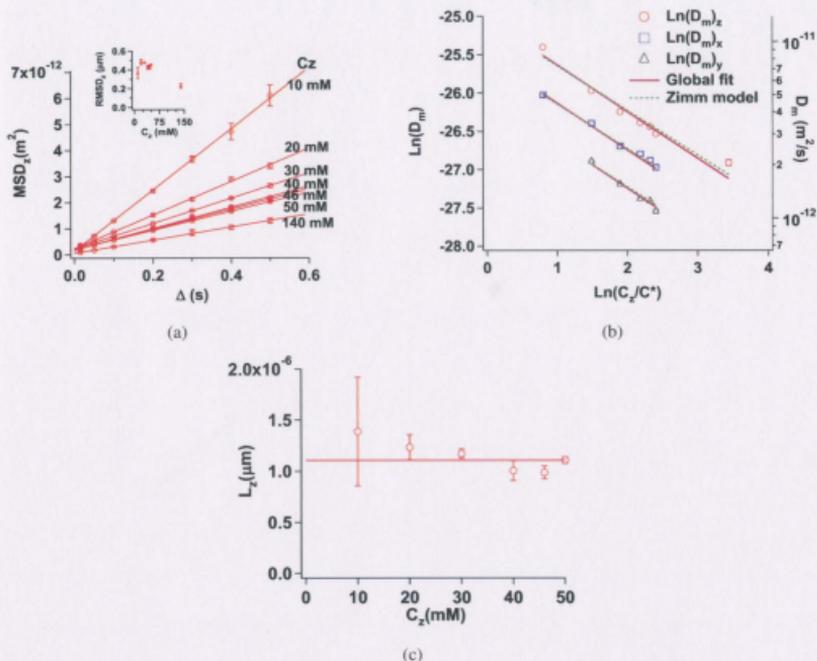
Figure 5.4: (a) Z-axis mean square displacement MSD_z versus diffusion time Δ. Inset: root mean square displacement ($RMSD_z$) versus TDPS concentration C_z (b) Anisotropic micelle self-diffusion coefficients (($D_m)_z$, $(D_m)_x$, $(D_m)_y$) extracted from the slopes of the mean-square displacement MSD curves as a function of TDPS concentration (C_z) for TDPS/SDS/NaCl(0.5M)/D_2O samples at T = 298 K. The anisotropic micelle self-diffusion coefficients $(D_m)_z$ and $(D_m)_y$ curves are offset along the y-axis. (c) The average z-end to end distance L_z of the TDPS-SDS micelle versus TDPS concentration C_z, extracted from a fit of the signal attenuations using equation 5.5, for TDPS/SDS/NaCl(0.5M)/D_2O samples at T=298 K. The mean L_z is around 1.1 μm.

135

5.4.4 Micellar and intramicellar diffusion

From the observed values of anisotropic self-diffusion coefficients (figure 5.3a) at different diffusion times Δ, the mean-square displacement MSD values ($MSD_i = 2D_i\Delta$, $i = x, y, z$) are obtained (figure 5.4a). The dependence is clearly linear; however the straight line does not pass through the origin. Therefore, the diffusion is neither lateral diffusion[50] nor it is single-file diffusion[51] for which the MSD should scale as the square root of the diffusion time. The slope in figure 5.4a represents a reasonable estimate for the micellar diffusion (figure 5.4b) at different TDPS concentration C_z. The non-zero intercept on the other hand, is an indication of faster intra-micellar surfactant diffusion at shorter times.

Figure 5.4b shows the variation of the anisotropic micelle diffusion coefficients $(D_m)_x$, $(D_m)_y$ and $(D_m)_z$ of the micelle as a function of TDPS concentration in the semidilute regime (i.e.; $10 \text{ mM} \leq C_z \leq 50 \text{ mM}$) for $(D_m)_x$, $(D_m)_y$ and in the $10 \text{ mM} \leq C_z \leq 140 \text{ mM}$ regime for $(D_m)_z$ of TDPS-SDS/NaCl (0.5M)/D_2O. The anisotropic diffusion curves D_z and D_y are offset along the y-axis. The anisotropic self-diffusion coefficients exhibit a power law decrease with respect to C_z.

We globally fit the three datasets in figure 5.4b in the semidilute regime to a single power law (Global fit in graph). Our experiments yield a power law $D = D_Z (C/C^*)^{-d}$ with the exponent $d = 0.58 \pm 0.03$. The Zimm model for polymer dynamics in a good solvent considers the hydrodynamic interactions between the monomers on the polymer chain and between the monomers and the solvent molecules in the pervaded volume. It would predict an exponent $d = (1-\nu)/(3\nu-1) = 0.54$ (using $\nu = 0.588$ for a self-avoiding polymer).[2] This exponent is shown for comparison (dashed line labeled "Zimm model" in the graph). We calculate an experimental exponent $\nu = (1+d)/(1+3d) = 0.58 \pm 0.01$. From the power law fit, we also obtain the average Zimm diffusion coefficient D_Z of the wormlike micelle of $8.3(1) \times 10^{-12} \text{ m}^2/\text{s}$.

For free diffusion, D is independent of Δ. For bounded diffusion, the apparent diffusion coefficient is smaller than the true diffusion coefficient at long times when molecules start to feel the

effects of the boundaries. The signal attenuation function S(q) which is related to the diffusion coefficient D via equation 5.2 is modified due to the effect of boundaries. We utilize a simple restricted diffusion model for surfactant diffusion in a one dimensional wormlike micelle.[52] We modify this to incorporate a diffusing micelle, resulting in the following signal attenuation equation:[52]

$$
\ln[S(q)] = -((2\pi q)^2)D_m\Delta + \ln\left[\frac{2[1 - \cos(2\pi qL_z)]}{(2\pi qL_z)^2} + \\ 4(2\pi qL_z)^2\sum_{n=1}^{N}\exp(-\frac{n^2\pi^2D_s\Delta}{L_z^2}) \times \frac{1 - (-1)^n\cos(2\pi qL_z)}{((2\pi qL_z)^2 - (n\pi)^2)^2}\right] \tag{5.5}
$$

here D_s is the molecular bulk surfactant self-diffusion, D_m is the micellar self-diffusion, $q = \gamma\delta g/(2\pi)$ and L_z is the average length of the one-dimensional channel.

As the diffusion time increases, a larger fraction of molecules feel the effects of confinement with the diffusion coefficient not changing much for $\Delta \gtrsim 300$ms. The z-axis signal attenuation curves for each diffusion time in figure 5.3a were fitted to equation 5.5. From this fit (signal attenuation curves and fit not shown), we extract the average end to end distance L_z (figure 5.4c) for the wormlike micelle. The infinite sum in equation 5.5 is approximated by an upper limit $N = 1000$. D_m was obtained from the slopes of figure 5.4a for each TDPS concentration C_z (values obtained for D_m are shown in figure 5.4b). D_s, the free diffusion of surfactant inside a micellar environment, and L_z are fit parameters. A value of $D_s = 13 \times 10^{-12}$ m^2/s provided a good fit for all concentrations. Having the Zimm diffusion coefficient D_Z, the average time τ_Z for a micellar chain to diffuse a distance of order of its average end to end distance L can be calculated.[2] Using $L_z = 1.1(1)$ μm and $D_Z = 8.3(1) \times 10^{-12}$ m^2/s, we get $\tau_Z \approx \frac{L_z^2}{D_Z} \approx 0.15$ s.

137

5.4.5 Rheology and Supramicellar Structure

Relaxation modulus experiments were performed for a range of TDPS concentrations in the semidilute regime (10 mM $\leq C_z \leq$ 50 mM). If the relaxation modulus exhibits a single exponential at long times, then recombination and the scission process is rapid, i.e.; the micellar chain breaks and recombines many times in a time scale $\tau_b << \tau_R$ and the primary relaxation mechanism is reptation.[8]

A stress relaxation dominated by a single exponential relaxation decay is generally consistent with the wormlike character of the self-assembled structures in the solution. If $\tau_R >> \tau_b$, stress relaxation follows a single exponential in wormlike solutions according to the Cates model. Lopez-Diaz et al[43] note that τ_b/τ_R is minimum at R = 0.55, which is precisely the R value where the mixture perfectly fits the Maxwellian Cole-Cole semicircle. While $R = 0.55$ mixtures could be fit to Maxwellian viscoelastic behavior with a single relaxation time for the stress relaxation modulus $G(t)$,[43] those for $R = 0.43$ showed deviations from the Maxwellian model.[43] For our (R = 0.45) samples, all relaxation functions $G(t)$ (not shown) are better fit to a bi-exponential than a single exponential.

The elastic modulus G_o (figure 5.5a) associated with the slower, dominant, relaxation mode is extracted. Reduced viscoelastic spectra are extracted over the whole range of TDPS concentration C_z. The inset in figure 5.5a is an example of Cole-Cole diagram for C_z = 50mM. The upturn in G'' at higher frequencies is an expected outcome of Rouse-like behavior.[53] This elastic modulus (figure 5.5a) scales as $C_z{}^b$ where the exponent b is given[8] by $3\nu/(3\nu-1)$ = 3.0 ± 0.1, implying ν = 0.50 ± 0.01. In addition, the zero-shear-strain viscosity (figure 5.5b) also scales[8] with $C_z{}^s$ with $s=1/(3\nu-1)$ = 2.4 ± 0.1, or ν = 0.47 ± 0.01. Both of these scaling behaviors are in the semidilute regime, and consistent with (ν = 1/2) Rouse-like behavior.
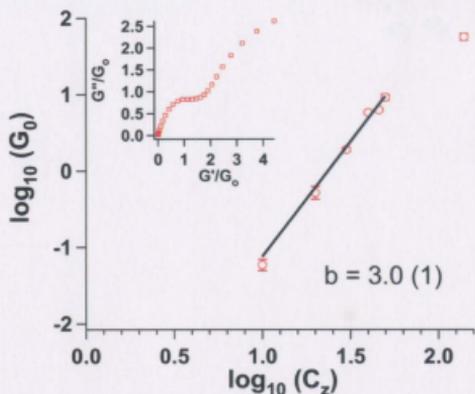
(a)
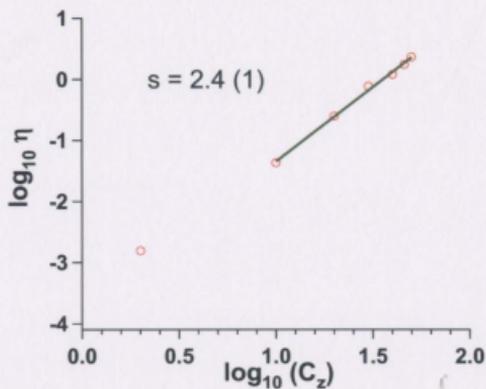
(b)

Figure 5.5: (a) The elastic modulus G_o versus TDPS concentration C_z. Inset: Cole-Cole diagram for $C_z = 50$mM non-deuterated SDS sample (b) Zero-shear strain viscosity η versus TDPS concentration C_z (on a logarithmic scale) for TDPS/SDS/NaCl(0.5M)/D_2O samples. Power law fits in the semi-dilute regime are consistent with the exponent expected for Rouse-like behavior - see text.

5.4.6 Two Polymer-like Scalings

In this work, we observed two distinct polymer-like scalings in micellar dynamics in the semi-dilute regime. Diffusometry in the semi-dilute regime is consistent with a scaling exponent $\nu = 0.58 \pm 0.01$ (consistent with the value of 0.588 for Zimm-like behavior in a good solvent). On the other hand, rheological measurements are consistent with a random-walk scaling exponent of $\nu = 0.5$.

These results have a simple interpretation. In the semidilute regime of mixed-surfactants TDPS/SDS, NMR diffusometry provides access to dynamics at shorter lengthscales and times (where hydrodynamic interactions are not screened) and can be described by Zimm dynamics in a good solvent.[2,4] On the other hand, the rheological measurements provide access to dynamics at larger scales at which the hydrodynamic interactions are screened, and Rouse dynamics results. In spite of the fact that, in order to remain in the semi-dilute regime, the range of the fit is small, the two exponents are distinct (about 8σ apart) and are consistent with classic polymer-like scalings in different hydrodynamic regimes.

5.5 Conclusion

In this work, we carried out several complementary NMR experiments, as well as rheology, and these results yield a comprehensive picture of microscopic structure in a wormlike micellar system. From NMR longitudinal relaxation T_1 measurements (figure 5.1), we estimate the TDPS characteristic overlap concentration $C^* \approx (5.9 \pm 0.6)$ mM. This compares reasonably with the value of $\approx 6 - 7$ mM determined using diffusive wave spectroscopy.[42] In addition, the temperature dependent ^{2}H NMR spectra (figure 5.2a) show a single broad deuterium peak that implies orientational disordered domains with slow exchange between domains. The narrowing of this peak is consistent with the temperature dependence of an isotropic liquid crystal mesophase with slow molecular

exchange between environments with different orientational order.[47]

By measuring the self-diffusion coefficient of the water H_2O molecule in deuterated SDS samples, we were able to obtain the functional dependence of the relative self diffusion coefficient of the water molecules H_2O with respect to the total surfactant volume fraction (figure 5.2c). Often one can assume a single monolayer of surface associated water.[49] In this system however there is the equivalent of 3 to 4 layers of surface-associated water. A pronounced change in water structure has been reported before in neutron diffraction studies of water in high-salt conditions.[54]

Diffusion time dependence on diffusion coefficients (figure 5.3a), linearity of the mean square displacement MSD versus time (but with non-zero offset) (figure 5.4a) and the contrast-matched diffusion experiments all point to a model that includes two ingredients: surfactant restricted diffusion in a cylindrical micelle, and micellar diffusion in water. Therefore, extracting the micellar diffusion from the slopes of the MSD curves (figure 5.4a) and a fit to a simple model with these two ingredients yields an average end-to-end distance of the wormlike micelle in the 1 - 1.5 μm range and is not strongly concentration-dependent (figure 5.4c), which is not far from the contour length found by Lopez-Diaz et al.[43]

Rheology reports on longer timescales and lengthscales than NMR. There appears to be a distinct second relaxation time in the stress relaxation measurements which is also consistent with oscillatory shear measurements (inset in figure 5.5a) that are not purely Maxwellian. This is consistent with previously reports results[43] which showed deviations from the Maxwellian model at $R = 0.45$.

Finally, two distinct (Zimm and Rouse) polymer-like scalings are observed via NMR and rheometry respectively, indicating that the worm-like micelles exhibit classic polymer-like behaviour in different hydrodynamic regimes.

141

Bibliography

[1] Richard. A. L. Jones. *Soft Condensed Matter*. Oxford University Press Inc, New York, 1st edition, 2002.

[2] Michael Rubinstein and Ralph H. Colby. *Polymer Physics*. Oxford University Press, New York, 1st edition, 2003.

[3] Jack F. Douglas and Karl F. Freed. Competition between hydrodynamic screening (draining) and excluded volume interactions in an isolated polymer chain. *Macromolecules*, 27:6088–6099, 1994.

[4] Patrick Ahlrichs, Ralf Everaers, and Burkhard Dunweg. Screening of hydrodynamic interactions in semidilute polymer solutions: A computer simulation study. *Physical Review E*, 64:1–4, 2001.

[5] Ji-Xuan Hou, Carsten Svaneborg, Ralf Everaers, and Gary S. Grest. Stress relaxation in entangled polymer melts. *Physical Review Letters*, 105:068301, 2010.

[6] Cecile A. Dreiss. Wormlike micelles: where do we stand? Recent developments, linear rheology and scattering techniques. *Soft Matter*, 3:956–970, 2007.

[7] Jean-Franois Berret. *Rheology of wormlike micelles: equilibrium properties and shear banding transitions, in: R.G. Weiss, P. Terech (Eds.), Molecular Gels: Materials with Self-Assembled Fibrillar Networks*. Springer, The Netherlands, 1st edition, 2006.

[8] Mike E. Cates and Sauveur-Jean Candau. Statics and dynamics of worm-like surfactant micelles. *Journal of Physics: Condensed Matter*, 2:6869–6892, 1990.

[9] Jiang Yang. Viscoelastic wormlike micelles and their applications. *Current Opinion in Colloid & Interface Science*, 7:267–281, 2002.

[10] Lynn M. Walker. Rheology and structure of worm-like micelles. *Current Opinion in Colloid & Interface Science*, 6:451–456, 2001.

[11] Mike E. Cates. Dynamics of living polymers and flexible surfactant micelles: scaling laws for dilution. *Journal de Physique*, 49:1593–1600, 1988.

[12] Mike E. Cates. Reptation of living polymers: Dynamics of entangled polymers in the presence of reversible chain-scission reactions. *Macromolecules*, 20:2289–2296, 1987.

[13] Mike E. Cates and Suzanne M. Fielding. Rheology of giant micelles. *Advances in Physics*, 55:799–879, 2006.

[14] Johan T. Padding, Edo S. Boek, and Wim J. Briels. Dynamics and rheology of wormlike micelles emerging from particulate computer simulations. *The Journal of Physical Chemistry*, 129:074903, 2008.

[15] Johan T. Padding, Wim J. Briels, Mikhail R. Stukan, and Edo S. Boek. Review of multi-scale particulate simulation of the rheology of wormlike micellar fluids. *Soft Matter*, 5:4367–4375, 2009.

[16] David Lopez-Diaz and Rolando Castillo. Microrheology of solutions embedded with threadlike supramolecular structures. *Soft Matter*, 7:5926, 2011.

[17] Toshiyuki Shikata and Hirotaka Hirata. Micelle formation of detergent molecules in aqueous media: Viscoelastic properties of aqueous cetyltrimethylammonium bromide solutions. *Langmuir*, 3:1081–1086, 1987.

[18] R. Messager, A. Ott, D. Chatenay, W. Urbach, and D. Langevin. Are giant micelles living polymers? *Physical Review Letters*, 60:1410–1413, 1988.

[19] Sauveur-Jean Candau and R. Oda. Linear viscoelasticity of salt-free wormlike micellar solutions. *Colloids and Surfaces A: Physicochemical and Engineering Aspects*, 183-185:5–14, 2001.

[20] Richard D. Koehler, Srinivasa R. Raghavan, and Eric W. Kaler. Microstructure and dynamics of wormlike micellar solutions formed by mixing cationic and anionic surfactants. *The Journal of Physical Chemistry B*, 104:11035–11044, 2000.

[21] Richard D. Koehler, Srinivasa R. Raghavan, and Eric W. Kaler. Microstructure and dynamics of wormlike micellar solutions formed by mixing cationic and anionic surfactants. *The Journal of Physical Chemistry B*, 104:11035–11044, 2000.

[22] Peter Fischer, Heinz Rehage, and Burghard Gruning. Linear flow properties of dimer acid betaine solutions with and without changed ionic strength. *The Journal of Physical Chemistry B*, 106:11041–11046, 2002.

[23] Heinz Rehage and Heinz Hoffmann. Rheological properties of viscoelastic surfactant systems. *The Journal of Physical Chemistry.*, 92:4712–4719, 1988.

[24] E. Cappelaere, Jean-Francois Berret, Jean-Paul Decruppe, R. Cressely, and Peter Lindner. Rheology, birefringence, and small-angle neutron scattering in a charged micellar system: Evidence of a shear-induced phase transition. *Physical Review E*, 56:1869–1978, 1997.

[25] Sauveur-Jean Candau, E. Hirsch, R. Zana, and M. Delsanti. Rheological properties of semidilute and concentrated aqueous solutions of cetyltrimethylammonium bromide in the presence of potassium bromide. *Langmuir*, 183-185:1225–1229, 1989.

[26] Ze Lin, J J. Cai, L E. Scriven, and H. Ted Davis. Spherical-to-wormlike micelle transition in CTAB solutions. *The Journal of Physical Chemistry*, 98:5984–5993, 1997.

[27] Kelly R. Francisco, Marcelo A. da Silva, Edvaldo Sabadini, Gran Karlsson, and Cecile A. Dreiss c. Effect of monomeric and polymeric co-solutes on cetyltrimethylammonium bromide wormlike micelles: Rheology, Cryo-TEM and small-angle neutron scattering. *Journal of Colloid and Interface Science*, 345:351–359, 2010.

[28] Toshiyuki Shikata, Hirotaka Hirata, Eiichi Takatori, and Kunihiro Osaki. Nonlinear viscoelastic behavior of aqueous detergent solutions. *Journal of Non-Newtonian Fluid Mechanics*, 28:171–182, 1988.

[29] Peter Schurtenberger, oger Scartazzini, Linda J. Magid, Martin E. Leser, and Pier Luigi Luis. Structural and dynamic properties of polymer-like reverse micelles. *The Journal of Physical Chemistry*, 94:3695–3701, 1990.

[30] Ulf Olsson, Johan Borjesson, Ruggero Angelico, Andrea Ceglie, and Gerardo Palazzo. Slow dynamics of wormlike micelles. *Soft Matter*, 6:1769–1777, 2010.

[31] Tanner S. Davies, Aimee, M. Ketner, and Srinivasa R. Raghavan. Self-assembly of surfactant vesicles that transform into viscoelastic wormlike micelles upon heating. *Journal of the American Chemical Society*, 56:6669–6675, 2006.

[32] Samiul Amin, Thomas W. Kermis, Ryan M. van Zanten, Stephen J. Dees, and John H. van Zanten. Concentration fluctuations in CTAB/NaSal solutions. *Langmuir*, 17:8055–8061, 2001.

[33] Francois Quirion. Growth and counterion binding of cetyltrimethylammonium bromide aggregates at 25 $^{\circ}c$: A neutron and light scattering study. *The Journal of Physical Chemistry*, 90:5435–5441, 1986.

[34] Erick Sarmiento-Gomez, David Lopez-Diaz, and Rolando Castillo. Microrheology and characteristic lengths in wormlike micelles made of a zwitterionic surfactant and SDS in brine. *The Journal of Physical Chemistry B*, 114:12193–12202, 2010.

[35] Peter Schurtenberger and Carolina Cavaco. Polymer-like lecithin reverse micelles. 1. a light scattering study. *Langmuir*, 10:100–108, 1994.

[36] Peter Schurtenberger, Gotz Jerke, and Carolina Cavaco. Cross-section structure of cylindrical and polymer-like micelles from small-angle scattering data. 2. experimental results. *Langmuir*, 12:2433–2440, 1996.

[37] Stephan Forster, M. Konrad, and Peter Lindner. Shear thinning and orientational ordering of wormlike micelles. *Physical Review Letters*, 94:017803, 2005.

[38] Ruggero Angelico, Gerardo Palazzo, Giuseppe Colafemmina, Peter A. Cirkel, Mauro Giustini, and Andrea Ceglie. Water diffusion and headgroup mobility in polymer-like reverse micelles: Evidence of a sphere-to-rod-to-sphere transition. *The Journal of Physical Chemistry B*, 102:2883–2889, 1998.

[39] Suliman Barhoum and Anand Yethiraj. An NMR study of macromolecular aggregation in a model polymer-surfactant solution. *The Journal of Chemical Physics*, 132:19, 2010.

[40] William S. Price, Fumihiko Tsuchiya, and Yoji Arata. Lysozyme aggregation and solution properties studied using PGSE NMR diffusion measurements. *Journal of the American Chemical Society*, 121:11503–11512, 1999.

[41] Suliman Barhoum and Anand Yethiraj. NMR detection of an equilibrium phase consisting of monomers and clusters in concentrated lysozyme solutions. *The Journal of Physical Chemistry B*, 114:17062–17067, 2010.

[42] David Lopez-Diaz, Erick Sarmiento-Gomez, Cristina Garza, and Rolando Castillo. A rheological study in the dilute regime of the worm-micelle fluid made of zwitterionic surfactant (TDPS), anionic surfactant (SDS), and brine. *Journal of Colloid and Interface Science*, 348:152–158, 2010.

[43] David Lopez-Diaz and Rolando Castillo. The wormlike micellar solution made of a zwitterionic surfactant (TDPS), an anionic surfactant (SDS), and brine in the semidilute regime. *The Journal of Physical Chemistry B*, 114:8917–8925, 2010.

[44] James Keeler. *Understanding NMR Spectroscopy*. John Wiley & Sons Ltd, Chichester, 1st edition, 2005.

[45] William S. Price. Pulsed-field gradient nuclear magnetic resonance as a tool for studying translational diffusion: Part I. basic theory. *Concepts in Magnetic Resonance*, 9:299–336, 1997.

[46] William S. Price. Pulsed-field gradient nuclear magnetic resonance as a tool for studying translational diffusion: Part II. experimental aspects. *Concepts in Magnetic Resonance*, 10:197–237, 1997.

[47] H. Zeng, Bostjan Zalar, Germano S. Iannacchione, and D. Finotello. *Effects of quenched disorder on the orientational order of the octylcyanobiphenyl liquid crystal, in: Roland Y. Dong, Nuclear Magnetic Resonance Spectroscopy of Liquid Crystals*. World Scientific Publishing Co. Pte. Ltd, USA, 1st edition, 2009.

[48] Malcolm H. Levitt. *Spin Dynamics*. John Wiley & Sons, Chichester, 2nd edition, 2008.

[49] Anand Yethiraj, Donatella Capitani, Nicholas E. Burlinson, and E. Elliott Burnell. An NMR study of translational diffusion and structural anisotropy in magnetically alignable nonionic surfactant mesophases. *Langmuir*, 21:3311–3321, 2005.

[50] Ruggero Angelico, Ulf Olsson, Gerardo Palazzo, and Andrea Ceglie. Surfactant curvilinear diffusion in giant wormlike micelles. *Physical Review Letters.*, 81:2823–2826, 1998.

[51] Anindya Das, Sundaresan Jayanthi, Handiganadu Srinivasa Murthy Vinay Deepak, Krishna Venkatachala Ramanathan, Anil Kumar, Chandan Dasgupta, and Ajay K. Sood. Single-file diffusion of confined water inside SWNTs: An NMR study. *ACS NANO*, 4:1687–1695, 2010.

[52] Paul T. Callaghan. *Principles of Nuclear Magnetic Resonance Microscopy*. Clarendon Press. Oxford, New York, 1st edition, 1991.

[53] P. Fischer and H. Rehage. Rheological master curves of viscoelastic surfactant solutions by varying the solvent viscosity and temperature. *Langmuir*, 13:7012–7020, 1997.

[54] R. Leberman and Alan K. Soper. Effect of high salt concentrations on water structure. *Nature*, 378:364–366, 1995.

Chapter 6

NMR Detection of an Equilibrium Phase Consisting of Monomers and Clusters in Concentrated Lysozyme Solutions

6.1 Abstract

Protein aggregation is an important biophysical phenomenon, and it is technically challenging to quantify. Scattering studies in concentrated protein solutions are not in complete agreement over the existence of an equilibrium cluster phase. We use pulsed-field-gradient NMR spectroscopy to characterize diffusion in the long-time limit in concentrated lysozyme solutions, and find strong evidence for the existence of an equilibrium phase that consists of both lysozyme monomers and clusters (aggregates). They indicate too that there is rapid exchange between monomer and aggregate on the NMR timescale, and that macroscopic measurables (e.g., the relaxation rate and

the observed diffusion coefficient) reflect a weighted average of the two fractions. Our results are quantitatively compared, with no fit parameters, to simple theories of macromolecular crowding.[1]

6.2 Introduction

The interactions of proteins in water is important in many biophysical processes. Concentrated solutions of protein exhibit a tendency to self-associate to form aggregates.[2] This phenomenon is important because many human proteins have segments that can form amyloid aggregates,[3] which are implicated in the root causes of many "conformational diseases".[4,5] On the other hand, much can be learned about structure and conformations of proteins in solution by treating them as polymeric colloidal suspensions,[6] with a phase behavior that includes liquid-liquid phase separation[7] and the formation of crystalline aggregates.[8,9] Dynamics in concentrated protein solutions is also complicated by effects of macromolecular crowding.[2,10] This too can be modeled in analogy with behavior in dense colloidal suspensions.[11,12]

For this reason, the aggregation of lysozyme solutions has been studied extensively using scattering techniques,[13–19] nuclear magnetic resonance,[8,9,17,20] and computer simulations.[21,22] Lysozyme solutions in the concentrated regime have been shown to exhibit metastable liquid-liquid phase segregation[7,23] that is in some cases followed by crystallization and precipitation.[7,8,19,20] Aggregates detected in solution in the latter studies are transient aggregates.

However, small-angle scattering studies have reported too that concentrated lysozyme solutions form not only transient aggregates but also a stable equilibrium phase consisting of both individual proteins (referred to here as "monomers") as well as clusters.[13,14] Parameters like temperature, salt concentration, and pH were found to play a role in changing cluster size and cluster density.[13,14] These results provide support for a colloidal model to understand the phase behaviour of lysozyme,[24] with the generic feature of long-range repulsions and short-range attractions yielding the possibility for complex gel and glass phases in lysozyme solutions.[25]

The small-angle scattering evidence for equilibrium clusters is based on one interpretation of the interference peak observed at low scattering vectors. A second small-angle scattering study,[15] which also observes an interference peak, however attributes it to interactions of individual monomers. In addition, a recent small-angle neutron scattering and neutron spin echo study has proposed a scenario that invokes the existence of clusters ("dynamic clusters") but with macroscopic properties in the long time limit that are determined by monomeric proteins.[16] Thus scattering studies[13,15,16,26] are still not in complete agreement on the existence of an equilibrium cluster phase.

In this context, we present an NMR study in concentrated lysozyme solutions that provides quantitative and independent evidence, in the long time limit, for an equilibrium phase that consists of fractions of protein monomers and fractions of aggregates or clusters. We find too that proteins exchange rapidly between monomer and cluster form on the NMR timescale. The NMR signal is a weighted average of the different fractions, and the macroscopic properties are governed by this weighted average. Monomer diffusion coefficients are compared with theoretical models for long-time self diffusion in crowded solutions: good agreement is found with the model of Han and Herzfeld.[11]

6.3   Experimental

Hen egg white lysozyme with 14,600 average molecular mass and HEPES buffer were purchased from Sigma-Aldrich Canada. We prepared 20 mM HEPES buffer solution in D_2O at pH $\approx$ 7.5, and used it to prepare lysozyme stock solution with 40 mg/ml lysozyme concentration. The lysozyme stock solution was stirred and filtered using a 0.22 μm filter to remove undissolved material. A centrifugal filter device with a YM-10 membrane was used to concentrate the lysozyme stock solution more. This high concentration lysozyme stock solution was diluted with the 20 mM HEPES buffer solution to prepare the lysozyme samples (batch 1, prepared from 274 mg/ml stock

solution: 14 mg/ml, 36 mg/ml, 169 mg/ml, and 245 mg/ml; batch 2, prepared from 247 mg/ml stock solution: 70 mg/ml and 100 mg/ml; batch 3, prepared from 274 mg/ml stock solution: 93 mg/ml). The lysozyme concentration was measured after preparation via the absorbance at $\lambda = 595$ nm[27] using a UV-visible spectroscometer. In increasing order, these concentrations resulted in lysozyme volume fractions of $\Phi = 0.012, 0.031, 0.059, 0.079, 0.085, 0.143$ and 0.215.

Figure 6.1a shows the one-dimensional NMR spectrum of the highest lysozyme concentration sample $C = 254$ mg/ml in an aqueous solution, while figure 6.1b shows the Fourier transform of a pulsed gradient stimulated echo at a gradient strength where the water and HEPES signals are completely attenuated, leaving only the lysozyme spectrum. NMR experiments were carried out on a 600 MHz Bruker Avance II spectrometer equipped with a Micro-5 imaging (3-axis gradient) probe with a maximum gradient strength of 200 G/cm (2 T/m). Unless otherwise stated, all NMR experiments were performed at T = 298 K.


(a)   (b)
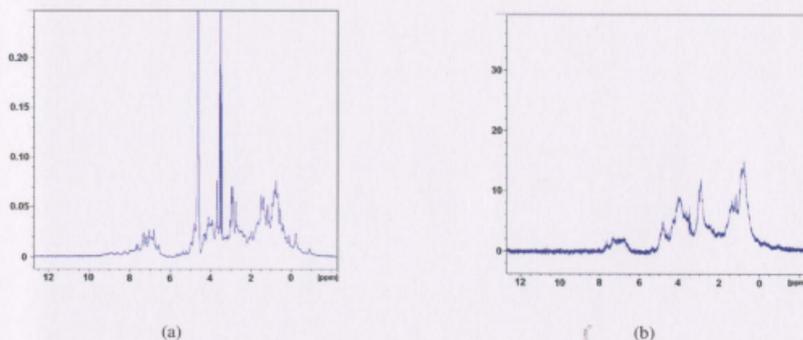
Figure 6.1: Lysozyme(254 mg/ml)/HEPES/D_2O, sample temperature 298 K. (a) ^1H – NMR one-dimensional (1D) spectrum of sample. (b) ^1H – NMR 1D spectrum after a pulsed-gradient stimulated echo ($\Delta = 100$ ms, gradient strength = 0.62 T/m).

The self-diffusion results were obtained with a pulsed field gradient stimulated-echo sequence

with (almost square) trapezoidal gradient pulses. The diffusion coefficient of the lysozyme species in aqueous solution is obtained from the attenuation of the signal according to:[28]

$$\ln\left(\frac{S(k)}{S(0)}\right) = -Dk \tag{6.1}$$

where S(k) is the "intensity" of the signal (the integration of the relevant peak region) in the presence of field gradient pulse, S(0) is the intensity of the signal in the absence of field gradient pulse, $k = (\gamma \delta g)^2 (\Delta - \delta/3)$ is a generalized gradient strength parameter, g is the amplitude of the field gradient pulse, $\gamma = \gamma^H = 2.6571 \times 10^8$ T^{-1}.s^{-1} is the gyromagnetic ratio of the ^{1}H nucleus, $\delta = 2$ ms is the duration of the field gradient pulse, and Δ is the time period between the two field gradient pulses which was varied from 50ms to 700 ms.

The relaxation measurements were also performed using the imaging probe. The inversion recovery technique with 16 time delays t was used to measure T_1, and the intensity data of lysozyme peaks in the region between 6.5 to 9.5 ppm were fit to the equation $I(t) = I_0\left(1 - 2\exp\left(\frac{-t}{T_1}\right)\right)$. A series of $16\ (\frac{\pi}{2})_x - t/2 - (\pi)_x - t/2$ - acquire spin echo experiments with varying delay times t was used to measure T_2, obtained similarly from a fit of the intensities to the equation $I(t) = I_0\exp\left(\frac{-t}{T_2}\right)$.

6.4 Results and Discussion

6.4.1 Crowded Diffusion

Figure 6.2a shows a multi-exponential attenuation in the signal which is due to the existence of water and HEPES molecules in the solution in addition to lysozyme species. The early linear (small k) and later linear (large k) parts in the signal attenuation have distinct spectral signatures that overlap in chemical shift but are separable in the field-gradient dimension (figure 6.1). The linear regime at large k corresponds to the signal attenuation associated with lysozyme peaks in the spectrum, which is mono-exponential. This is consistent also with relaxation results where the

153
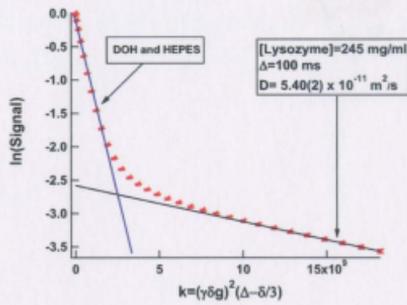
(a)
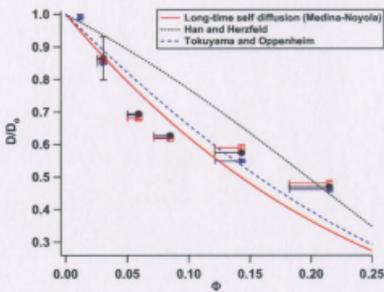
(b)
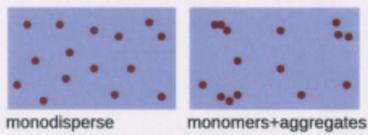
(c)

Figure 6.2: (a)The attenuation of the signal S(k)/S(0) on a log scale versus $k = (\gamma \delta g)^2 (\Delta - \delta/3)$ for 254 mg/ml ($\Phi = 0.215$) lysozyme concentration and with Δ=100 ms. The black line shows the attenuation in signal of lysozyme peaks. The blue line shows the attenuation in signal of DOH and HEPES peaks. (b) Lysozyme self-diffusion coefficient D (scaled by the theoretical value at zero concentration[20,29] at diffusion times Δ= 50, 100, and 150 ms versus lysozyme volume fraction Φ. Dashed lines are long-time self-diffusion coefficients obtained in the works of Medina-Noyola,[30,31] Tokuyama and Oppenheim[12] and Han and Herzfeld.[11] Volume fraction error bars (left error bars). (c) Illustration of the effect of aggregate formation on the free volume seen by monomers.

154

time dependence of the lysozyme signal attenuation exhibits a single relaxation time.

Figure 6.2b shows the variation of the lysozyme self-diffusion coefficient D at diffusion time $\Delta = 50$, 100, and 150 ms as a function of lysozyme volume fraction:

$$\Phi = C \times \left(\frac{N_A \times \left(\frac{4\pi R^3}{3} \right)}{M_w} \right) \times 10^3 \approx C \times 0.85 \times 10^{-3} \tag{6.2}$$

treating the globular protein lysozyme as an ellipsoid with dimensions $a = b = 15$ Å and $c = 22.5$ Å,[32] leading to hydrodynamic radius $R = (abc)^{1/3} \approx 17$ Å. In equation 6.2 N_A is the Avogadro number and M_W is the molecular weight of lysozyme. If one used instead the specific volume of lysozyme,[33] one gets a lower value of volume fraction $\Phi = C \times 0.717 \times 10^{-3}$. The uncertainty in volume fraction reflects a systematic difference in the calculation of volume fraction based on the bare lysozyme volume (lower value) and the volume fraction deduced from the hydrodynamic radius of the lysozyme molecule. The diffusion coefficients are scaled by the theoretical value at zero concentration $D_0 = 11.7 \times 10^{-11}$ m^2/s[20] which employs an anisotropy correction to the calculation for spheres.[29]

Figure 6.2b shows that the lysozyme self-diffusion coefficient D increases with decreasing lysozyme volume fraction Φ. Also plotted are the long-time self-diffusion coefficient according to Tokuyama and Oppenheim,[12] Medina-Noyola[30] (using the formula obtained in van Blaaderen et al.[31]) and Han and Herzfeld[11] (using the self-consistent value $\Delta r/R = 2/3$) - we would expect the experiments to be closest to the model values for low volume fractions of lysozyme in solution where aggregate formation is least important. For $\Phi < 0.1$, the Medina-Noyola form appears to be closest to the observed diffusion coefficient results for lysozyme. The Medina-Noyola and Tokuyama-Oppenheim theoretical curves underestimate the diffusion coefficients at higher volume fractions; this fact has been noted before[20] and can be understood simply as follows:

- The observed diffusion coefficient is a relaxation-weighted average of monomer and aggregate diffusion, as expressed in equation 6.4. This alone would indicate that the observed

155

diffusion coefficient is a lower bound for the monomer diffusion.

- When there are aggregates, the calculated volume fraction reflects an underestimation of the free volume and an overestimation of the effective volume fraction seen by the monomers. This latter point is illustrated in the cartoon (figure 6.2c).

We revisit the comparison of experimental diffusion coefficients with theory after a more careful analysis of the effects of relaxation weighting on the observed diffusion coefficients.

6.4.2 Relaxation Rates

Figure 6.3a and figure 6.3b show the variation of longitudinal relaxation rate R_1 ($=1/T_1$) and transverse relaxation rate R_2 ($=1/T_2$) respectively as a function of reciprocal lysozyme concentration $1/C$. Based on the assumption that the lysozyme molecules coexist with lysozyme aggregates especially at high lysozyme concentration, the observed relaxation rates R_i (i.e R_1 and R_2) include contributions from both the aggregate relaxation rate $R_{i,a}$ and the monomeric relaxation rate $R_{i,m}$. Therefore, the observed relaxation rates R_1 and R_2 may be written

$$R_i = bR_{i,m} + (1 - b)R_{i,a} \qquad (6.3)$$

where $R_{i,m}$ and $R_{i,a}$ are $R_{1,m}$ or $R_{2,m}$ and $R_{1,a}$ or $R_{2,a}$, and $b = C_m/C$ is the fraction of the free lysozyme monomers, and C_m is the free monomer concentration.

Parts a and b of figure 6.3 are clearly not a linear function of $\frac{1}{C}$ (equation 6.3). In simpler micelle- and aggregate-forming systems (such as SDS and PEO-SDS solutions[34]) there is a linear dependence of the relaxation rates on $\frac{1}{C}$, this implies that the concentration of free monomers is a constant above a critical aggregation concentration. In this system, the free fraction of monomers is itself a function of C.

156
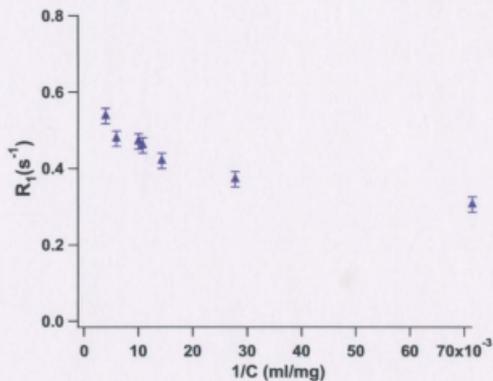
(a)
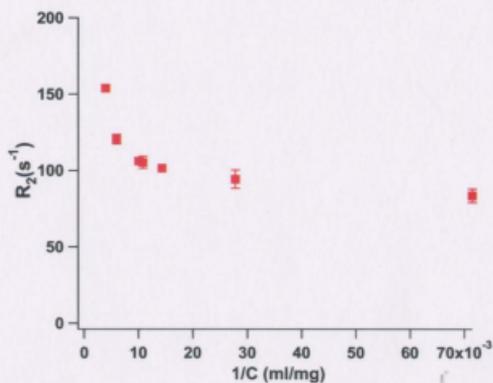
(b)

Figure 6.3: (a) Proton longitudinal relaxation rates R_1 and (b) transverse relaxation rates R_2 versus reciprocal of lysozyme concentration $1/C$. Both relaxation rates show a systematic decrease as a function of $1/C$.
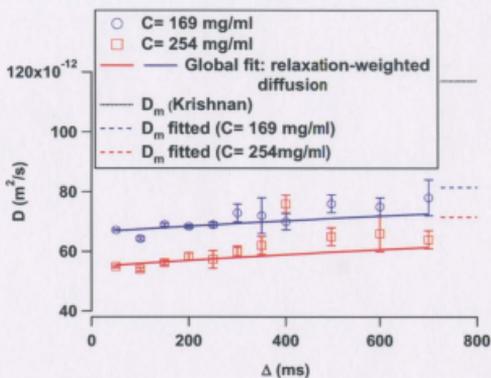
(a)
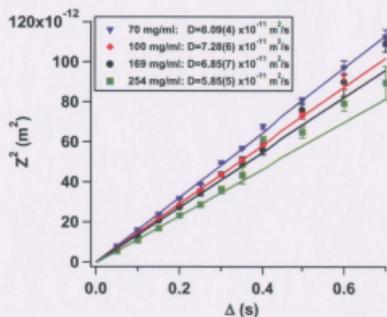
(b)

Figure 6.4: (a) Lysozyme self-diffusion coefficient D versus diffusion time Δ for lysozyme concentrations C = 169 mg/ml ($\Phi = 0.143$) and 254 mg/ml ($\Phi = 0.215$). The values of D_m obtained from the fit are shown to the right of the data. (b) Mean-squared displacement $z^2 = 2D\Delta$ as a function of Δ for C = 70, 100, 169, and 254 mg/ml.

6.4.3 Fraction of Protein Monomers and Clusters

Figure 6.4a shows the variation of lysozyme self-diffusion coefficient D at two different lysozyme concentrations (C= 169 mg/ml and 254 mg/ml) as a function of the diffusion time Δ. At lower concentrations, we have limited signal at high Δ. At all concentrations, the signal attenuation of lysozyme peaks is mono-exponential over the range of diffusion time Δ probed (not shown). The lysozyme self-diffusion coefficient shows a small but unambiguous increase with diffusion time for both C = 169 mg/ml and 254 mg/ml.

Figure 6.2b shows that in the time scale of the NMR experiment we are already accessing the long time self diffusion coefficient of lysozyme at $\Delta = 50$ ms. Therefore for a monodisperse system of lysozyme proteins we would not expect D to show a dependence of Δ for $\Delta > 50$ ms. In addition, if we were not in the long-time limit, we would expect to see a *decrease* not an increase.[35] However if the lysozyme exists in monomeric form and in clusters, then these two states would be expected to have different microscopic correlation times: shorter for monomers and longer for aggregates. Then the observed diffusion coefficients from a pulsed-gradient stimulated echo would be a (longitudinal) relaxation weighted average of the monomer and the aggregate diffusion coefficient.[8,20] Thus, the observed lysozyme self-diffusion coefficient D can be written in the form

$$D = \frac{bD_m \exp(-R_{1,m}\Delta) + (1-b)D_a \exp(-R_{1,a}\Delta)}{b \exp(-R_{1,m}\Delta) + (1-b)\exp(-R_{1,a}\Delta)} \qquad (6.4)$$

where from equation 6.3, $b = (R_1 - R_{1,a})/(R_{1,m} - R_{1,a})$. By globally fitting the diffusion curves of both C = 169 mg/ml and 254 mg/ml to equation 6.4, we are able to calculate the monomer and aggregate relaxation rates ($R_{1,m} \approx 0.30(4)$ s^{-1}, $R_{1,a} \approx 1.2(1)$ s^{-1}, and $D_a \approx 8(8)\times10^{-12}$ m^2/s). There is a large uncertainty in D_a. We can say unambiguously, however, that $D_a << D_m$. An alternative approach is to calculate the mean-squared displacement $z^2 = 2D\Delta$ (ignoring the effects of relaxation weighting, figure 6.4b). The slope in figure 6.4b yields a reasonable estimate (although, comparing with the fit to figure 6.4a, in fact an underestimate of about 10% at higher concentrations) of the monomer diffusion coefficient.

From the monomer and aggregate relaxation rates ($R_{1,m}$ and $R_{1,a}$) and the measured relaxation rates R_1, we can obtain (equation 6.3) the fraction b of lysozyme free monomers in the solution and the fraction $(1 - b)$ of lysozyme molecules in the aggregate state for all samples; figure 6.5a shows that the fraction b of free lysozyme monomers decreases by increasing the concentration, while the fraction $(1 - b)$ of lysozyme monomers in the aggregate state increases with increasing concentration. At large concentrations, approximately 25% of lysozyme molecules are in the aggregate state. Using equation 6.4 and the calculated $R_{1,m}$, $R_{1,a}$, and D_a at $\Delta = 100$ ms, we calculate the scaled lysozyme monomeric diffusion coefficient D_m/D_0 at different lysozyme volume fractions Φ (figure 6.5b). A rough estimate of the error in D_m/D_0 is obtained from the errors in the global fitting. The Φ dependence of the monomer diffusion coefficients exhibit reasonable agreement with the theoretical results of Han and Herzfeld up to $\Phi \approx 0.15$.

From the fit to the diffusometry results, we can plot the longitudinal relaxation rate R_1 and transverse relaxation rate R_2 respectively as a function of the fraction b of free lysozyme monomers (not shown). By fitting both curves to equation 6.3, we are able to calculate the longitudinal and transverse relaxation rates of lysozyme monomer and aggregate. While $R_{1,m} = 0.29(7)$ s^{-1} and $R_{1,a} = 1.2(3)$s^{-1} (for the monomer and aggregate) are simply restating the results of the global fitting in equation 6.4, we are also able to obtain the corresponding transverse relaxation rates ($R_{2,m} = 75(6)$ s^{-1} and $R_{2,a} = 325(25)$ s^{-1}).

The relaxation rate and the diffusion measurements for 254 mg/ml lysozyme sample have been done at three different temperatures 298, 288, and 278 K. Figure 6.6a and figure 6.6b show the variation of longitudinal R_1 relaxation rate, transverse R_2 relaxation rate, and the diffusion coefficient respectively as a function of temperature. The relaxation rates R_1 and R_2 increase as the temperature decreases, while the diffusion coefficient shows a decrease as the temperature decreases. This too is consistent with the fraction of lysozyme aggregate increasing with decreasing lysozyme solution temperature.
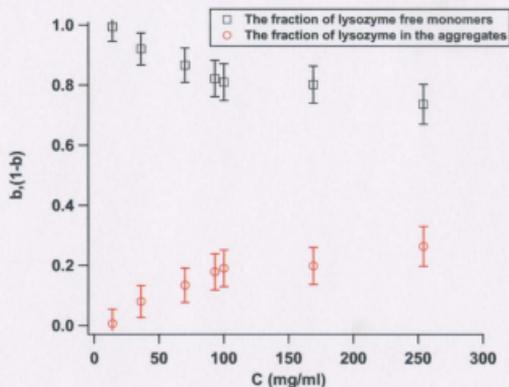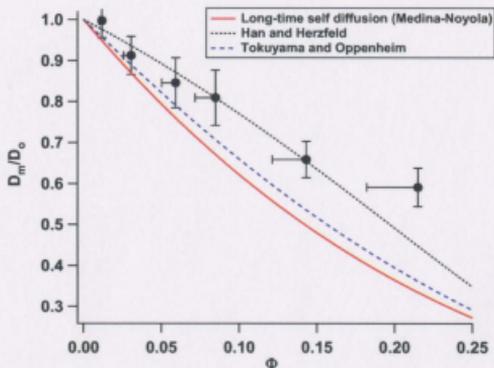
Figure 6.5: (a) The fraction b of lysozyme free monomers and the fraction (1 − b) of lysozyme monomers in the aggregates versus lysozyme concentration C (b) Monomeric self-diffusion coefficient D_m/D_0 (scaled by the theoretical value at zero concentration[20,29]) at $\Delta= 100$ ms versus lysozyme volume fraction Φ. Dashed lines are long-time self-diffusion coefficients obtained in the works of Medina-Noyola,[30,31] Tokuyama and Oppenheim[12] and Han and Herzfeld.[11]

161
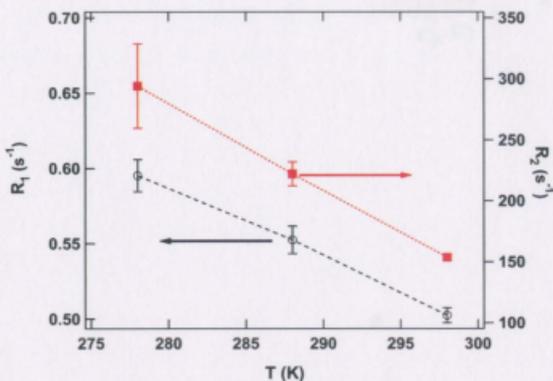
(a)
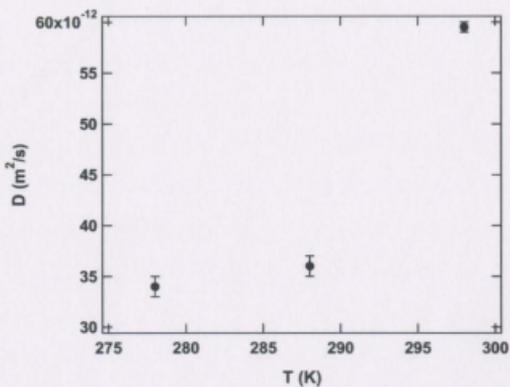
(b)

Figure 6.6: (a) Relaxation rates R_1 (open circles, left scale) and R_2 (filled squares, right scale) versus temperature T. (b) Lysozyme diffusion coefficient D versus temperature. C = 254 mg/ml.

6.5 Conclusion

We have carried out NMR relaxometry and diffusometry experiments on concentrated lysozyme solutions. Mono-exponential dependence of the NMR signal on the delay time in the inversion

recovery and spin echo experiments suggest that if there are multiple species in solution they must be exchanging rapidly on the NMR timescale. Both longitudinal and transverse relaxation rates show a sharp increase with increasing concentration, suggesting the increased contribution to the signal from lysozyme clusters or aggregates.

Diffusometry as a function of lysozyme volume fraction Φ agreems with simple colloidal models for macromolecular crowding for $\Phi < 0.1$, with no fit parameters. At higher volume fractions or concentrations, there is a marked deviation, again pointing to the role of aggregates. All the models underestimate the observed diffusion coefficients for large Φ. A simple picture for this is that the formation of aggregates creates more free volume for the monomers.

The dependence of diffusion coefficient on diffusion time Δ provides quantitative evidence of aggregates. Prior to approaching the long-time self-diffusion limit, one would expect a decrease in D with increasing Δ. Given that the experiments are clearly in the long-time limit ($\tau_{Brownian} \sim 40$ ns $<< \Delta$) , one would naively expect no Δ dependence for a monodisperse system. The presence of aggregates (with a relaxation rate larger than that of monomers) results in the observed diffusion coefficients being a relaxation-weighted average of monomer and aggregate diffusion. Unique to NMR is the fact that microscopic molecular correlation times in the picosecond to nanosecond window lead to relaxation times in the millisecond to second window, where one is probing long-time self diffusion. Putting together both diffusion measurements (e.g., figure 6.4a) and relaxation measurements, we were able to calculate the relaxation rates of lysozyme in the monomer and the aggregate state.

In addition, we obtained from the fit in figure 6.4a the self-diffusion coefficient of lysozyme monomers D_m as a function of volume fraction, as well as of the aggregates D_a. The monomeric diffusion coefficient is in rather good agreement with simulations of crowded diffusion of model proteins (Han and Herzfeld[11]). The value obtained for aggregate diffusion is $D_a \approx 8 \times 10^{-12}$ m^2/s. If the clusters were compact and freely diffusing, this implies an aggregate size of $9R_0$, about 2-3 times larger than the values deduced by Porcar et al.[16] and Stradner et al.[13] A possibility that

is consistent with our experiments and with the picture of an equilibrium cluster phase driven by competition between short range attraction and long range repulsion (as suggested by Stradner et al[13]) is that the clusters are not tightly bound oligomers but instead form loose percolating networks at higher density coexisting with, and exchanging with, monomers at lower densities. This has been observed in colloidal systems.[36] Finally, we quantified (figure 6.5a) the fraction b and $1 - b$ of free monomers and aggregates over the entire range of lysozyme concentration. Above $C = 100$ mg/ml (at $T = 298$ K), the aggregate state constitutes a fraction of roughly 20 - 25% of the proteins in solution, this fraction increases with decreasing T. The macroscopic properties of the long-time limit are therefore governed by a weighted average of monomeric and aggregate properties.

Bibliography

[1] Suliman Barhoum and Anand Yethiraj. NMR detection of an equilibrium phase consisting of monomers and clusters in concentrated lysozyme solutions. *The Journal of Physical Chemistry B*, 114:17062–17067, 2010.

[2] Duncan A. White, Alexander K. Buell, Tuomas P. J. Knowles, Mark E. Welland, and Christopher M. Dobson. Protein aggregation in crowded environments. *Journal of the American Chemical Society*, 132:5170–5175, 2010.

[3] Jim Schnabel. Protein folding: The dark side of proteins. *Nature*, 464:828–829, 2010.

[4] Ron R. Kopito and David Ron. Conformational disease. *Nature Cell Biology*, 2:E207–E209, 2000.

[5] Adriano Aguzzi and Tracy O'Connor. Protein aggregation diseases: pathogenicity and therapeutic perspectives. *Nature Reviews Drug Discovery*, 9:237–248, 2010.

[6] Adrian H. Elcock, David Sept, and J. Andrew McCammon. Computer simulation of protein-protein interactions. *The Journal of Physical Chemistry B*, 105:1504–1518, 2001.

[7] Martin Muschol and Franz Rosenberger. Liquid-liquid phase separation in supersaturated lysozyme solutions and associated precipitate formation/crystallization. *The Journal of Chemical Physics*, 107:1953–1962, 1997.

[8] William S. Price, Fumihiko Tsuchiya, and Yoji Arata. Time dependence of aggregation in crystallizing lysozyme solutions probed using NMR self-diffusion measurements. *Biophysical Journal*, 80:15851590, 2001.

[9] Elena Ilyina, Vikram Roongta, Hong Pan, Clare Woodward, and Kevin H. Mayo. A pulsed-field gradient NMR study of bovine pancreatic trypsin inhibitor self-association. *The Journal of Biochemistry*, 36:3383–3388, 1997.

[10] Allen P. Minton. Implications of macromolecular crowding for protein assembly. *Current Opinion in Structural Biology*, 10:34–39, 2000.

[11] Jining Han and Judith Herzfeld. Macromolecular diffusion in crowded solutions. *Biophysical Journal*, 65:1155–1161, 1993.

[12] Michio Tokuyama and Irwin Oppenheim. Dynamics of hard-sphere suspensions. *Physical Review E*, 50:R16–R19, 1994.

[13] Anna Stradner, Helen Sedgwick, Frederic Cardinaux, Wilson C. K. Poon, Stefan U. Egelhaaf, and Peter Schurtenberger. Equilibrium cluster formation in concentrated protein solutions and colloids. *Nature*, 432:492–495, 2004.

[14] Anna Stradner, Frederic Cardinaux, and Peter Schurtenberger. A small-angle scattering study on equilibrium clusters in lysozyme solutions. *The Journal of Physical Chemistry B*, 110:21222–21231, 2006.

[15] Anuj Shukla, Efstratios Mylonas, Emanuela Di Cola, Stephanie Finet, Peter Timmins, Theyencheri Narayanan, and Dmitri I. Svergun. Absence of equilibrium cluster phase in concentrated lysozyme solutions. *Proceedings of the National Academy of Sciences*, 105:5075–5080, 2008.

[16] Lionel Porcar, Peter Falus, Wei-Ren Chen, Antonio Faraone, Emiliano Fratini, Kunlun Hong, Piero Baglioni, and Yun Liu. Formation of the dynamic clusters in concentrated lysozyme protein solutions. *The Journal of Physical Chemistry Letters*, 1:126129, 2009.

[17] Jaroslaw Poznanski, Jedrzej Szymanski, Teresa Basinska, Stanislaw Slomkowski, and Wojciech Zielenkiewicz. Aggregation of aqueous lysozyme solutions followed by dynamic light scattering and ^{1}H NMR spectroscopy. *Journal of Molecular Liquids*, 121:21–26, 2005.

[18] Yun Liu, Emiliano Fratini, Piero Baglioni, Wei-Ren Chen, and Sow-Hsin Chen. Effective long-range attraction between protein molecules in solutions studied by small angle neutron scattering. *Physical Review Letters*, 95(118102):1–4, 2005.

[19] N. Niimura, Y. Minezaki, M. Ataka, and T. Katsura. Aggregation in supersaturated lysozyme solution studied by time-resolved small angle neutron scattering. *Journal of Crystal Growth*, 154:136–144, 1995.

[20] William S. Price, Fumihiko Tsuchiya, and Yoji Arata. Lysozyme aggregation and solution properties studied using PGSE NMR diffusion measurements. *Journal of the American Chemical Society*, 121:11503–11512, 1999.

[21] Sean R. McGuffee, , and Adrian H. Elcock. Atomically detailed simulations of concentrated protein solutions: The effects of salt, pH, point mutations, and protein concentration in simulations of 1000-molecule systems. *Journal of the American Chemical Society*, 128:12098–12110, 2006.

[22] Fredrik Carlsson, Martin Malmsten, and Per Linse. Monte carlo simulations of lysozyme self-association in aqueous solution. *The Journal of Physical Chemistry B*, 105:12189–12195, 2001.

[23] Victor G. Taratuta, Andreas Holschbach, George M. Thurston, Daniel Blankschtein, and George B. Benedek. Liquid-liquid phase separation of aqueous lysozyme solutlons: Effects of pH and salt identity. *The Journal of Physical Chemistry*, 94:2140–2144, 1990.

[24] Christoph Gögelein, Gerhard Nägele, Remco Tuinier, Thomas Gibaud, Anna Stradner, and Peter Schurtenberger. A simple patchy colloid model for the phase behavior of lysozyme dispersions. *The Journal of Chemical Physics*, 129:085102, 2008.

[25] Frederic Cardinaux, Thomas Gibaud, Anna Stradner, and Peter Schurtenberger. Interplay between spinodal decomposition and glass formation in proteins exhibiting short-range attractions. *Physical Review Letters*, 99:118301, 2007.

[26] Jill Trewhella. The different views from small angles. *Proceedings of the National Academy of Sciences*, 105:49674968, 2008.

[27] Marion M. Bradford. A rapid and sensitive method for the quantitation of microgram quantities of protein utilizing the principle of protein-dye binding. *Analytical Biochemistry*, 72:248–254, 1976.

[28] William S. Price. Pulsed-field gradient nuclear magnetic resonance as a tool for studying translational diffusion: Part I. basic theory. *Concepts in Magnetic Resonance*, 9:299–336, 1997.

[29] V. V. Krishnan. Determination of oligomeric state of proteins in solution from pulsed-field-gradient self-diffusion coefficient measurements. a comparison of experimental, theoretical, and hard-sphere approximated values. *Journal of Magnetic Resonance*, 124:468–473, 1997.

[30] Magdaleno Medina-Noyola. Long-time self-diffusion in concentrated colloidal dispersions. *Physical Review Letters*, 60:2705, 1988.

[31] Alfons van Blaaderen, J. Peetermans, Georg Maret, and Jan K. G. Dhont. Long-time self-diffusion of spherical colloidal particles measured with fluorescence recovery after photobleaching. *The Journal of Chemical Physics*, 96:4591–4603, 1992.

[32] Donald Voet, Judith G. Voet, and Charlotte W. Pratt. *Fundamentals of Biochemistry: Life at the Molecular Level*. John Wiley & Sons Inc, USA, 3rd edition, 2008.

[33] Kunihiko Gekko and Hajime Noguchi. Compressibility of globular proteins in water at 25 °c. *The Journal of Physical Chemistry*, 83:2706–2714, 1979.

[34] Suliman Barhoum and Anand Yethiraj. An NMR study of macromolecular aggregation in a model polymer-surfactant solution. *The Journal of Chemical Physics*, 132:19, 2010.

[35] Swomitra Palit and Anand Yethiraj. A new model system for diffusion NMR studies of concentrated monodisperse and bidisperse colloids. *Langmuir*, 24:3747–3751, 2008.

[36] Amit K. Agarwal and Anand Yethiraj. Low-density ordered phase in brownian dipolar colloidal suspensions. *Physical Review Letters*, 102:1–4, 2009.

Chapter 7

NMR Study of Membrane-Associated Peptides and the Impact of Peptide Size on Micelle Properties

7.1 Abstract

The nature of peptide-micelle complexes and micelles were studied for a 19-residue antimicrobial peptide (Gad2) in complex with anionic surfactant (sodium dodecyl sulfate (SDS)) as well as for two smaller dipeptides (Ala-Gly and Tyr-Leu) in complex with SDS, and in SDS alone respectively. Using pulsed-field-gradient PFG-NMR spectroscopy measurements, we extracted the hydrodynamic radius of an antimicrobial peptide (Gad2)-sodium dodecyl sulfate (SDS) complex as a function of SDS concentration. The size of a Gad2-SDS complex shows more than a factor-of-two increase over the entire range of SDS concentration, while there is only a small increase in the aggregate number of SDS molecules per each Gad2 molecule. This suggests that the number of peptide molecules in the complex increases with the SDS concentration. For dipeptide (Ala-Gly and Tyr-Leu)-SDS solutions, PFG-NMR measurements show that the self-diffusion coefficient of

SDS is similar to the self-diffusion of SDS in the absence of peptide. This indicates that, unlike larger peptides, Ala-Gly and Try-Leu peptides do not impact significantly the aggregate nature of SDS micelles. Comparing the diffusometry results of buffered SDS system with unbuffered SDS/D$_2$O systems suggested that the micellar size in the buffered system is smaller than the micellar size in the unbuffered system for SDS concentrations below 60 mM. Moreover, the observed self-diffusion coefficient of SDS in the buffered and unbuffered SDS systems merge at around 60 mM. This concentration is identified as an onset of crowding beyond which hydrodynamic corrections to the diffusion coefficient are extremely important.

7.2 Introduction

Membrane-associated proteins and peptides are often studied in the context of micelles. Micelles provide a hydrophobic-hydrophilic interface, but unlike large systems such as liposomes, are small enough to enable solution NMR signals to be observed. Micelles are commonly employed in NMR structure determination of membrane proteins,[1,2] but have also been used in studies where the protein-lipid interaction itself is the focus.[3-6] One important class of membrane-associated proteins are the antimicrobial peptides (AMPs).

AMPs are often short peptides consisting of 12 to 50 residues and act by associating with (and often disrupting) membranes. AMPs have been shown to play an important role in attacking and killing microbes such as bacteria, viruses, and fungi.[7-10] Moreover, some AMPs exhibit activities against tumor cells by disrupting the membrane of the diseased cells and targeting the cell interior without affecting the membrane of host cells in the mammal's body.[11] This selectivity, for microbial and/or tumour cells, is thought to arise in large part due to the interaction between the positive charge on the AMP, with the anionic components of the tumour or pathogen cell membrane.[12] Therefore, anionic sodium dodecyl sulfate SDS micelles are commonly employed in the structural studies of AMPs, as well as other membrane proteins.[13-21]

171

Studying the dynamics of proteins in protein-micellar systems by extracting their diffusion coefficients can be useful. These provide information about the fraction of peptide in the aggregate and free states as well as the average size of protein-micelle complexes. Therefore, NMR diffusometry[3,4] as well as fluorescence correlation spectroscopy[5,6] have been used as tools to obtain the size of protein-micelle complexes.

A starting point for determining the details of protein or peptide structure is the determination of its hydrodynamic size. Extracting the true hydrodynamic radius R_H of biomolecules or biomolecular complexes in realistic mimetics of cellular environments is challenging for two reasons. First, R_H is only meaningful when extracted from self-diffusion coefficients extrapolated to infinite dilution of the diffusing object. At finite concentrations there are hydrodynamic corrections to the diffusion coefficient.[22] Even for a simple colloidal system of spherical particles, these corrections depend sensitively on the details of interparticle interactions. Second, this problem is compounded by the practical challenge that many membrane proteins of interest can only be prepared in tiny quantities, making a detailed study as a function of micelle volume fraction impractical.

In this work, we use NMR diffusometry and relaxometry to identify the principles one needs to apply to obtain reliable quantities such as the hydrodynamic radius and the aggregate ratio, a number characterizing the ratio of detergent to peptide molecules in the aggregate (non-free) state. We find, reassuringly, that the most minimal model utilized to extract hydrodynamic size works well for peptides, at least for those with the size (19 residues) of Gad2 or greater; however, one must be careful to avoid the onset of crowding in order to reliably use these simple models.

The nature of the association of peptides with anionic SDS micelles depends on the details of the electrostatic environment; for example, cationic peptides bind more strongly than their zwitterionic counterparts.[17] NMR diffusometry studies have also found that peptide binding with anionic SDS micelles and zwitterionic dodecylphosphocholine (DPC) micelles are different, also due to the difference in electrostatic environment.[19] Similarly, it was found that a cell-penetrating peptide

172

(CPP) alters the dynamics and size of neutral and negatively charged bicelles in different ways.[23] Several diffusion studies in peptide- or protein-micelle systems have been carried out in the last twelve years.[20,21,23–30] However, the onset of crowding effects remain ambiguous, the partitioning of SDS and peptide molecules and true hydrodynamic radius of a peptide-SDS complex over a wide range of SDS concentration remain unquantified.

Pulsed-field gradient (diffusion) NMR studies have also showed that the hydrophobic interaction has a significant role in the peptide-micelle binding process.[18] A similar conclusion on the role of the hydrophobic interaction was reached on the binding of neuropeptides to a membrane-mimic environment[28] and on the binding of two tripeptide systems to SDS micelles.[16]

NMR studies were carried out to study the binding of a cationic peptide on SDS micelles in the presence and absence of zwitterionic CHAPS (3-[(3-cholamidopropyl)dimethylammonio]-1-propanesulfonate) surfactant as a crude model for cholesterol in the biological membrane. While the binding of the peptide to the SDS micelle, in CHAPS-free solution, is attributed to electrostatic attraction as well as hydrophobic interaction, the presence of CHAPS in the solution inhibits the hydrodynamic interaction of the peptide with the comicelles composed of anionic SDS and zwitterionic CHAPS surfactants.[15]

Since AMPs are subjects of much interest and also represent an even larger class of amphipathic, helical peptides, an AMP, Gad2, was selected for this study. Gad2, and a related peptide Gad1, have been identified in recent efforts to discover new AMPs in Atlantic Cod fish.[31,32]

In this work, we used NMR diffusometry and relaxometry to study the interaction between the cationic Gad2 AMP and an anionic SDS micelle as a membrane mimic environment. In order to do so, we used the same simple model that was applied and developed to signal the changes in the nature of the complexes in a system of nonionic polymer-anionic surfactant system in aqueous solution.[33] We compare the nature of the resulting peptide-SDS complex with those that form with two much smaller peptides, and are able to identify important distinguishing characteristics.

7.3 Experimental

Gad2 peptide with 2168 average molecular mass has been synthesized and purified in a similar way as surfactant-protein B (SP-B) peptide.[34] Ala-Gly peptide with 146.14 average molecular mass, Tyr-Leu peptide with 294.35 average molecular mass, and SDS (99% purity) with 288.38 average molecular mass were purchased from Sigma-Aldrich Canada and were used as received without purification. Deuterium oxide D_2O with 99.9% isotopic purity was purchased from Cambridge Isotope Laboratories.

Table 7.1: Sample nomenclature. All samples unless stated have 0.1 M sodium oxalate buffer in them.

Abbreviation	Complete sample details
SDS-a	SDS/sodium oxalate(0.1M)/D_2O
SDS-b	SDS(60mM)/sodium oxalate(0.1M)/D_2O
SDS-c	SDS(187mM)/sodium oxalate(0.1M)/D_2O
Gad2-SDS-a	Gad2/SDS/sodium oxalate(0.1M)/D_2O
Gad2-SDS-b	Gad2(2mM)/SDS(60mM)/sodium oxalate(0.1M)/D_2O
Gad2-SDS-c	Gad2(2.67mM)/SDS(80mM)/sodium oxalate(0.1M)/D_2O
Ala-Gly-a	Ala – Gly(2mM) /sodium oxalate(0.1M)/D_2O
Ala-Gly-SDS-b	Ala – Gly(2mM)/SDS/sodium oxalate(0.1M)/D_2O
Ala-Gly-SDS-c	Ala – Gly(2mM)/SDS(60mM)/sodium oxalate(0.1M)/D_2O
Tyr-Leu-a	Tyr – Leu(2mM)/sodium oxalate(0.1M)/D_2O
Tyr-Leu-SDS-b	Tyr – Leu(2mM)/SDS/sodium oxalate(0.1M)/D_2O
Tyr-Leu-SDS-c	Tyr – Leu(2mM)/SDS(60mM)/sodium oxalate(0.1M)/D_2O

Gad2-SDS-a samples were prepared from two different stock solutions. We prepared three different stock solutions: Gad2-SDS-b, Gad2-SDS-c, and sodium oxalate (0.1M)/D_2O. Samples

with SDS concentration (20 mM, 30 mM, and 60 mM) were prepared by mixing Gad2-SDS-b stock solution with sodium oxalate(0.1M) /D_2O stock solution, while we used Gad2-SDS-c stock solution to prepare samples with SDS concentration (1 mM, 2 mM, 4 mM, 8 mM, 13.3 mM, 25 mM, 35 mM, 40 mM, 50 mM, 80 mM), where the ratio (R) of SDS concentration to peptide concentration is constant (R = [SDS]/[Gad2] = 30).

Ala-Gly-SDS-b samples were prepared by mixing Ala-Gly-SDS-c stock solution with Ala-Gly-a stock solution. Also, Tyr-Leu-SDS-b samples were prepared by mixing Tyr-Leu-SDS-c stock solution with Tyr-Leu-a.

SDS-a samples were prepared from two different stock solutions. Samples with SDS concentration below 60 mM were prepared by mixing SDS-b stock solution with sodium oxalate(0.1M)/D_2O stock solution, while samples with SDS concentration above 60mM were prepared by mixing SDS-c stock solution with /sodium oxalate(0.1M)/D_2O stock solution. The pH value of different stock solutions including the buffer solution were adjusted to be 4 by the addition of sodium deuteroxide or deuterium chloride.

The one-dimensional (1D) proton NMR spectra for different species in all samples at a resonance frequency of 600 MHz on a Bruker Avance II spectrometer are shown in figure 7.1. In all cases the trace signal of HDO in D_2O is the most dominant peak; however the HDO, peptide and SDS peaks are all spectrally separable. An advantage of the Gad2 peptide is that it has aromatic groups; thus the spectral region of the aromatic group is used to measure separately the peptide signal attenuation which is used to extract the self-diffusion coefficient of the peptide molecule in our Gad2-SDS samples. In these samples, the spectra of both SDS and the Gad2 peptide components overlap in the (0-4ppm) spectra region.

Figure 7.1 shows the one dimensional spectra for SDS-a with C^{SDS} = 6 mM, Gad2-SDS-b, Ala-Gly-SDS-b with C^{SDS} = 6 mM, and Tyr-Leu-SDS-b with C^{SDS} = 6 mM samples at sample temperature 298K.

The self-diffusion measurements were carried out in a diffusion probe (Diff 30) and with maxi-
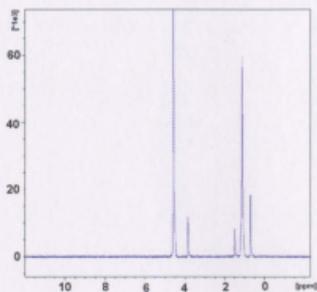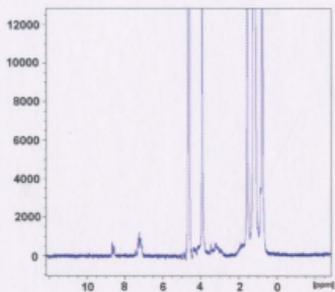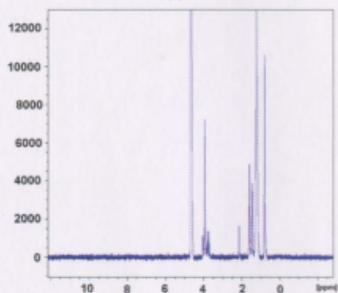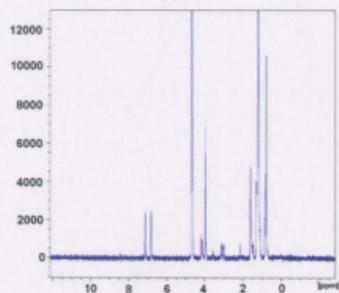
Figure 7.1: 1D ^{1}H NMR spectrum for (a) SDS-a with $C^{SDS} = 6$ mM (b) Gad2-SDS-b (c) Ala-Gly-SDS-b with $C^{SDS} = 6$ mM (d) Tyr-Leu-SDS-b with $C^{SDS} = 6$ mM at sample temperature 298 K.

mum field gradient (1800 G/cm). Diffusion was measured with a pulsed-field gradient stimulated-echo sequence[35] with (almost square) trapezoidal gradient pulses. The diffusion coefficient of a molecule in aqueous solution was obtained from the attenuation of the signal according to the equation[35]

$$\ln\left(\frac{S(k)}{S(0)}\right) = -Dk \tag{7.1}$$

where $S(k)$ is the ``intensity''of the signal (the integration of the relevant peak region) in the presence of field gradient pulse, $S(0)$ is the intensity of the signal in the absence of field gradient pulse, $k = (\gamma\delta g)^2(\Delta - \delta/3)$ is a generalized gradient strength parameter, $\gamma = \gamma^H = 2.6571 \times 10^8$ T^{-1}s^{-1} is the gyromagnetic ratio of the ^{1}H nucleus, $\delta = 2$ ms is the duration of the field gradient pulse, $\Delta = 100$ ms is the time period between the two field gradient pulses, and g is the amplitude of the field gradient pulse.

The signal attenuation in all samples was observed to be monoexponential (figure 7.2). This suggests that the exchange of SDS molecules between the SDS in micelles and in free solution must be very rapid on the NMR time scale. Values of the diffusion coefficients were calculated from the monoexponential decays using equation 7.1.

Figure 7.2 shows the signal attenuation and the self-diffusion coefficients for SDS and peptides in the different peptide systems. For SDS-a system (figure 7.2a), the spectrum region 0-4 ppm is used to measure the signal attenuation. For the Gad2-SDS system (figure 7.2b) the spectrum region 0-4 ppm is used to measure the SDS signal attenuation while the spectrum region 7-9 ppm is used to measure Gad2 signal attenuation. For the Ala-Gly-SDS-b system (figure 7.2c), the SDS signal attenuation is measured using the SDS peak at 0.8 ppm, while the spectrum region at 3.6ppm is used to measure the Ala-Gly signal attenuation. Also, for the Tyr-Leu-SDS-b system (figure 7.2d), the SDS signal attenuation is measured using SDS peak at 3.8 ppm, while the spectrum region 6-8 ppm is used to measure the Tyr-Leu signal attenuation.
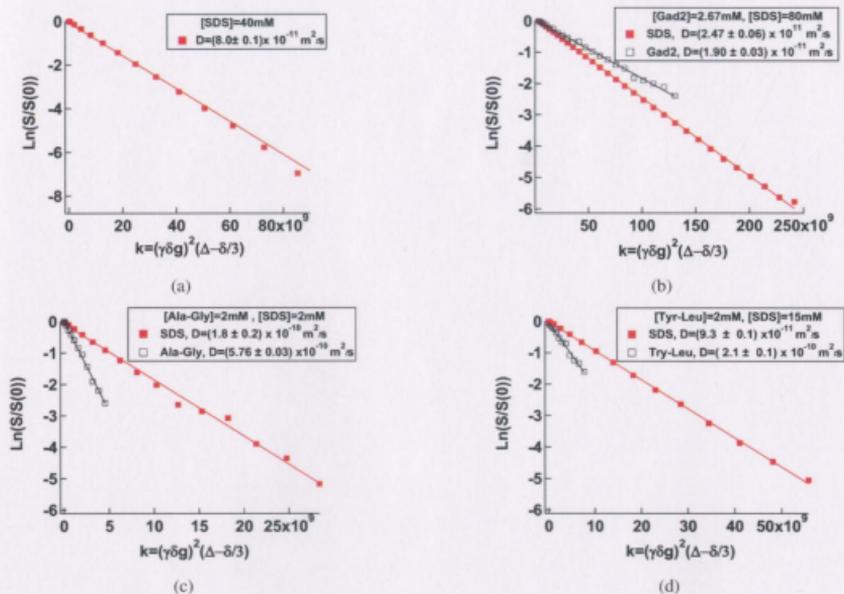
Figure 7.2: The attenuation of the signal S(k)/S(0) on a log scale versus $k = (\gamma\delta g)^2(\Delta - \delta/3)$ for (a) SDS-a with $C^{SDS} = 40$ mM(b) Gad2-SDS-c (c) Ala-Gly-SDS-b with $C^{SDS} = 2$ mM (d) Tyr-Leu-SDS-b with $C^{SDS} = 15$ mM with $\delta = 2$ ms and $\Delta = 100$ ms.

178

Values of the self-diffusion coefficients D are calculated from the slopes of the curves in figure 7.2. The signal attenuation is normalized with respect to the value at zero gradient. Therefore, $\ln(S(k)/S(0)) = 0$ at zero field gradient. T_1 relaxation measurements were also performed using the Diff30 diffusion probe and the relaxation rates ($R_1 = 1/T_1$) are reported in section 7.4.1.

7.4 Results and Discussion

7.4.1 Relaxometry

Longitudinal T_1 relaxation measurements were carried out for the SDS peaks for different peptide samples and at different SDS concentration. All results (figure 7.3) exhibit an exponential dependence on surfactant concentration. Because this exponential dependence arises from changes in the surfactant environment, this is typically interpreted as an estimator of critical aggregation concentrations.[36-38]

Figure 7.3 shows the variation in the proton relaxation rate R_1 for the SDS peaks in SDS-a, Gad2-SDS-a, Ala-Gly-SDS-b, and Tyr-Leu-SDS-b samples. In all cases, the concentration dependence can be fit to an exponential, the exponent is an estimator of the critical aggregation concentration (CAC) or critical micellar concentration (CMC). The monoexponential fit is phenomenological.

Proton longitudinal relaxation measurements were carried out for the SDS peaks for SDS-a at different SDS concentration (figure 7.3a). A fit to $y0 + A \exp(-C^{SDS}/C_0)$ yields a ($C_0 = 1.9 \pm 0.2$ mM), which we identify with the critical micelle concentration CMC. Figure 7.3b shows the variation in the proton longitudinal relaxation rate R_1 for the SDS peaks for Gad2-SDS-a samples in the range $0 - 4$ ppm at different SDS concentration, where the critical aggregation concentration CAC of the Gad2-SDS-a system is (1.3 ± 0.1 mM). Figure 7.3c shows the variation in the proton longitudinal relaxation rate R_1 for the SDS peak for Ala-Gly-SDS-b samples at 0.8ppm at different SDS
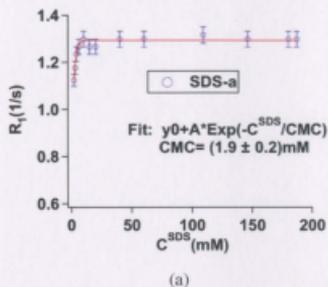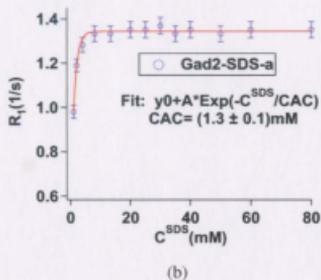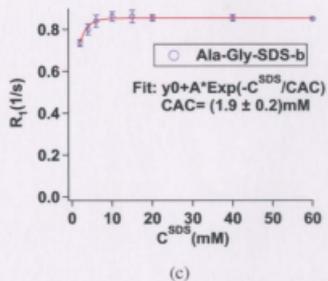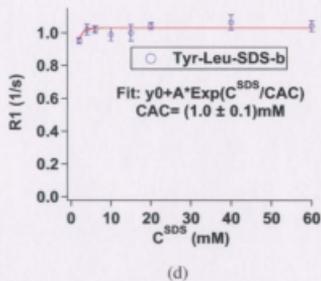
Figure 7.3: (c) Proton longitudinal relaxation rate R_1 for SDS for SDS-a versus SDS concentration C^{SDS}. (b) Proton longitudinal relaxation rate R_1 for SDS for Gad2-SDS-a samples (c) Proton longitudinal relaxation rate R_1 for SDS for Ala-Gly-SDS-b samples (d) Proton longitudinal relaxation R_1 for SDS for Tyr-Leu-SDS-b samples.

concentration, where the critical aggregation concentration CAC of the Ala-Gly-SDS-b system is 1.9 ± 0.2 mM. Figure 7.3d shows the variation in the proton longitudinal relaxation rate R_1 for the SDS peak for Tyr-Leu-SDS-b samples at 3.8 ppm at different SDS concentration, where the critical aggregation concentration CAC of the Tyr-Leu-SDS-b system is 1 ± 0.1 mM

7.4.2 Diffusometry

7.4.2.1 Surfactant Solutions and Analysis Methods

Figure 7.4a shows the self-diffusion coefficient of SDS in an SDS system SDS-a (with no peptide) with sodium oxalate buffer (pH=4) (red open circles) and without sodium oxalate buffer SDS/D_2O (pH=3-3.5) (blue open squares). Also, in the same graph, the self-diffusion coefficient of SDS in an SDS system SDS/D_2O (with no peptide), without sodium oxalate buffer, and with pH=4 (black filled squares). SDS samples whose pH was not adjusted (pH=3-3.5), and SDS samples whose pH was adjusted to pH=4 show certainly the same behavior, but the buffered samples at pH=4 show different behavior in the SDS concentration regime below 60 mM. This indicates that sodium oxalate buffer impacts significantly the self-diffusion coefficients.

Because the pulsed-field-gradient attenuation is monoexponential (figure 7.2a), this suggests that the exchange of SDS molecules between the SDS in micelles and in free solution must be very rapid on the NMR time scale. Therefore, in the interpretation of observed diffusion coefficients in surfactant systems, where a surfactant molecule visits more than one environment over very short timescales, a two-site exchange model is known to work very well.[39] For example, in all systems considered here, the SDS surfactant can either be a free monomer in solution or associated with a surfactant-rich aggregate. Thus, the self-diffusion coefficient of SDS is a linear combination of the self-diffusion coefficient D_{free}^{SDS} of the free molecules in bulk and that of the bound molecules in the micelle $D_{micelle}^{SDS}$ in peptide-free solutions or a peptide-SDS complex D_{Aggr}^{SDS}:
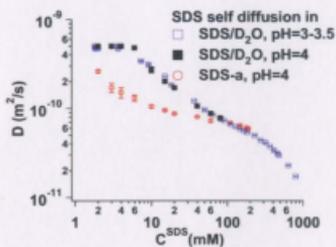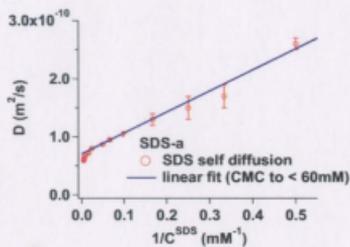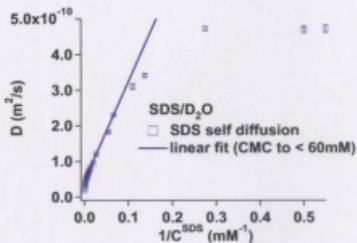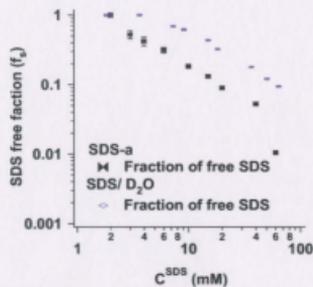
Figure 7.4: (a) Self-diffusion coefficient of SDS in an SDS system SDS-a (with no peptide) with sodium oxalate buffer (pH=4) (red open circles) and without sodium oxalate buffer SDS/D$_2$O (pH=3-3.5) (blue open squares) as well as an SDS system SDS/D$_2$O (with no peptide) without buffer and with pH=4 (black filled squares) versus SDS concentration C^{SDS} (b) self-diffusion of SDS for SDS-a versus reciprocal of SDS concentration 1/C^{SDS} (c) self-diffusion of SDS for SDS/D$_2$O versus reciprocal of SDS concentration 1/C^{SDS} (d) fraction (f$_s$) of free SDS for SDS-a and SDS/D$_2$O systems.

$$D_{Obs}^{SDS} = f_s \, D_{free}^{SDS} + (1 - f_s) \, D_{Aggr}^{SDS} \qquad (7.2)$$

for $C^{SDS} > C_0$, where f_s is the fraction of free SDS molecules, D_{Aggr}^{SDS} is either the micellar diffusion coefficient or the micelle-peptide complex diffusion coefficient, and C_0 refers to the critical (micellar or aggregation) concentration (CMC or CAC), and C^{SDS} is the total SDS concentration.

Two approaches are used in order to extract physical parameters such as the fraction (f_s) of free SDS molecules and the self-diffusion of a peptide-SDS complex D_{aggr}^{SDS} or the micellar aggregate $D_{micelle}^{SDS}$. The first and more general approach is to rewrite equation 7.2 in the form

$$D_{Obs}^{SDS} = \left(D_{free}^{SDS} - D_{Aggr}^{SDS}\right)\left(C_{free}^{SDS}\right)\left(\frac{1}{C^{SDS}}\right) + D_{Aggr}^{SDS} \qquad (7.3)$$

for $C^{SDS} > C_0$, D_{free}^{SDS} is always a constant and very close to the self-diffusion coefficient of SDS at any concentration below the CMC. Linear dependence of the SDS self-diffusion D_{Obs}^{SDS} versus the reciprocal of SDS concentration $1/C^{SDS}$ implies that C_{free}^{SDS} and D_{Aggr}^{SDS} are constants. In addition, we may extract D_{Aggr}^{SDS}, i.e. the self-diffusion coefficient for either an SDS micelle $D_{micelle}^{SDS}$ or a peptide-SDS complex D_{Aggr}^{SDS} from the intercept, and the concentration of free SDS molecules C_{free}^{SDS} is calculated from the slope. Using these values, in the linear (low concentration) regime, we can obtain the free surfactant fraction as a function of concentration even at higher concentrations using

$$f_s(C^{SDS}) = \frac{D_{Obs}^{SDS} - D_{micelle}^{SDS}}{D_{free}^{SDS} - D_{micelle}^{SDS}}. \qquad (7.4)$$

A second and more minimal approach is feasible when the size of the peptide that has a tendency to associate with micelles is large enough that surfactant motion is rapid on the timescale of peptide motion. Therefore, this kind of peptide is usually associated with several surfactants and so there can never be a free peptide, i.e. the peptide binding fraction is close to 1. In this case, $D_{Aggr}^{SDS} = D^{Peptide}$. Using this additional information allows us to use the two-site model even in a

183

(a)

(b)

(c)
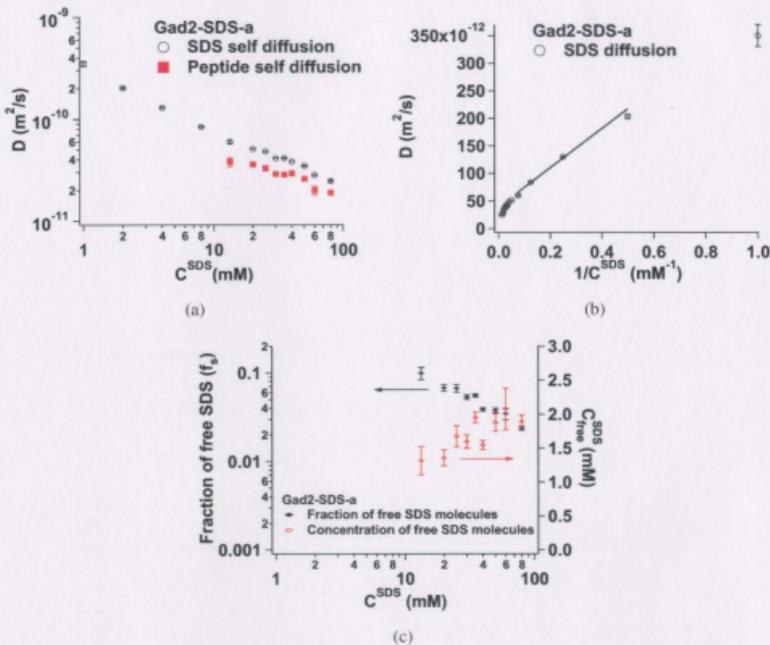
Figure 7.5: (a) Self-diffusion of Gad2 and SDS for Gad2-SDS-a samples versus SDS concentration C^{SDS} (b) self-diffusion of SDS for Gad2-SDS-a versus reciprocal of SDS concentration $1/C^{SDS}$ (c) fraction (f_s) of free SDS and concentration (C^{SDS}_{free}) of free SDS versus SDS concentration C^{SDS}.

184

regime where the D_{Obs}^{SDS} versus $1/C^{SDS}$ relationship is not linear. The only proviso is that the overall particulate volume fraction must always be small enough that hydrodynamic effects are negligible. For the SDS system, this is generally true for concentrations below 60 mM, or volume fractions below 0.04. Using this we can rewrite equation 7.2 in the form:

$$f_s(C^{SDS}) = \frac{D_{Obs}^{SDS} - D^{Peptide}}{D_{free}^{SDS} - D^{Peptide}}. \tag{7.5}$$

For buffered and unbuffered SDS solutions we find a systematic difference in all quantities. The micellar self-diffusion coefficient $D_{micelle}^{SDS} = 7.2 \pm 0.1 \times 10^{-11}$ m^2/s and $4.42 \pm 0.02 \times 10^{-11}$ m^2/s in the SDS-a and SDS/D_2O systems respectively. The self-diffusion coefficient of the SDS micelle is extracted by linearly fitting the self-diffusion coefficient of SDS in figure 7.4b and figure 7.4c, respectively, in the regime of SDS concentration that is higher than CMC but below the onset of crowding.[33]

The concentrations of free surfactant in solution are found to be $C_{free}^{SDS} = 1.8 \pm 0.1$ mM and 5.1 ± 0.4 mM[33] for SDS-a and SDS/D_2O respectively. Moreover, the fraction (f_s) of free surfactant (figure 7.4d) is obtained using $D_{free}^{SDS} = (2.6 \pm 0.1) \times 10^{-10}$ m^2/s and $(4.7 \pm 0.1) \times 10^{-10}$ m^2/s. These are the SDS observed self diffusion coefficients in buffered and unbuffered systems, respectively, at the lowest SDS concentration (figure 7.4a), which is below the CMC, and at very low surfactant packing fraction ($\Phi < 0.001$). Therefore, all surfactants are in the non-aggregated state, and hydrodynamic effects are negligible.

The ratio of D_{free}^{SDS} in the unbuffered with respect to the buffered SDS solution is ≈ 2 for $C^{SDS} < 60$ mM (figure 7.4a). This indicates the presence of of stable dimers and n-mers (n $< 2^3 = 8$). Also, the micellar self-diffusion coefficient in the unbuffered SDS solution is significantly larger than the micellar self-diffusion coefficient in the buffered solution (figure 7.4b). This indicates that while the micellar size in the SDS-a system is smaller than the micellar size in the SDS/D_2O system, the fraction (f_s) of free SDS molecules (figure 7.4d) for SDS-a shows a more rapid decrease compared

to the fraction (f_s) for the SDS/D$_2$O system. The presence of sodium oxalate buffer (Na$_2$C$_2$O$_4$) promotes the formation of SDS micelles. Moreover, it causes a decrease in the value of critical micellar concentration.

7.4.2.2 Peptide: Gad2

Figure 7.5a shows the self-diffusion coefficient of Gad2 and SDS in Gad2-SDS-a. We measured the self-diffusion of Gad2 in the SDS concentration range above 13.3 mM. Due to experimental limitations (small value of signal to noise ratio), we were not able to extract the self-diffusion coefficient of Gad2 in the SDS concentration range below 13.3 mM.

Figure 7.5b is a plot of D_{Obs}^{SDS} versus $1/C^{SDS}$. Over a range of concentrations, this behavior is linear and yields $D_{Aggr}^{SDS} = (3.9 \pm 0.1) \times 10^{-11}$ m^2/s. Since the concentration of SDS is 30 times higher than Gad2 concentration (R = [SDS]/[Gad2] = 30), we know that there is unlikely to be free peptide. Therefore, we use equation 7.5 with $D^{Peptide} = D_{Obs}^{Gad2}$ and $D_{free}^{SDS} = (2.6 \pm 0.1) \times 10^{-10}$ m^2/s to obtain the fraction (f_s) of free surfactant in the monomer state in the aqueous solution as well as the concentration of free surfactant C_{free}^{SDS}, this is shown in figure 7.5c. With increasing surfactant concentration, f decreases while C_{free}^{SDS} rises from about 1 mM to an asymptotic value of $\approx$ 2 mM.

The lower value (near 1 mM) is consistent with CAC value of (1.1±0.2) mM that is extracted using relaxometry (figure 7.3b). This is consistent with the picture[33, 40] that the concentration of free surfactant above the CAC/CMC is equal to the value of the CAC/CMC. In the peptide-SDS system (and similar to the behavior in the nonionic polymer-anionic surfactant system (poly(ethylene) oxide (PEO)-SDS system)[33]) the free concentration rises further until it reaches the CMC value in the buffered solution.

Also, we estimate the hydrodynamic radius R_H of Gad2-SDS complexes (figure 7.6a) using the Stokes-Einstein-Sutherland equation[41]

186
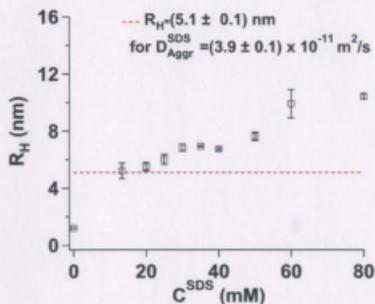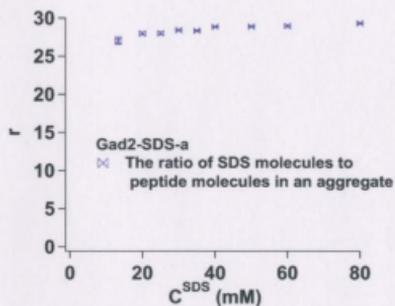
Figure 7.6: (a) The hydrodynamic radius (R_H), extracted from the peptide diffusion coefficient, of Gad2-SDS complexes versus SDS concentration C^{SDS}. The dashed line is the value obtained *via* the SDS diffusion coefficient at lower SDS concentrations. (b) The ratio (r) of SDS molecules to peptide molecules in a complex versus SDS concentration (C^{SDS}) for Gad2-SDS-a samples.

$$R_H = \frac{K_B T}{6\pi\eta D},$$ (7.6)

where K_B is the Boltzmann constant, T is the absolute temperature, $D = D^{Peptide}$, and η is the solvent viscosity ($\eta_{D_2O} = 1.1$ mPa.s). The R_H value obtained from surfactant diffusion in a peptide-SDS complex is consistent with the lowest value obtained for peptide diffusion in Gad2-SDS-a and is approximately 5 nm. Since the values obtained for surfactant diffusion represent the asymptotic value at low dilution, this agreement is a welcome self-consistency check. R_H (obtained from peptide diffusion) increases as a function of concentration to about 10 nm at 60 mM, approximately a factor of 2 larger.

Moreover, the variation in the ratio of SDS molecules to peptide molecules in a complex r = $(C^{SDS} - C_{free}^{SDS})/(C^{SDS}/R) = (1 - f)R$ is extracted (figure 7.6b). It shows that r exhibits a very slight increase, from 27 to 29, over the entire range of SDS concentration, it approaches R = 30 asymptotically. We need to understand how the aggregate size changes in order to accommodate the two-fold increase in the hydrodynamic radius R_H, we will return to this point later.

7.4.2.3 Dipeptides: Ala-Gly and Tyr-Leu

In order to study the effect of peptide size on the dynamics of peptide-SDS complexes, diffusometry was carried out to quantify complex formation of SDS with the dipeptides Ala-Gly and Tyr-Leu.

A plot of the SDS self-diffusion coefficient for all systems in the current study in one graph (figure 7.7) shows clearly that SDS diffusion looks similar for the systems with small di-peptides (Ala-Gly and Tyr-Leu) and SDS-a systems. This suggests that the fraction of free SDS in Tyr-Leu-SDS-b and Ala-Gly-SDS-b systems is similar to the fraction of free SDS in the SDS-a system (figure 7.4d). On the other hand, SDS diffusion looks very different for the system with long peptide (Gad2-SDS-a), suggesting that the Gad2-SDS complexes are very different from the other Ala-Gly-SDS and Tyr-Leu-SDS complexes which are essentially indistinguishable from micellar
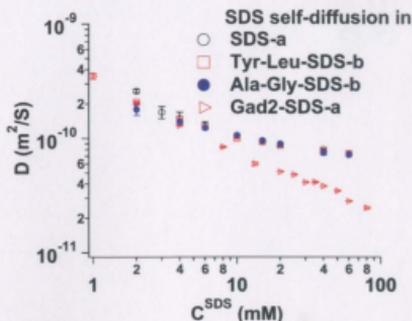
Figure 7.7: Self-diffusion of SDS in all the systems studied: SDS-a, Tyr-Leu-SDS-b, Ala-Gly-SDS-b, and Gad2-SDS-a. Sample nomenclature is provided in Table 1.

aggregates with no peptide.

Figure 7.8a shows the self-diffusion coefficient of Ala-Gly and SDS in the Ala-Gly-SDS-b system. By linearly fitting the self-diffusion of SDS, D_{Obs}^{SDS} (figure 7.8b), for SDS concentration higher than CAC, we extract the self-diffusion coefficient of SDS in the Ala-Gly-SDS complex $D_{Aggr}^{SDS} = (7.4 \pm 0.8) \times 10^{-11}$ m^2/s. The hydrodynamic radius of Ala-Gly-SDS complex $R_H = (2.7 \pm 0.3)$ nm is then calculated using equation 7.6. In addition, the concentration of free SDS molecules $C_{free}^{SDS} = (1.7 \pm 0.2)$ mM. The scatter in the values comes from the very low value of the fraction of bound peptide $(1 - f_p)$ for concentrations ≤ 20 mM.

Since the Ala-Gly peptide is short, they are rapidly exchangeable between free and aggregate states. Thus, the fraction (f_p) of free Ala-Gly peptide is calculated using the following equation,

$$f_p = \frac{D_{Obs}^{Peptide} - D_{Aggr}^{SDS}}{D_{free}^{Peptide} - D_{Aggr}^{SDS}} \qquad (7.7)$$

where $D_{free}^{Ala-Gly} = (5.3 \pm 0.2) \times 10^{-10}$ m^2/s is the self diffusion of Ala-Gly peptide in the SDS-free solution and $D_{Aggr}^{SDS} = (7.4 \pm 0.8) \times 10^{-11}$ m^2/s.

189
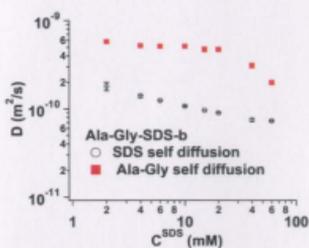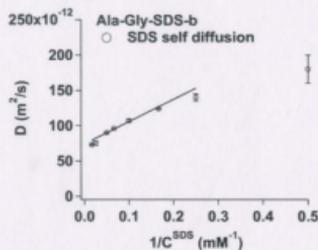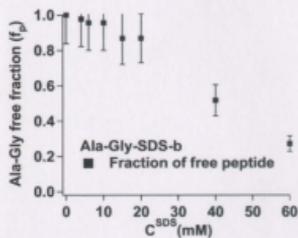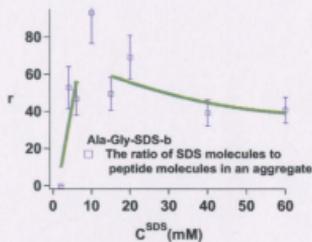
Figure 7.8: (a) Self-diffusion of Ala-Gly and SDS for Ala-Gly-SDS-b samples versus SDS concentration C^{SDS} (b) self-diffusion of SDS for Ala-Gly-SDS-b versus reciprocal of SDS concentration $1/C^{SDS}$ (c) fraction (f_p) of free Ala-Gly (d) the ratio (r) of SDS molecules to peptide molecules in a complex versus SDS concentration (C^{SDS}) for Ala-Gly-SDS-b samples.

From the calculated values of the free fraction (f_s) of SDS and free fraction (f_p) of Ala-Gly pep-tide, the ratio of SDS molecules to peptide molecules in the aggregate state $r = (C^{SDS}/2mM)((1 - f_s)/(1 - f_p))$ is calculated in the Ala-Gly-SDS-b system (figure 7.8d). The graph shows a scatter in r for finite concentration, with a mean value $r = 48 \pm 4$.

(a)

(b)

(c)

(d)
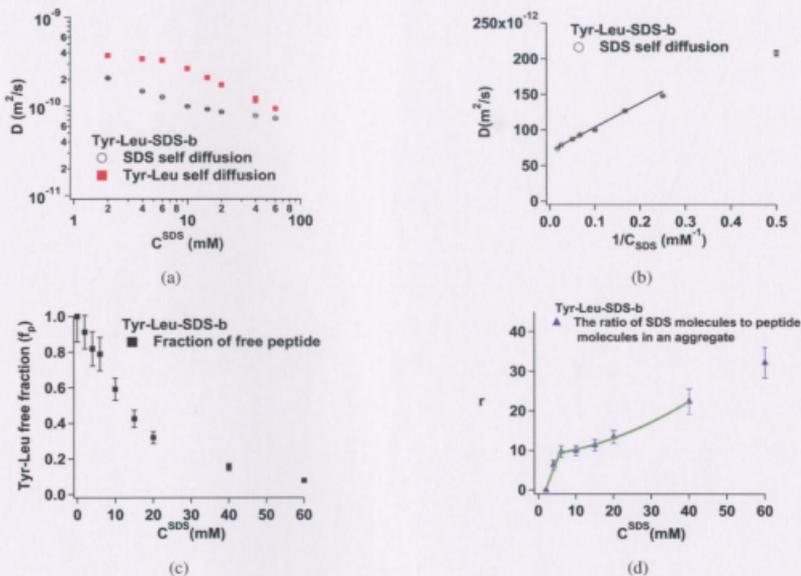
Figure 7.9: (a) Self-diffusion of Tyr-Leu and SDS for Tyr-Leu-SDS-b samples versus SDS concen-tration C^{SDS} (b) self-diffusion of SDS for Tyr-Leu-SDS-b versus reciprocal of SDS concentration $1/C^{SDS}$ (c) fraction (f_p) of free Tyr-Leu (d) The ratio (r) of SDS molecules to peptide molecules ``in a complex'' versus SDS concentration (C^{SDS}) for Tyr-Leu-SDS-b samples.

Diffusometry was also carried out on the dipeptide Tyr-Leu system. Figure 7.9a shows the self-diffusion coefficient of Tyr-Leu and SDS in Tyr-Leu-SDS-b. The analysis method is identical to

that in the Ala-Gly-SDS-b system. The observed self-diffusion of SDS is a weighted-average parameter, where the self-diffusion coefficient of SDS D_{Aggr}^{SDS} in the Tyr-Leu-SDS complex is extracted by linearly fitting the self-diffusion of SDS D_{Obs}^{SDS} (figure 7.8b) in the regime of SDS concentration which is higher than CAC. Thus, by using equation 7.6, the hydrodynamic radius of Tyr-Leu-SDS complex $R_H = (2.87 \pm 0.04)$ nm.

For Tyr-Leu-SDS-b the $D_{free}^{Tyr-Leu} = (4.0 \pm 0.4) \times 10^{-10}$ m^2/s is the self diffusion of Tyr-Leu peptide in SDS-free solution and $D_{Aggr}^{SDS} = (6.9 \pm 0.1) \times 10^{-11}$ m^2/s (figure 7.9b). Therefore, the fraction (f_p) of free Tyr-Leu peptide (figure 7.9c), and the ratio of SDS molecules to peptide molecules in the aggregate state (r) (figure 7.9d) for Tyr-Leu-SDS-b system have been extracted in a similar way as for Ala-Gly-SDS-b system. However, for Tyr-Leu-SDS-b system, r exhibits a systematic increase at low SDS concentrations with a change in slope between 5 and 10 mM, reaching a value of approximately r = 20 at 40 mM. Note that the scattering in the data for Tyr-Leu is much smaller than for Ala-Gly. This is due to the presence of a non-negligible fraction of bound peptide even at small SDS concentration. The 60 mM value is not reliable due to crowding effects, this is discussed later. This asymptotic value is comparable to Gad2-SDS, where the asymptotic value approaches the molar ratio at large concentration, consistent with a binding ratio $1 - f_p$ close to 1, and very different from the Ala-Gly-SDS system, where it is closer to 0.5 at 40 mM.

7.5   Conclusion

Using diffusometry, we measured the signal attenuation curves of SDS and peptide components in different samples. The monoexponential signal attenuation curves (figure 7.2) indicate that there is either a quick exchange between the molecules in the monomeric state and aggregate state for SDS and short peptides (Ala-Gly and Try-Leu) or the molecules are presented in one state (e.g. an aggregate state for the long peptide (Gad2)). Therefore, the self-diffusions of SDS molecules and short peptides are weighted-average parameters. Based on that, we were able to extract parameters

such as the fraction and the concentration of free SDS and free peptide molecules over the entire range of SDS concentration.

Using relaxometry (figure 7.3), we estimate the critical micellar concentration (CMC) for the SDS-a system to be 1.9 ± 0.2 mM (figure 7.3a), significantly lower than the value of CMC = 5.2 ± 0.2 mM[33] for the unbuffered SDS/D_2O system. This indicates that the presence of the sodium oxalate buffer in the solution enhances micellar formation. The value of critical aggregation concentration (CAC) for Gad2-SDS-a, Ala-Gly-SDS-b, and Tyr-Leu-SDS-b systems is 1.3 ± 0.1 mM, 1.9 ± 0.2 mM, and 1.0 ± 0.1 mM respectively. Values consistent with these are obtained from diffusion measurements.

The concentration dependence of the self-diffusion coefficient depends sensitively on the presence of sodium oxalate buffer. In the presence of the buffer, we see, not only that the CMC is lower, but micellar diffusion coefficient is larger by a factor of ≈ 2 and the micelle size is smaller by the same factor (figure 7.4b). The diffusion coefficients for buffered and unbuffered surfactant merge at around 60mM. In past work[33] this concentration has been identified as the onset of crowding, and so we can say with confidence that 60 mM in the SDS system signals the concentration at which one cannot extract hydrodynamic radius or aggregate ratios from observed diffusion coefficients.

There is a distinct difference in the behavior of large peptides ($M_w^{peptide} > M_w^{surfactant}$) and small dipeptides ($M_w^{peptide} \approx M_w^{surfactant}$). The small dipeptides (Ala-Gly and Tyr-Leu) hardly affect the SDS diffusion coefficient (figure 7.7). This is consistent with the dipeptides behaving just as the surfactant does, i.e. rapidly exchanging between aggregate and free state. For large peptides such as Gad2, on the other hand, rapid exchange between free and aggregate state is practically impossible. This is because the surfactant molecules form micellar-like aggregates along the peptide chain. This is consistent with a bead-on-a-chain picture[42, 43] for large-molecule aggregates.

The surfactant itself is always in the rapid exchange limit. The concentration of free SDS in solution rises from the CAC value (≈ 1 mM) to the CMC value (≈ 2 mM) when the total SDS concentration increases from 10 to 60 mM. In Gad2-SDS samples, the SDS concentration is increased,

193

with the peptide-surfactant molar ratio kept constant. Therefore, a moderate increase in free surfactant concentration necessarily implies a small change in aggregate number (the number of SDS molecules associated with each Gad2 molecule) from 27 to 29. The hydrodynamic radius of the aggregate state is more than 3 times the size of a peptide monomer in the absence of surfactant. The concentration range between 0 and 10 mM is the regime where the linear model (equation 7.3) is valid. At 10 mM, the surfactant aggregate diffusion coefficient and the peptide diffusion coefficient coincide. At larger concentrations (where the linear model is not valid), the aggregate size increases from 5 nm at 10 mM to 10 nm at 60 mM. In this range, crowding effects are not yet important, therefore the increase in R_H likely reflects a true increase in aggregate size. Given that the ratio of SDS to Gad2 molecules in a complex is fixed, the only way for mean aggregate size to increase is for the average number of peptides in one complex to increase from 1 (at 10 mM) to approximately 2 (at 50 mM).

In all 3 systems, the concentration of free SDS C_{free}^{SDS} is found to increase over the entire range of SDS concentration, with the asymptotic value being close to 2 mM. This is roughly consistent with the value of the CAC obtained from relaxation experiments, although the values from the latter are not true measurements of the CAC but only indicative values.

Previous experiments have reported peptide binding fractions $f_b = 1 - f_p$ in dipeptides based on measurements at two concentrations.[18] Our results for both Ala-Gly and Tyr-Leu provide these values as a function of SDS concentration. Our values are roughly consistent with those quoted values at concentrations of about 10 mM. We also calculate the ratio of SDS molecules to peptide molecules in the aggregate state, r, in the three peptide-SDS systems, and can compare them to the molar ratio R (which was held constant for Gad2-SDS-a but allowed to increase linearly for the short dipeptides). The quantity r is highly susceptible to noise when the fraction of bound peptide is very small, as is the case for Ala-Gly. The value of r has a self-consistent large concentration asymptote of r = R for Gad2 (figure 7.6b) and Tyr-Leu (figure 7.9d) complexes. However, for Ala-Gly complexes this value is noisy but has a mean value much larger than R (figure 7.8d). This

is indicative of a high peptide free fraction. This indicates that SDS molecules have more affinity to associate with Gad2 and Tyr-Leu peptides than to the Ala-Gly peptide. This is based on the fact that Tyr-Leu dipeptide is more hydrophobic than Ala-Gly dipeptide.

We conclude with some recommendations for diffusion measurements made in order to extract parameters such as the hydrodynamic radius and peptide binding fractions. Our results consistently show that measurements should be made well below the concentration that signals the onset of crowding (about 60 mM for SDS), and a safe recommendation is two-thirds of this value, i.e. 40 mM. Surfactant with sodium oxalate buffer can have unusual properties which should be known a priori, e.g. pure SDS solutions contain micellar aggregates with a hydrodynamic radius twice that of those in solutions with sodium oxalate buffer. Ideally measurements for hydrodynamic radius should be carried out for at least two concentrations. This procedure will work very well for larger peptides, but less well for small ones, especially those that are not very hydrophobic.

Bibliography

[1] Isabelle Marcotte and Michele Auger. Bicelles as model membranes for solid and solution-state NMR studies of membrane peptides and proteins. *Concepts in Magnetic Resonance. Part A*, 24A:17–37, 2005.

[2] David V. Tulumello and Charles M. Deber. SDS micelles as a membrane-mimetic environment for transmembrane segments. *The Journal of Biochemistry*, 48:12096–12103, 2009.

[3] Sara Cozzolino, Maria. G. Sanna, and Massimiliano Valentini. Probing interactions by means of pulsed field gradient nuclear magnetic resonance spectroscopy. *Magnetic Resonance in Chemistry*, 46:S16S23, 2008.

[4] Sven Morein, Theodore P. Trouard, Jon. B. Hauksson, Uif Rilfors, Gosta Arvidson, and Goran Lindblom. Two-dimensional ^{1}H-NMR of transmembrane peptides from escherichia coli phosphatidylglycerophosphate synthase in micelles. *European Journal of Biochemistry*, 241:489–497, 1996.

[5] Lanlan Yu, Minyi Tan, Bow Ho, Jeak Ling Ding, and Thorsten Wohland. Determination of critical micelle concentrations and aggregation numbers by fluorescence correlation spectroscopy: Aggregation of a lipopolysaccharide. *Analytica Chimica Acta*, 556:216–225, 2006.

[6] Ana Paula Romani, Cassia Alessandra Marquezina, and Amando Siuiti Ito. Fluorescence spectroscopy of small peptides interacting with microheterogeneous micelles. *International Journal of Pharmaceutics*, 383:154–156, 2010.

[7] Michael Zasloff. Antimicrobial peptides of multicellular organisms. *Nature*, 415:389–395, 2002.

[8] Pierre Nicolas. Multifunctional host defense peptides: intracellular-targeting antimicrobial peptides. *Federation of European Biochemical Societies*, 276:6483–6496, 2009.

[9] David W. Hoskin and Ayyalusamy Ramamoorthy. Studies on anticancer activities of antimicrobial peptides. *Biochimica et Biophysica Acta*, 1778:357–375, 2008.

[10] V.G. Chinchar, L. Bryan, U. Silphadaung, E. Noga, D. Wade, and L. Rollins-Smith. Inactivation of viruses infecting ectothermic animals by amphibian and piscine antimicrobial peptides. *Journal of Virology*, 323:268–275, 2004.

[11] Kaushal Rege, Suraj J. Patel, Zaki Megeed, and Martin L. Yarmush. Amphipathic peptide-based fusion peptides and immunoconjugates for the targeted ablation of prostate cancer cells. *cancer research Journal*, 67:6368–2375, 2007.

[12] Richard M. Epand and Hans J. Vogel. Diversity of antimicrobial peptides and their mechanisms of action. *Biochimica et Biophysica Acta*, 1462:11–28, 1999.

[13] Guangshun Wang. NMR studies of a model antimicrobial peptide in the micelles of SDS, dodecylphosphocholine, or dioctanoylphosphatidylglycerol. *The Open Magnetic Resonance Journal*, 1:9–15, 2008.

[14] Guangshun Wang. Structural biology of antimicrobial peptides by NMR spectroscopy. *Current Organic Chemistry*, 10:569–581, 1999.

[15] Tracy L. Whitehead, Lucretia M. Jones, and Rickey P. Hicks. Effects of the incorporation of CHAPS into sds micelles on neuropeptidemicelle binding: Separation of the role of electrostatic interactions from hydrophobic interactions. *Biopolymers*, 58:593–605, 2001.

[16] Laszlo Orfi, Mengfen Lin, and Cynthia K. Larive. Measurement of sds micelle-peptide association using ^{1}H NMR chemical shift analysis and pulsed-field gradient nmr spectroscopy. *Journal of Analytical Chemistry*, 70:1339–1345, 1998.

[17] Brandon A. Begotka, Jennifer L. Hunsader, Chinelo Oparaeche, Jonathan K. Vincent, and Kevin F. Morris. A pulsed field gradient NMR diffusion investigation of enkephalin peptide-sodium dodecyl sulfate micelle association. *Magnetic Resonance in Chemistry*, 44:586–593, 2006.

[18] Kimberly R. Deaton, Elizabeth A. Feyen, Hassan J. Nkulabi, and Kevin F. Morris. Pulsed-field gradient NMR study of sodium dodecyl sulfate micellepeptide association. *Magnetic Resonance in Chemistry*, 39:276–282, 2001.

[19] Tracy L. Whitehead, Lucretia M. Jones, and Rickey P. Hicks. PFG-NMR investigations of the binding of cationic neuropeptides to anionic and zwitterionic micelles. *Journal of Biomolecular Structure and Dynamics*, 21:567–576, 2004.

[20] Xinfeng Gao and Tuck C. Wong. Studies of the binding and structure of adrenocorticotropin peptides in membrane mimics by NMR spectroscopy and pulsed-field gradient diffusion. *Biophysical Journal*, 75:1871–1888, 1998.

[21] Garry W. Buchko, Annett Rozek, David W. Hoyt, Robert J. Cushley, and Michael A. Kennedy. The use of sodium dodecyl sulfate to model the apolipoprotein environment. evidence for peptideSDS complexes using pulsed-field-gradient NMR spectroscopy. *Biochimica et Biophysica Acta*, 1392:101–108, 1998.

[22] William S. Price, Fumihiko Tsuchiya, and Yoji Arata. Lysozyme aggregation and solution properties studied using PGSE NMR diffusion measurements. *Journal of the American Chemical Society*, 121:11503–11512, 1999.

[23] August Andersson, Jonas Almqvist, Franz Hagn, and Lena Maler. Diffusion and dynamics of penetratin in different membrane mimicking media. *Biochimica et Biophysica Acta*, 61:18–25, 2004.

[24] Wei-Jyun Chien, Shu-Fang Cheng, and Ding-Kwo Chang. Determination of the binding constant of a protein kinase C substrate, NG((28-43)), to sodium dodecyl sulfate via the diffusion coefficient measured by pulsed field gradient nuclear magnetic resonance. *Analytical Biochemistry*, 264:211–215, 1998.

[25] Christoph Gobl, Martin Dulle, Walter Hohlweg, Jorg Grossauer, S. Fabio Falsone, Otto Glatter, and Klaus Zangger. Influence of phosphocholine alkyl chain length on peptide micelle interactions and micellar size and shape. *The Journal of Physical Chemistry B*, 114:4717–4724, 2010.

[26] Gang Zheng, Allan M. Torres, Marina Ali, Nicholas Manolios, and William S. Price. NMR study of the structure and self-association of core peptide in aqueous solution and DPC micelles. *Biopolymers*, 96:177–180, 2011.

[27] Giorgio Cerichelli and Giovanna Mancini. NMR techniques applied to micellar systems. *Current Opinion in Colloid & Interface Science*, (6):641–648, 1997.

[28] Chiradip Chatterjee, Barun Majumder, and Chaitali Mukhopadhyay. Pulsed-field gradient and saturation transfer difference NMR study of enkephalins in the ganglioside GM1 micelle. *The Journal of Physical Chemistry B*, 108:7430–7436, 2004.

[29] Raymond T. Syvitski, Ian Burton, Neil R. Mattatall, Susan E. Douglas, and David L. Jakeman. Structural characterization of the antimicrobial peptide pleurocidin from winter flounder. *The Journal of Biochemistry*, 44:7282–7293, 2005.

[30] Deborah A. Kallick, Michael R. Tessmer, Charles R. Watts, and Ching-Yuan Li. The use of dodecylphosphocholine micelles in solution NMR. *Journal of Magnetic Resonance Series B*, 109:60–65, 1995.

[31] Jorge M. O. Fernandes, Jareeporn Ruangsri, and Viswanath Kiron. Atlantic cod piscidin and its diversification through positive selection. *Public Library of Science*, 5:1–7, 2010.

[32] Mitchell J. Brownea, Charles Y. Fenga, Valerie Booth, and Matthew L. Rise. Characterization and expression studies of gaduscidin-1 and gaduscidin-2; paralogous antimicrobial peptide-like transcripts from atlantic cod (gadus morhua). *Developmental & Comparative Immunology*, 35:399–408, 2011.

[33] Suliman Barhoum and Anand Yethiraj. An NMR study of macromolecular aggregation in a model polymer-surfactant solution. *The Journal of Chemical Physics*, 132:19, 2010.

[34] Muzaddid Sarker, Jarratt Rose, Mark McDonald, Michael R. Morrow, and Valerie Booth. Modifications to surfactant protein B structure and lipid interactions under respiratory distress conditions: Consequences of tryptophan oxidation. *The Journal of Biochemistry*, 50:25–36, 2011.

[35] William S. Price. Pulsed-field gradient nuclear magnetic resonance as a tool for studying translational diffusion: Part I. basic theory. *Concepts in Magnetic Resonance*, 9:299–336, 1997.

[36] H.Z. Yuan, L. Luo, L. Zhang, S. Zhao, S.Z. Mao, J.Y. Yu, L.F. Shen, and Y.R. Du. Aggregation of sodium dodecyl sulfate in poly(ethylene glycol) aqueous solution studied by ^{1}H NMR spectroscopy. *Colloid and Polymer Science*, 280:479–484, 2002.

[37] Hans Evertsson, Stefan Nilsson, Christopher J. Welch, and Lars-Olof Sundelof. Molecular dynamics in dilute aqueous solutions of ethyl(hydroxyethyl)cellulose and sodium dodecyl sulfate as investigated by proton NMR relaxation. *Langmuir*, 14:6403–6408, 1998.

[38] Jing Zhao and B. M. Fung. NMR study of the transformation of sodium dodecyl sulfate micelles. *Langmuir*, 9:1228–1231, 1993.

[39] Oller Soderman and Peter Stilbs. NMR studies of complex surfactant systems. *Progress in Nuclear Magnetic Resonance Spectroscopy*, 26:445–482, 1994.

[40] Richard. A. L. Jones. *Soft Condensed Matter*. Oxford University Press Inc, New York, 1st edition, 2002.

[41] Erik Pettersson, Daniel Topgaard, Peter Stilbs, and Olle Soderman. Surfactant/nonionic polymer interaction. A NMR diffusometry and NMR electrophoretic investigation. *Langmuir*, 20:1138–1143, 2004.

[42] Krishnan Chari, John Kowalczyk, and Jyotsana Lal. Conformation of poly(ethylene oxide) in polymer-surfactant aggregates. *The Journal of Physical Chemistry B*, 108:2857–2861, 2004.

[43] Paola Roscigno, Fioretta Asaro, Giorgio Pellizer, Ornella Ortona, and Luigi Paduano. Complex formation between poly(vinylpyrrolidone) and sodium decyl sulfate studied through NMR. *Journal of the American Chemical Society*, 19:9639–9644, 2003.

Chapter 8

Conclusions

Multi-component solutions consisting of polymer, surfactants, micelles, proteins, and other macro-molecules are common to many biological systems, as well as cosmetic, pharmaceutical and technological applications. In addition, the biological cell represents a vivid example of a system that includes different kinds of macromolecules at high concentrations (i.e. 400 g/l). Such a high concentration makes the intracellular medium a crowded environment that affects the characteristics of the macromolecules, such as the structure and dynamics. In our research study, we are trying to experimentally simulate the multi-component crowded environment in the living cell. We have investigated four systems which have significant relevance to modern day biology and medicine: a polymer-surfactant solution, a wormlike micellar system, a protein solution, and a protein-micelle system.

PFG-NMR is a powerful technique that can be used to study the dynamics of different molecular components simultaneously and to study the molecular diffusion in restricted geometries. This might provide structural information about the restricted geometries. However, PFG-NMR, in my view, is underutilized technique in the field of soft matter and biophysics. My doctoral studies represent a systematic attempt to utilize PFG-NMR in order to extract different physical parameters for molecular complexes such as the hydrodynamic radius/radius of gyration of spherical charged

or non-spherical uncharged complexes. As an example, this sheds more light on the binding characteristic of an antimicrobial peptide Gad2 on a membrane mimic environment. Coupled with other techniques, such as deuterium NMR, NMR relaxometry, and rheometry, we utilized PFG-NMR to construct a picture of the microscopic structure of a wormlike micellar system as a system composed of restricted geometries.

8.1 Polymer-Surfactant Aggregates

The dynamics of macromolecules in an anionic surfactant- nonionic polymer system (SDS-PEO system) (chapter 4) has been investigated using nuclear magnetic resonance (NMR). We were able to identify accurately and quantitatively the critical aggregation concentration (CAC) (figure 4.8) and the onset of the crowding respectively.

We measured the self-diffusion of SDS, PEO, and DOH molecules simultaneously over the entire range of SDS concentration in both SDS/D_2O (figure 4.4a) and PEO (0.5% w/v)/SDS/D_2O (figure 4.5a) systems. Using the self-diffusion profile of the SDS molecules for SDS/D_2O system, we were able to extract the critical micellar concentration (CMC) (figure 4.4a).

In our self-diffusion analysis, we assume that the observed self-diffusion coefficient of SDS molecule is a weighted-average of SDS in free and SDS-PEO aggregate (i.e. two-species model). Based on this assumption, we calculated the concentration of SDS molecules in the monomeric state (figure 4.8). We find that the two-species model is definitely valid below 64 mM, and definitely not valid above 145 mM. One can thus say that the onset of crowding occurs somewhere in this concentration range. For $C^{SDS} > 145$ mM the concentration of free SDS molecules C_{f2} based on the two-species model exhibits a sharp increase above CMC that is clearly not physical (figure 4.8). This is consistent with both relaxometry (figure 4.6) that shows crossover between two different regimes at $C^{SDS} = 60$ mM and DOH self-diffusion measurements (figure 4.10) that exhibits a noticeable decrease above ≈ 100 mM. This indicates an increase of the fraction of DOH

203

molecules associated with the charged surfactant. Therefore, a three-species model is defined in the SDS concentration regime $C^{SDS} > 145$ mM which considers the saturation of polymer molecules with surfactant and the formation onset of SDS micelles in the solution. It implicitly signals the onset of crowding in the solution. Based on this model, we were able to calculate the concentration of SDS molecules in the micellar state as well as the concentration of SDS molecules in the monomeric and SDS-PEO aggregate states over the entire range of SDS concentration (figure 4.9a).

8.2 Wormlike Micellar Aggregates

The second system that was studied is a mixed-surfactant wormlike micellar system composed of anionic surfactant SDS and zwitterionic surfactant TDPS in brine solution at surfactant concentration ratio $R = $ [SDS] /[TDPS] $= 0.45$ (chapter 5) that shows deviation from Maxwellian behavior. Using relaxometry (figure 5.1), we identified the TDPS overlap concentration $C^\star$ that shows a crossover from dilute to semidilute regime.

Deuterium NMR spectra (figure 5.2a) shows that the wormlike micellar system is composed of domains with different orientational orders, where there is a slow molecular exchange between different domains. This is consistent with the anisotropic self-diffusion measurements (figure 5.3a) that indicate an isotropic orientation of the micelles.

Moreover, both the time-dependent self-diffusion measurements (figure 5.3a) and the linearity of the mean-square displacement with non-zero offset (figure 5.4a) indicate that the observed-self diffusion is a combination of two dynamical modes: surfactant diffusion in a micelle and micellar self-diffusion. Therefore, by applying the simple model of restricted diffusion within one dimensional boundaries (equation 5.5), we were able to extract the average end-to-end distance of the micellar chain (figure 5.4c). From the mean square displacement versus diffusion time graph (figure 5.4a) we calculated the micellar self-diffusion $((D_m)_x,(D_m)_y,(D_m)_z)$ over the entire

of TDPS concentration in the semidilute regime (figure 5.4b). We found that self-diffusion of the micelles in the semidilute regime is consistent with the self-avoiding walk model, while rheometry (figure 5.5a and figure 5.5b) shows consistency with the random-walk model. This semi-dilute wormlike micellar system behaves like a dilute polymer system when probed on (relatively) short length scales by NMR, but like a concentrated polymer system when probed on long length scales by rheology.

8.3   Protein Clusters in Equilibrium

The third system that was studied is the lysoyme protein system. Diffusometry and relaxometry have been carried out on a system of concentrated lysozyme solutions (chapter 6). We found that the observed self-diffusion coefficient of the lysozyme shows an increase with the diffusion time (figure 6.4a) and that we are already accessing the long time self-diffusion limit (figure 6.2b) even at $\Delta = 50$ ms. This indicates that these concentrated lysozyme solutions include lysozyme in both monomeric and aggregate form, with the lysozyme self-diffusion coefficient being a relaxation-weighted average of the monomer and the aggregate diffusion coefficients (equation 6.4). The time scale is not in the fast exchange limit for the relaxation measurements but nevertheless is fast enough that we get a monoexponential attenuation for diffusion. The average size of a lysozyme cluster was estimated to be nine times the monomer size. Also, we calculated the fraction of lysozyme in monomeric and aggregate states over the entire range of the lysozyme concentration (figure 6.5a). The fraction of lysozyme in both states levels off above lysozyme concentration $C = 100$ mg/ml (at T=298 K) with 20 – 25% fraction of lysozyme in the aggregate state. Our results thus provided unambiguous support for the existence of a phase of equilibrium protein clusters.

8.4   Peptide-Surfactant Aggregates

The dynamics of macromolecules in peptide-anionic surfactant systems was explored using nuclear magnetic resonance (NMR). This study mainly includes three different systems: a system composed of a 19-residue antimicrobial peptide (Gad2) and anionic surfactant (sodium dodecyl sulfate) SDS, a system composed of dipeptides (Ala-Gly and Tyr-Leu) and anionic surfactant (SDS), and a system consisting only of anionic surfactant (SDS) in an aqueous solution.

A comparison of diffusometry results of SDS solutions with and without sodium oxalate buffer (figure 7.4) suggests that the micellar size in the buffered system is smaller than the micellar size in the unbuffered system. Based on NMR diffusometry measurements, we identify the SDS concentration (C^{SDS} = 60 mM) beyond which the crowding effect (figure 7.4a) plays a crucial role in the dynamics of macromolecular aggregates. This provides confirmation of the existence of collective micellar effects at these concentrations, implying that measurements designed to extract true hydrodynamic radii should be carried out well below this concentration. Using NMR relaxometry (figure 7.3) we identify the SDS concentration at which the peptide-SDS and micellar aggregates start forming in a solution.

Next, we extract the true hydrodynamic radius (figure 7.6a) of the Gad2-SDS aggregate over the entire range of SDS concentration where crowding effects are not significantly important. Using NMR diffusometry, we extract the fraction of free dipeptides (figure 7.8c and figure 7.9c) over the entire range of SDS concentration. The functional behavior of the free fraction for smaller dipeptides shows more concentration dependence for the more hydrophobic dipeptide (Tyr-Leu) which has more affinity to form peptide-SDS aggregates.

We find, in summary, that simple models for analyzing diffusion coefficients in peptide-surfactant systems work best at relatively low surfactant concentrations, and for hydrophobic peptides that are much larger than the surfactant, and less well for peptides whose size is comparable to the surfactant.